



January 2015

Simulations Of Convectively-Induced Turbulence Based On Radar-Based Climatology Of Tropical Storm Types

Katelyn Barber

Follow this and additional works at: <https://commons.und.edu/theses>

Recommended Citation

Barber, Katelyn, "Simulations Of Convectively-Induced Turbulence Based On Radar-Based Climatology Of Tropical Storm Types" (2015). *Theses and Dissertations*. 1739.
<https://commons.und.edu/theses/1739>

This Thesis is brought to you for free and open access by the Theses, Dissertations, and Senior Projects at UND Scholarly Commons. It has been accepted for inclusion in Theses and Dissertations by an authorized administrator of UND Scholarly Commons. For more information, please contact zeinebyousif@library.und.edu.

SIMULATIONS OF CONVECTIVELY-INDUCED TURBULENCE
BASED ON RADAR-BASED CLIMATOLOGY OF TROPICAL
STORM TYPES

by

Katelyn A. Barber

Bachelor of Science, State University of New York at Oswego, 2013

A Thesis

Submitted to the Graduate Faculty

of the

University of North Dakota

in partial fulfillment of the requirements

for the degree of

Master of Science

Grand Forks, North Dakota

August

2015

This thesis, submitted by Katelyn A. Barber in partial fulfillment of the requirements for the Degree of Master of Science from the University of North Dakota, has been read by the Faculty Advisory Committee under whom the work has been done and is hereby approved.



Dr. Gretchen Mullendore



Prof. Michael Poellot



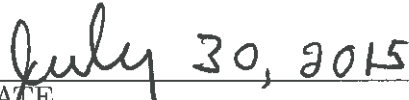
Dr. Mark Askelson

This thesis is being submitted by the appointed advisory committee as having met all of the requirements of the School of Graduate Studies at the University of North Dakota and is hereby approved.



Wayne Swisher

Dean of the School of Graduate Studies



DATE

PERMISSION

Title	Simulations of Convectively-Induced Turbulence based on Radar-Based Climatology of Tropical Storm Types
Department	Atmospheric Sciences
Degree	Master of Science

In presenting this thesis in partial fulfillment of the requirements for a graduate degree from the University of North Dakota, I agree that the library of this University shall make it freely available for inspection. I further agree that permission for extensive copying for scholarly purposes may be granted by the professor who supervised my thesis work or, in her absence, by the Chairperson of the department or the dean of the School of Graduate Studies. It is understood that any copying or publication or other use of this thesis or part thereof for financial gain shall not be allowed without my written permission. It is also understood that due recognition shall be given to me and to the University of North Dakota in any scholarly use which may be made of any material in my thesis.

Katelyn A. Barber
July 30, 2015

TABLE OF CONTENTS

LIST OF FIGURES	vi
LIST OF TABLES	xii
ACKNOWLEDGMENTS	xv
ABSTRACT	xvi
 CHAPTER	
1 INTRODUCTION	1
2 BACKGROUND	3
2.1 Comparison of Known Midlatitude and Maritime Tropical Convection Properties	3
2.1.1 Midlatitude Isolated Shallow Convection	3
2.1.2 Midlatitude Isolated Deep Convection	5
2.1.3 Midlatitude Mesoscale Convective Systems	6
2.1.4 Tropical Isolated Shallow Convection	7
2.1.5 Tropical Isolated Deep Convection	8
2.1.6 Tropical Mesoscale Convective Systems	11
2.1.7 Tropical Cyclones	13
2.2 Comparison of Known Hazards Associated with Midlatitude and Maritime Tropical Convection	15
2.2.1 Lightning	15
2.2.2 Hail	20
2.2.3 Turbulence	22
2.3 Convection and Aviation	29
2.4 WRF Simulations of Tropical Convection and Turbulence .	35
2.4.1 Convection	35
2.4.2 Turbulence	37
3 DATA AND METHODOLOGY	40
3.1 Data	40

3.2	Identification of Objects Using Method for Object-Based Diagnostic Evaluation	48
3.3	Storm Type Classification	51
3.4	Model Configuration and Setup	55
3.5	Model Sensitivity Analysis	57
3.5.1	Simulation 1	58
3.5.2	Simulation 2	61
3.5.3	Simulation 3	62
3.5.4	Simulations 4 and 5	63
3.6	Turbulence Calculation	65
4	RESULTS AND DISCUSSION: WESTERN TROPICAL PACIFIC OBSERVED STORM CLIMATOLOGY	67
4.1	Sensitivity of the Ground-based Radar Storm Climatology Using Three Different Methods	67
4.2	Statistical Comparison of Sensitivity Tests	72
4.3	Ground-based Radar Classification	76
4.4	Satellite-based Radar Classification	81
4.5	Statistical Comparison of Ground-based Radar and Satellite-based Radar Classification	87
4.6	Discussion of Observational Results	94
4.6.1	Seasonal Variability	94
4.6.2	Limitations of the Climatology	99
4.6.3	Influences of Climatology Results on Aviation Operations	102
4.6.4	Storm Type Hazard Risk	103
5	RESULTS AND DISCUSSION: MODEL INVESTIGATION OF CONVECTIVELY-INDUCED TURBULENCE	104
5.1	Case Day Selection	104
5.2	Overview of Observed and Simulated Synoptic and Mesoscale Features	105
5.2.1	5 August 2005	105
5.2.2	6 August 2005	109
5.3	Simulation of Convection and Estimation of Turbulence Results	112
5.4	Discussion	119
6	CONCLUSIONS	128
	REFERENCES	131

LIST OF FIGURES

Figure	Page
1 Simulation of cumulus clouds in Florida (Blyth et al. 2005, Figure 3D). Cloud liquid water content is contoured using 1 g m^{-3} intervals. Arrows represent airflow (m s^{-1}) in the plane of the cross section. The area circled in red indicates the updraft region.	4
2 A schematic of electrical charge distribution inside deep convection (National Severe Storms Laboratory 2015).	18
3 Lightning clusters flash counts detected from an Optical Transient Detector from June-August 1995 (Toracinta and Zipser 2001, Figure 3). Flash counts between 1-3 flashes in the top panel (a) are represented by small dots and small pluses are used to represent flash counts of 4-24 flashes. In the bottom panel (b), medium pluses represent 25-75 flashes and large pluses represent flash counts greater than 75.	19
4 Hailstorm frequency estimated from Advanced Microwave Scanning Radiometer from 2003-2010, a) with a regional scaling of brightness temperature, and b) without a regional scaling of brightness temperature (Cecil and Blankenship 2012, Figure 6).	22
5 Turbulent regions associated with convection indicated by curled lines. Originally presented in USAF Weather for Aircrews Volume 1, 1982. . .	27
6 Annual average rainfall rates derived from TRMM 3B43 over Guam (courtesy of E. Maddox).	41
7 Domain used in the classification study. The white circle represents the area covered by PGUA ground-based radar (230 km radius, $12\text{-}15^\circ\text{N}$, $142\text{-}147^\circ\text{E}$). The red box represents the large domain of the classification study ($6\text{-}21^\circ\text{N}$, $134\text{-}150^\circ\text{E}$).	41

8	Years Level-II and Level-III radar data are available (courtesy of C. Theisen).	43
9	Level-III short range (i.e. 230 km radius) base reflectivity from Guam. Image created using the NOAA Weather and Climate Toolkit.	43
10	Level-III short range (i.e. 230 km radius) echo tops from Guam. Image created using the NOAA Weather and Climate Toolkit.	44
11	TRMM product 2A25 near surface reflectivity swath through the large domain on 5 August 2005.	46
12	TRMM product 2A23 storm top height swath through the large domain on 5 August 2005.	46
13	Example object identifications using the Method for Object-Based Diagnostic Evaluation for 16 August 2005 at 10 UTC and 17 UCT. A and D represent TRMM 2A25 near surface radar reflectivity within the large domain. B and E represent objects identified in the TRMM 2A25 data using MODE. C and F show the numerical value assigned to each object using MODE.	50
14	Location of model domains with horizontal grid spacing. Domain 1 has a horizontal grid spacing of 15 km, domain 2 5 km, and domain 3 1.67 km.	57
15	Simulated 1 km reflectivity on 5 August 2005 at 5:00 UTC for Simulation 1.	60
16	Echo top height calculated using an 18 dBZ threshold for Simulation 1 on 5 August 2005 at 10:00 UTC.	61
17	Echo top height calculated using an 18 dBZ threshold for Simulation 2 on 5 August 2005 at 10:00 UTC.	62
18	Simulated 1 km reflectivity on 5 August 2005 at 5:00 UTC for Simulation 3.	63
19	Echo top height calculated using an 18 dBZ threshold for Simulation 4 on 5 August 2005 at 10:00 UTC.	64
20	An example of a turbulence forecast estimated by the Ellrod Index for the continental United States for flight levels 30,000 ft to 34,000 ft on 24 April, 2015 (Aviation Weather Center)	65

21	Percentage of time convection is present in the small radar domain during 2005 using three methods, a) Method 1, b) Method 2, and c) Method 3, and the percentage of time the area of convection exceeds 12.5% of the small radar domain area using d) Method 1, e) Method 2, and f) Method 3. The percentage of time the area of all types of convection exceeds 60% of the small radar domain g) Method 1, h) Method 2, and i) Method 3. Solid lines represent isolated storms and dashed lines represent MCSs. . .	70
22	Percentage of time a) isolated storms and b) MCSs are present for the three methods. In c), the percentage of time the area of convection exceeds 12.5% of the domain during 2005 is illustrated	73
23	Percentage of time convection is present using ground-based radar within the small radar domain (Method 2) during a) 2005, b) 2010, c) 2011. d-f) Percentage of time the area of convection exceeds 12.5% of the domain area during 2005, 2010, and 2011. g-i) Percentage of time the area of convection (all types of isolated deep and MCSs) and only deep convection exceeds 60% of the small radar domain during 2005, 2010, and 2011. Solid lines represent isolated deep storms and dashed lines represent MCSs.	79
24	Difference of the percentage of time isolated storms are present in the domain from a) 2005-2010, b) 2011-2005, and c) 2011-2010.	80
25	Difference of the percentage of time MCSs are present in the domain from a) 2005-2010, b) 2011-2005, and c) 2011-2010.	81
26	Percentage of time convection is present in the large domain during a) 2005, b) 2010, and c) 2011 using satellite-based radar. Percentage of time the area of convection exceeds 12.5% of the satellite swath area during d) 2005, e) 2010, and f) 2011. Percentage of time the area of deep convection (all types of isolated deep and MCSs) and only deep convection exceeds 60% of the satellite swath area during g) 2005, h) 2010, and i) 2011. Solid lines represent isolated deep storms and dashed lines represent MCSs. . .	84
27	Difference of the percentage of time isolated storms are present in the large domain using satellite-based data. a) 2005-2010, b) 2011-2005, and c) 2011-2010.	86
28	Difference of the percentage of time MCSs are present in the large domain using satellite-based data. a) 2005-2010, b) 2011-2005, and c) 2011-2010.	86

29	Percentage of time a) isolated storms and b) MCSs are present in the small radar domain from the ground-based radar climatology and the large domain from the satellite-based radar climatology. The percentage of time the area of convection exceeds 12.5% of the small radar domain from the ground-based radar climatology and the large domain from the satellite-based radar climatology is represented in c). The percentage of time the area of all types of convective storms and only deep convective storms exceeds more than 60% of the small radar domain from the ground-based radar climatology and the large domain from the satellite-based radar climatology is represented in d).	91
30	a) An example of reflectivity (dBZ) from TRMM 2A25 and PGUA radar on 10 August 2005 at 21 UTC and b) objects identified by the Method for Object-Based Diagnostic Evaluation at 21 UTC on 10 August 2005. . . .	92
31	a-b) Reflectivity determined from TRMM on 10 August at 21 UTC. Objects identified by the Method for Object-Based Diagnostic Evaluation using a convolution radius of c) 8 km and d) 4 km.	93
32	Percentage of time the area of convection covers more than 12.5% of the domain. Solid lines represent the percentage of time calculated from PGUA in the radar domain, and dashed lines represent the percentage of time calculated from TRMM in the large domain.	95
33	Near surface rain categorized by rain type for January, April, July, and October from 1988-2006 in mm day ⁻¹ analyzed from TRMM precipitation radar data (shaded; Aparted from Kodama et al. 2009, Figure 1). The area in the red box represents the large domain.	97
34	Seasonal mean rain frequency in the TRMM precipitation data (shaded; Biasutti et al. 2012, Figure 12). The area in the red box represents the large domain.	98
35	Percentage of echo storm type present in the domain on a) 5 August 2005, and b) 6 August 2005, as determined from the climatology.	105
36	Observed and model simulated soundings at a-b) 00 UTC and c-d) 12 UTC on 5 August 2005.	107
37	a) Mean sea level pressure reanalysis, b) low level convergence, c) upper level divergence, d) deep layer shear at 00 UTC on 5 August 2005.	108

38	Observed and model simulated soundings at a-b) 00 UTC and c-d) 12 UTC on 6 August 2005.	110
39	a) Mean sea level pressure reanalysis, b) low level convergence, c) upper level divergence, d) deep layer shear at 00 UTC on 6 August 2005.	111
40	Echo top height composite of the maximum echo top height from the model simulation using 18 dBZ as a threshold from a) 00-06 UTC, b) 06-12 UTC, c) 12-18 UTC, and d) 18-23 UTC on 5 August 2005. Numbers represent identified convective features.	113
41	Estimated turbulence at a) 10 km, b) 14 km, c) 18 km, and d) 20 km at 06 UTC in 5 August 2005. Light-Moderate turbulence is represented by green, Moderate is represented by yellow, and Moderate-Severe is represented by red. Numbers represent convective features identified in the echo top analysis. Circled regions represent turbulence not associated with convective features.	114
42	The percentage of the domain experiencing turbulence throughout the first 24 hours of the model simulation beginning at 00 UTC on 5 August 2005. Various colors represent the four height levels (10, 14, 18, 20 km), and solid lines represent Light-Moderate turbulence, dashed lines represent Moderate turbulence, and Moderate turbulence is represented by the dashed lines with circular markers.	114
43	As in Fig. 41, except at 12 UTC.	116
44	As in Fig. 41, except at 18 UTC.	117
45	As in Fig. 41, except at 24 UTC.	118
46	As in Fig. 42, except from 00-23 UTC on 6 August 2005.	118
47	Square of Brunt-Väisälä frequency (N^2) and Richardson Number (RI) at a) 06 UTC, b) 12 UTC, and c) 18 UTC on 5 August 2005.	120
48	Comparison of Ellrod Index with varied horizontal resolution, a-b) 1.66 km horizontal grid spacing and c-d) 15 km horizontal grid spacing at 12 UTC 6 August 2005.	123
49	Maximum vertical velocity (m s^{-1}) in the domain during the first 24 hours of the simulation beginning on 5 August 2005.	126

50 Vertical Velocities (m s^{-1}) at 22 UTC on 5 August 2005 at 10, 14, 18, 20 km.126

LIST OF TABLES

Table		Page
1	Summary of field projects in which vertical velocities in deep convection in tropical regions were measured. * represents the average vertical velocity.	10
2	Federal Aviation Administration vertical clearance recommendations prior to 2012.	31
3	Turbulence level descriptions, aircraft vertical acceleration $\sigma_{\Delta n}$ magnitude g (m s^{-2}), and the cube root of eddy dissipation rates $\varepsilon^{1/3}$ ($\text{m}^{2/3} \text{s}^{-1}$) that would induce such responses in B737 and B757 at cruising altitude (Poltovich 2011 Table 1, Aeronautical Information Manual Chapter Chapter 7-1-23, Lane et al. 2012 Table 1, Bowles and Buck 2009).	33
4	A summary of known WRF simulation studies of tropical convection. . .	37
5	Summary of PGUA radar beam (0.5°) average height and width at varying distances from the radar.	44
6	Number of Observations for the small radar and large satellite domain. .	45
7	Summary of data grid spacing.	47
8	Method for Object-Based Diagnostic Evaluation Configuration file. . . .	49
9	Previous studies that used echo top height thresholds for classification purposes.	52
10	Storm height thresholds in km and kft used in this study. TTL represents the tropical tropopause layer.	53

11	A summary of the storm type classification thresholds. ET represents the echo top height of each grid point and TTL represents the tropical tropopause layer. The blue shading represents how each object is classified.	54
12	Model setup.	59
13	p-values calculated from a proportion test with 95% confidence for the percentage of time convective storms are present in the small radar domain using Method 1 and Method 2 during 2005.	74
14	p-values calculated from a proportion test with 95% confidence for the percentage of time the area of convective storms cover more than 12.5% of the small radar domain using Method 1 and Method 2 during 2005.	74
15	p-value calculated from a proportion test with 95% confidence for the percentage of time the area of all types of convective storms and only deep convective storms exceeds more than 60% of the small radar domain using Method 1 and Method 2 during 2005.	74
16	p-values calculated from a proportion test with 95% confidence for the percentage of time convective storms are present within the small radar domain (Method 2) and within 115 km of the radar site (Method 3)	75
17	p-values calculated from a proportion test with 95% confidence for the percentage of time the area of convective storms covers more than 12.5% of the small radar domain Method 2 and the domain area within 115 km of the radar site (Method 3).	75
18	p-value calculated from a proportion test with 95% confidence for the percentage of time the area of all types of convective storms and deep convective storms exceeds more than 60% of the small radar domain using Method 2 and Method 3 during 2005.	75
19	p-values calculated from a proportion test with 95% confidence for the percentage of time convective storms are present in the small radar domain from the ground-based radar climatology and the large domain from the satellite-based radar climatology.	91
20	p-values calculated from a proportion test with 95% confidence for the percentage of time the area of convective storms more than 12.5% of the small radar domain from the ground-based radar climatology and the large domain from the satellite-based radar climatology.	94

21	p-value calculated from a proportion test with 95% confidence for the percentage of time the area of all types of convective storms and only deep convective storms exceeds more than 60% of the small radar domain from the ground-based radar climatology and the large domain from the satellite-based radar climatology.	94
22	Oceanic Niño Index (3 month running mean of SST anomalies for 5 °N-5 °S, 120-170 °W; Climate Prediction Center 2015).	100
23	The number of satellite-based radar swaths per month in the large domain along with the percentage of observations whose areas were greater or less than the ground-based radar area domain (GBR; $1.66 \times 10^2 \text{ km}^2$) during 2005.	102

ACKNOWLEDGMENTS

I would like to extend my sincere gratitude to my advisor, Dr. Gretchen Mullendore for the immeasurable amount of guidance and support throughout my graduate career. Her enthusiasm, motivation, and experience was a true benefit to this research. I would also like to thank my committee members, Prof. Michael Poellot and Dr. Mark Askelson for their feedback, direction, and assistance.

Lastly, I would like to thank my family for all of their encouragement and for always believing in me.

I dedicate this thesis to my amazing sister, Jami. Without you I would have never had the courage to challenge myself and question the world around me. Always remember to dream big!

ABSTRACT

Convective hazards such as lightning, hail, and turbulence are known to be dangerous to aviation. In order to limit aviation accidents associated with convection, the Federal Aviation Administration (FAA) has several avoidance policies in place. Though these policies have been solely based on research performed in the midlatitude, continental United States (U.S.), U.S. aviation operations in the tropics still abide by the FAA avoidance policies. In this study, a limited three year climatology of tropical convection is created using both ground-based and satellite-based radar in the Guam region in order to analyze the frequency of several storm types and to gain a sense of which storm types could most commonly influence aviation. Storm types that are classified are shallow stratiform, isolated, mesoscale convective systems, and tropical cyclones. The results of the climatology indicate that storm type most frequently present near Guam are isolated. In addition, the frequency of storms with higher echo top heights increase during the summer months, suggesting that aviation operations would be most influenced by convection during the summer. The percentage of time that the area coverage of storms exceeds the FAA avoidance policy for thunderstorm coverage also increases during the summer months. Using the Weather Research and Forecast (WRF) model, convection on August 5-6 2005 is simulated to determine the strength and extent of turbulence caused by convectively induced gravity waves. Turbulence is estimated using the Ellrod Index and indicates that Moderate-Severe turbulence is present from 10-20 km, with the greatest concentration of Moderate-Severe turbulence at 14 km throughout the entire simulation period. Further investigation of the Ellrod Index shows a dependency of turbulence

strength and extent on the horizontal model resolution. The results from the model simulations are then compared to the avoidance policies set by the FAA to determine if these policies are representative of tropical convection hazards.

CHAPTER 1

INTRODUCTION

Thunderstorms produce hazardous weather, including lightning, turbulence and hail, which can be very dangerous to aviation. Convectively induced turbulence is an aviation hazard that can cause moderate to severe damage to aircraft and serious injuries to those aboard. According to Golding (2000), turbulence encounters in general cost the commercial aviation industry millions of dollars a year in insurance premiums, workers compensation, injury settlements, and mechanical repairs, indirectly increasing the cost of air travel (Sharman et al. 2006). According to the National Transportation Safety Board (NTSB 2015), two-thirds of turbulence related accidents occur above 30,000 feet (NTSB 2015) when flight attendants and passengers are unbelted. Furthermore, from 1980 through 2008, U.S. commercial airlines reported 234 turbulence accidents that resulted in 298 serious injuries and three fatalities. Though the number of fatalities due to commercial airline turbulence is very low, turbulence encounters account for approximately 65% of all weather related commercial aircraft incidents (Sharman et al. 2006). As U.S. aviation operations continue to increase both nationally and internationally, turbulence encounters and associated costs will also likely increase.

The Federal Aviation Administration (FAA) has strict thunderstorm avoidance policies that are drawn from the conclusions of scientific research and field campaigns conducted solely in the United States (Project Thunderstorm and Oklahoma Study; Byers and Braham 1949 and Burns et al. 1966). Because these are the best data avail-

able, U.S. tropical aviation operations also follow the same FAA convection avoidance policies. However, tropical convective storms have remarkably different characteristics and properties than midlatitude storms. These differences significantly influence the potential hazards associated with various types of convection.

The goal of this study is to examine the potential turbulence hazards associated with different types of tropical convection classified using ground-based and satellite-based radar thresholds near the Guam region. A limited three year climatology was created describing the frequency of storm types. A 48 hour case day period was simulated using WRF to closely examine the degree and extent of convectively induced turbulence. Finally, the results of these simulations are compared to the avoidance policies set by the FAA to determine if those avoidance policies are appropriate for tropical convection.

CHAPTER 2

BACKGROUND

Convection is a process that occurs throughout most regions across the world. However, the properties and hazards associated with convection in various regions differ in many ways. Several observational and modeling studies have been conducted in order to further analyze differences between midlatitude and tropical convection. In this section types and properties of midlatitude and tropical convection, and convective aviation hazards will be discussed.

2.1 Comparison of Known Midlatitude and Maritime Tropical Convection Properties

2.1.1 Midlatitude Isolated Shallow Convection

Midlatitude isolated shallow convection is composed of cumulus clouds that may or may not become cumulonimbus clouds. According to Byers and Braham (1949), only an extremely small number of cumulus clouds continue to grow and attain thunderstorm proportions, due to the negative impacts of dry air entrainment (Wu et al. 2009). Properties of shallow cumulus clouds also vary drastically depending upon the entrainment process (Belair et al. 2005). The dimensions of shallow convective clouds differ between simulation studies and observational case studies. In general it is characterized by a horizontal scale of approximately 2-8 km and vertical scale of approximately 5 km (Blyth et al. 2005, Markowski and Richardson 2010). The lifecycle of shallow cumulus convection first begins above a thermal, having no radar

reflectivity, yet strong vertical development (Byers and Braham 1949, Heus et al. 2009). During the mature stage, the inflow of air from the thermal below the cloud is in balance with the detrainment from the cloud into the environment (Heus et al. 2009). Features of a shallow cumulus cloud during the mature stage as determined from simulations include a strengthening updraft throughout most of the cloud and weaker downdrafts at the cloud edge (Blyth et al. 2005). Maximum vertical velocities within such updrafts occur at higher altitudes later in the mature stage, and were observed to be greater than 15 m s^{-1} on some occasions (Byers and Braham 1949). In model simulations performed by Blyth et al. (2005), updraft velocities were observed to reach 12 m s^{-1} (Fig. 1). Finally, the dissipation phase of shallow convective cumulus cloud takes place when the subcloud thermal has died out and detrainment begins to mix the cloud away into the environment (Heus et al. 2009).

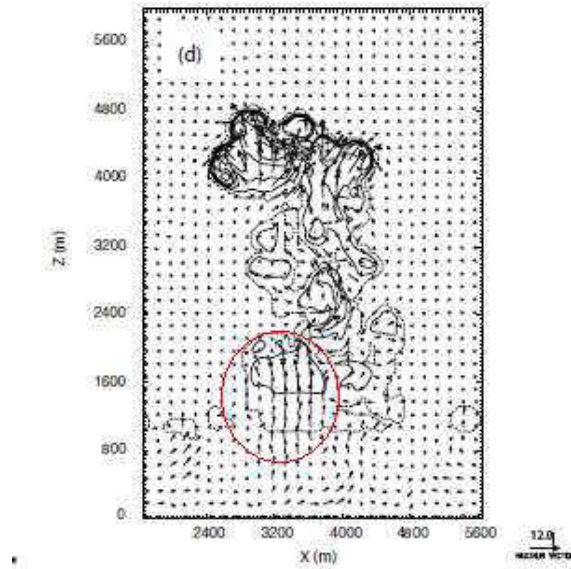


Figure 1: Simulation of cumulus clouds in Florida (Blyth et al. 2005, Figure 3D). Cloud liquid water content is contoured using 1 g m^{-3} intervals. Arrows represent airflow (m s^{-1}) in the plane of the cross section. The area circled in red indicates the updraft region.

2.1.2 Midlatitude Isolated Deep Convection

Midlatitude isolated deep convection is defined herein as cumulonimbus clouds that are often associated with violent phenomena (Ludlam 1976). The lifecycle of an ordinary isolated deep convective cell begins with the towering cumulus stage with a cloud 5-8 km in horizontal extent, cloud tops extending past the freezing level up to 6 km, and a single updraft driven by buoyancy only (Markowski and Richardson 2010). Next, the mature stage features the production of precipitation particles that are large enough to fall through the updraft, which reduces updraft buoyancy through hydrometeor loading. A downdraft is formed as falling hydrometeors cool the air through evaporation, which creates a gust front once it reaches the ground. It is also during this stage that the anvil begins to develop. The convective cloud has grown vertically to approximately 12 km, and extends 8-16 km in the horizontal. The last stage is dissipation, where the downdraft completely takes over the cell. Rain-cooled air spreads away from the updraft, cutting off the potentially buoyant inflow, which substantially weakens the updraft and leaves an orphan anvil composed entirely of ice crystals. The cloud feature in this stage is now 8-11 km in horizontal extent and extends to approximately 11 km in the vertical. The typical lifetime of this type of convection is approximately 30-60 minutes. A subset of isolated deep convection are supercells. Though supercells are the least common storm type worldwide, they are associated with the greatest number of severe weather reports (Markowski and Richardson 2010). Supercells most commonly have a lifetime between 1-4 hours but have been known to last longer than 5 hours. In addition, supercells occur in environments with large vertical wind shear upward throughout a large portion of the troposphere. Furthermore, supercells generally have a horizontal extent greater than 20 km and a vertical extent greater than 15 km. Supercells are characterized by a single updraft and two main downdraft regions, the rear-flank downdraft and the

forward-flank downdraft. The updraft within a supercell can have vertical velocities that exceed 50 m s^{-1} (Bunkers et al. 2006).

2.1.3 Midlatitude Mesoscale Convective Systems

Mesoscale convective systems (MCS) are defined by the National Weather Service as a complex of thunderstorms that becomes organized on a scale larger than the individual thunderstorms and normally persists for several hours or more (NOAA 2014). Houze (2004) describes this type of convection as a cumulonimbus system that produces a continuous precipitation area approximately 100 km or greater in one direction. In warmer midlatitude locations, these systems account for a large fraction of precipitation and contain both convective and stratiform regions with the possibility of developing mesoscale circulations (Houze 2004). Within the convective region, intense vertical cores are present, in contrast to more uniform light precipitation that is present within the stratiform region (Houze 2004).

Several environmental factors that may contribute to the formation of MCSs (Markowski and Richardson 2010). One example is upscale growth, which begins from the outflows of isolated convection that have merged into a large cold pool. This merged cold pool then initiates new convection along the boundary and can lead to severe weather events. Another example is environments with deep-layer wind shear and environmental storm-relative winds at upper levels that are parallel to the boundary. In this scenario, MCS formation occurs in weakly capped environments, immediately after convective initiation, due to strong forcing along an airmass boundary.

2.1.4 Tropical Isolated Shallow Convection

Tropical convection connects radiation, dynamics, and the hydrological cycle in the atmosphere, making it an important component of the climate system (Arakawa 2004). Tropical convective clouds can be divided into three categories: boundary layer, shallow, and deep (Folkins et al. 2008). Shallow convective clouds, more specifically cumulus and cumulus congestus, are the most abundant cloud type below the freezing layer. These clouds account for one-third of convective rainfall in the western Pacific warm pool region (Folkins and Martin 2005, Folkins et al. 2008) and one-fifth of total rainfall over the tropical oceans (Short and Nakamura 2000). Shallow cumulus clouds have a horizontal extent of 1 km and cloud tops are typically between 5 and 7 km, but these clouds can detrain at altitudes as high as 8 km (Khairoutdinov and Randall 2006, Johnson et al. 1999, Folkins and Martin 2005). Observed radar echoes of shallow cumulus clouds from the Global Atmospheric Research Program Atlantic Tropical Atlantic (GATE) project had horizontal areas of $1\text{-}10^2 \text{ km}^2$ (Houze and Cheng 1977) and radar echo tops of precipitating cumulus congestus clouds varied between 4.5 and 9.5 km (Johnson et al. 1999). Observations from the Tropical Ocean Global Atmosphere Coupled Ocean Atmosphere Response Experiment (TOGA COARE) over the western Pacific warm pool region showed that small scale cloud systems almost always formed over the ocean in the afternoon for approximately 1-3 hours when the ocean and atmosphere were the warmest (Chen and Houze 1997). These clouds are an important vertical moisture transport mechanism in the trade wind region (Johnson et al. 1999), providing environment alterations that favor deep convection by increasing the relative humidity in the lower troposphere at a rate of $2 \text{ g kg}^{-1} \text{ day}^{-1}$ (Folkins et al. 2008, Waite and Khouider 2010). However, only 26% of the total cumulus population between 3 and 7 km continue to grow and develop into cumulonimbus clouds (Kumar et al. 2013). Factors such as the existence of low-level

wind shear, humidity of the lower troposphere, low level convergence, and convective available potential energy (CAPE) determine whether or not a shallow cumulus cloud will develop into a cumulonimbus cloud (Folkin et al. 2005).

2.1.5 Tropical Isolated Deep Convection

Deep convective clouds such as those produced by isolated cells and mesoscale convective systems provide the tropics with the majority of its rainfall (Folkins et al. 2008). Over the oceans, heavy rain events contribute to a nighttime maximum in precipitation (Chen and Houze 1997). Deep convective clouds have three main regions: convective core, stratiform, and anvil. The convective core region contains the developing updraft with vertical velocities, near the 0 °C isotherm, between 10-12 m s⁻¹ over tropical land and 4-5 m s⁻¹ over tropical ocean (Wu et al. 2009). Several observational and modeling studies have been conducted in order to more accurately determine vertical velocities in both midlatitude and tropical convection. Field campaigns in which updraft cores in tropical oceanic regions were penetrated with aircraft include KWAJEX, TWP-ICE, GATE, TOGA COARE, and EMEX (Anderson et al. 2005, Wu et al. 2009, Xu and Randall 2001, LeMone and Zipser 1980, Lucas et al. 1994). Table 1 is a summary of relevant findings from several of the field campaigns that took place in the tropics. KWAJEX took place during the summer of 1999, over the Kwajalein Atoll of the Marshall Islands in the Pacific. Updrafts were identified as regions where the vertical velocity was continuously greater than 1 m s⁻¹ for at least 500 m, with an updraft core diameter less than 7 km. Results from KWAJEX showed that no vertical velocity greater than 17 m s⁻¹ were measured during this field campaign (Anderson et al. 2005). TWP-ICE took place in the area around Darwin, Australia and during it various convective regimes were sampled throughout the study period. Model simulations of the collected observations showed that

simulated median updraft velocities were less than 5 m s^{-1} , while the 90th percentile of simulated updraft velocities were greater than 5 m s^{-1} with a maximum updraft velocity between $7\text{-}20 \text{ m s}^{-1}$ above 300 mb (Wu et al. 2009). Moreover, throughout the break period, vertical velocities were between $20\text{-}40 \text{ m s}^{-1}$ for the 90th percentile drafts at 300 mb (Wu et al. 2009). For the GATE campaign in the tropical Atlantic, a six day sampling period contained no updraft core with a one-minute mean vertical velocity greater than 8 m s^{-1} or a maximum one second velocity greater than 15 m s^{-1} (LeMone and Zipser 1980). It was also observed that the 90th percentile of updraft cores in the middle troposphere exceeded 2 km in diameter and had mean vertical velocities greater than 5 m s^{-1} (LeMone and Zipser 1980). Lastly, the mean vertical velocity of updraft cores over the Pacific Ocean during EMEX was 2.2 m s^{-1} and the maximum was 3.2 m s^{-1} (Lucus et al. 1994).

Over the ocean, the stratiform region contains stratiform rain decks that can be heavily precipitating (Futyan and Del Genio 2007). In addition, a greater percentage of stratiform rain fraction is common over the ocean due to greater sustainability and the continual generation and disintegration of convection (Schumacher and Houze 2006). The stratiform cloud deck generally begins at 5 km in the vertical and extends to the tropopause (Houze 1982). Cirrus anvils are produced by the outflow of one or multiple deep convective cells and have large variations in thickness ranging from less than 1 km near anvil edges to several kilometers closer to convective turrets (Ackerman et al. 1988). Detrainmentthe outflow of deep cumulonimbus and stratiform clouds is found between 10 and 17 km (Folkins et al. 2005). Radar echoes from GATE showed that deep convection had horizontal areas between $10^2\text{-}10^5 \text{ km}^2$ (Houze and Cheng 1977); however, the horizontal scale of deep convection is not determined by the depth of convection (Futyan and Del Genio 2007). Studies using Tropical Rainfall Measuring Mission (TRMM) satellite measurements show that nearly half of tropical

Table 1: Summary of field projects in which vertical velocities in deep convection in tropical regions were measured. * represents the average vertical velocity.

Field Campaign	Location	Median Vertical Velocity (m s^{-1})	Height (km)	90 th Percentile Vertical Velocity (m s^{-1})	Height (km)	References
KWAJEX	Marshall Islands	3-5	6-7	< 17	N/A	Anderson et al. 2005
GATE	Tropical Atlantic	$< 8-15$	N/A	$> 5^*$	N/A	LeMone and Zipser 1980
TWP-ICE	Near Darwin, AU	5-10	550-300 mb	5-40	500-300 mb	Wu et al. 2009
EMEX	Pacific Ocean	2.2-3.2*	N/A	N/A	N/A	Lucas et al. 1994

oceanic deep convection has maximum 20 dBZ echo top heights between 6 and 10 km and maximum 30 dBZ echo top heights between 5-7 km (Toracinta et al. 2002).

The diurnal heating of the ocean and atmospheric boundary layer provides for an afternoon initiation of oceanic convection and convective sustainability (Futyan and Del Genio 2007). Full maturity of these storms is reached during the night and early morning. Furthermore, full maturity can be seen by the maximum of cold cloud cover over the ocean before dawn, especially when the intraseasonal oscillation, i.e. a 30-60 day period of fluctuations in rainfall, is convectively active (Chen and Houze 1997).

These convective systems begin with low-level convergence and an updraft, followed by a stratiform region with low-level divergence, and the formation of a downdraft (Hagos et al. 2013). As longer lived systems grow and mature, the boundary layer is filled with air that has lower moist static energy, and a cloud canopy that partially shades the ocean surface from the sun is formed. An environment that is not favorable for widespread convection the following day is created, leading to a bi-diurnal cycle for larger cloud systems over the ocean (Chen and Houze 1997). Thus, the diurnal cycle of deep convection over the ocean is dependent on the size of the cloud system and available midtropospheric moisture before and after initiation (Chen and Houze 1997, Hagos et al. 2013). Studies have also demonstrated that low-level and upper level shear positively increase the longevity of storms over the ocean (Hagos et al. 2013), while the intensity of deep convection is correlated to the cloud top temperature, size, and lifetime (Futyan and Del Genio 2007).

2.1.6 Tropical Mesoscale Convective Systems

Previous studies have shown that tropical cumulonimbus clouds are often organized into mesoscale convective systems (MCS) such as squall lines (Johnson et

al. 1999), the largest of convective storms (Houze 2004), and account for 50-80% of tropical rainfall (Toracinta and Zipser 2001). These precipitating convective clusters occupy approximately 15-20% of the tropics between 5-25 °latitude (Lane et al. 2001) and frequently merge into superclusters or mesoscale convective complexes (Fityan and Del Genio 2007). In fact, the largest MCS systems in the world occur over the Pacific warm pool region (Houze 2004). Tropical MCSs are characterized by a group of deep convective cells connected by extensive stratiform cloud decks in the middle to upper troposphere, and a large cirrus anvil shield formed from the outflow of cumulonimbus cells (Sherwood and Wahrlich 1999). The horizontal dimensions of the convective and stratiform precipitation regions of these MCSs are approximately 30 km and 125 km, respectively, (Houze 2004) and have radar echoes of horizontal area around 10^5 - 10^6 km² (Houze and Cheng 1977). According to Houze (2004), the convective area within superclusters is no greater than ordinary tropical MCSs, but the areal coverage of the stratiform precipitation region is much greater. One important difference between the stratiform region in MCSs over tropical ocean and tropical land is the higher fraction of rainfall produced by deep stratiform ice clouds over the ocean (Houze 2004). Anvil regions generally have bases near 5-6 km and tops between 12-16 km. The anvil structure, depending upon the stage of development, may consist of a midlevel deck with a thinner anvil deck near the tropopause, a single deep deck which has varying ice content with height, or a single elevated deck in the upper troposphere (Ackerman et al. 1988).

According to Sherwood and Wahrlich (1999), the typical life stages of a tropical MCS start with the formation stage, where isolated convective cells begin to arrange in a line or randomly organize. This is followed by the intensification stage is where the isolated cells begin to grow and merge together. During this stage the anvil cirrus shield is formed from the outflow of convective cells and mesoscale drafts. Next,

the mature stage occurs with the formation of large stratiform cloud decks, which precipitate continuously. Updrafts of mature tropical oceanic MCSs are not as strong as those found in tropical continental MCSs due to almost moist adiabatic lapse rates over the ocean, leading to less buoyancy at low levels, and less growth of ice particles by riming (Houze 2004). With weaker updraft strength, fewer graupel particles reach the higher levels of the system, resulting in less radiation being scattered by ice hydrometeors and less lightning production (Houze 2004). If a mesoscale convective vortex (MCV) forms during the mature stage over warm ocean waters, this could be indicative of the beginning stages of a tropical cyclone (Miller and Fritsch 1991). Finally, the dissipation phase marks when active convection weakens and decays, while the stratiform and anvil clouds remain for several hours afterwards before dissipating.

In summary, tropical MCSs and midlatitude MCSs have three significant differences. The first is that the updraft of a midlatitude MCS is stronger due to greater buoyancy at low levels. Secondly, there is less growth of ice particles by riming in tropical MCS convective cores. Lastly, there is less transport of larger ice particles to higher altitudes in tropical MCSs (Houze 2004).

2.1.7 Tropical Cyclones

Tropical cyclones are described by the American Meteorological Society Glossary as any low pressure system having a closed circulation and originating over a tropical ocean (AMS 2014). The diameter of tropical cyclones varies from 100 to greater than 1000 km (AMS 2014). However, according to Molinari et al. (2012) tropical cyclones only have active convection in less than 10% of the total area. According to Houze (2010), there are four stages in the lifecycle of a tropical cyclone. The first stage begins as an MCS with one or more isolated deep vortical hot towers. Vorticity is stretched and advected upward in the low-level environment by conver-

gence in the lower portion of the updraft. In the second stage, hot towers associated with the MCS begin to die off forming a precipitating stratiform cloud, while new towers form. During the third stage, a midlevel MCV is eventually formed by portions of convective cells as the stratiform region gains positive vorticity. In the last stage, new cell development no longer continues; however, the MCV vorticity remains in the stratiform rain region for hours.

Three main cloud features are present within a tropical cyclone: the eyewall, the inner rainband and the outer rainband (Cecil et al. 2002). The eyewall is described as a quasi-circular ring of precipitation that surrounds the circulation center (Cecil et al. 2002). The inner band region extends from the eyewall outward approximately 100 km and is bounded by a no-precipitation slot and an outer rainband (Cecil et al. 2002). In the inner band, stratiform rain is the primary precipitation type with weak convection. Additionally, vertical velocities are weaker than in the eyewall, radar reflectivities decrease more with height above the freezing level than in other regions of the cyclone, and ice scattering signatures detected from satellite are almost completely absent (Cecil et al. 2002). The outer rainband is located 150-200 km away from the center circulation and includes any precipitation associated with the cyclone (Cecil et al. 2002). It is in the outer rainband region that the strongest vertical velocities other than within the eyewall are found due to the presence of more supercooled liquid water (Cecil et al. 2002). In addition, Heymsfield et al. (2010) found that the maximum vertical velocity within tropical cyclone hot towers occurs at 12 km altitude.

In the region of interest for this study, i.e. the northwestern Pacific, the majority of tropical cyclones that develop form along the shear zone between the monsoon westerlies and the trade wind easterlies (Chen and Yen 2006). A 24-year climatology of tropical cyclones in the northwestern Pacific region (Chen and Yen 2006) shows

that weaker cyclones comprise the majority of the cyclone population. Another conclusion drawn from this study is that cyclone lifetimes are related to intensity: 5-9 days for tropical depressions and typhoons, 7-12 days for strong and very strong typhoons, and 9-15 days for catastrophic typhoons. It was also observed that during El-Niño years, tropical cyclones were generally stronger and had longer lifetimes, in contrast to La-Niña years during which most cyclones did not even reach typhoon intensity.

2.2 Comparison of Known Hazards Associated with Midlatitude and Maritime Tropical Convection

2.2.1 Lightning

Lightning associated with midlatitude convection has been studied to correlate trends with severe weather. Schultz et al. (2011) found that the updraft provides an environment that favors mixed-phase microphysical and precipitation processes, charge transfer, separation of charge centers, and large in-cloud electric fields, and is intrinsically related to electric discharges. Lang and Rutledge (2002) describe the lifecycle of lightning with typical convection beginning as intracloud (IC) after the development of the ice phase. Once the main core of the cell begins to descend to lower heights, cloud-to-ground (CG) lightning occurs at a rate of approximately 10 min^{-1} , 90% of which are negatively charged (Lang and Rutledge 2002, Rutledge et al. 1992). In extreme examples, such as supercells, flash rates can exceed 200 min^{-1} (Markowski and Richardson 2010), although rates are more commonly 15-30 min^{-1} for typical severe convection with a majority of IC lightning and less CG.

According to Vonnegut (1994), as a fair weather cumulus cloud grows into a larger convective cloud the intensity of the electric fields increases a thousandfold, and the electric energy within the cloud increases a billionfold. As larger water particles

such as raindrops, graupel, and snow begins to form in the cloud, the electric fields within the cloud increase exponentially. Furthermore, vegetation and other elevated points beneath the convective cloud produce positive point discharge currents. As the electric fields within the cloud continue to increase, a dielectric breakdown occurs and initiates lightning. The primary cause of electrification within the cloud is the charge separation process produced by collisions between large and small ice particles. Of particular concern is that positive cloud to ground lightning can occur more than 100 km away from deep convective cores (Rutledge et al. 1992) in regions such as trailing stratiform regions within MCSs (Rutledge and MacGorman 1988).

Lightning that is produced in the tropics has several physical properties that are similar to lightning produced in midlatitudes; however, the frequency of production varies. According to Christian et al. (2003), 78% of all global lightning occurs between 30 °N and 30 °S. Moreover, systems that produce the most rainfall also produce the most lightning (Toracinta et al. 2002). There is also a significant difference between lightning frequencies over tropical land and tropical ocean. Studies have shown that the likelihood of a precipitating systems having lightning was 40% greater over land than over the ocean (Lal et al. 2014, Toracinta et al. 2002) and that convective cells with vertical velocities characteristic of oceanic storms only rarely develop electric fields strong enough to produce lightning (Zipser 1994). Lightning produced in tropical regions strongly depends on the life stage of convection (Rutledge et al. 1992), has maximum activity after the system has reached maximum size (Futyan and Del Genio 2007), and occurs later in the life cycle of convection over the ocean (Hagos et al. 2013). In addition, Lal et al. (2014) concluded that the optimal level for the electrification of clouds is between 8 and 14 km, and that weak updraft velocities in the mixed phase region limits lightning production. It was also concluded that when

CAPE values are low to moderate ($500\text{-}1000\text{ J kg}^{-1}$), lightning frequency is reduced (Rutledge et al. 1992).

Of the three regions within tropical convection, the stratiform and anvil regions account for 5% of all lightning and only vary 1-2% throughout the year (Peterson and Liu 2011). Stratiform flashes are more common than anvil flashes, especially overnight and into the morning. It was found that the fraction of anvil flashes over land and ocean are similar, in comparison to more stratiform flashes over ocean than land, though the convective core produces more lightning over land. In addition, over land stratiform flashes peak two hours later than anvil flashes. Charge is accumulated in the stratiform region by advection from the convective core and in situ charge generation, because precipitation extends below the freezing layer. Furthermore, lightning in the tropics is characterized by high ratios of IC to CG lightning ratios. This is because of greater vertical development of the upper dipole region (Fig. 2) and larger volumes of cloud above the main negative charge center corresponding to higher tropopause heights, and higher peak currents of return strokes (Rutledge et al. 1992). Another explanation for high IC/CG ratios is that less shear in tropical environments leads to less advection of positive charge away from the negative charge center (Rutledge et al. 1992). IC lightning occurs when the updraft has reached complete maturity, while CG lightning occurs approximately 5-10 minutes later with the development of precipitation-induced downdrafts (Rutledge et al. 1992).

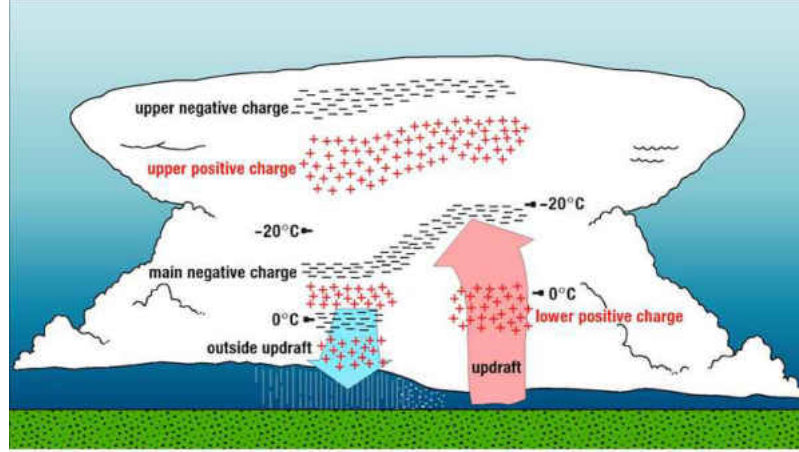


Figure 2: A schematic of electrical charge distribution inside deep convection (National Severe Storms Laboratory 2015).

For tropical MCSs, Toracinta and Zipser (2001) found that there is a noticeable difference between total lightning rates over the ocean and over land as seen in Fig. 3. In particular, for three-month periods, tropical land regions contained 56-66% of the total lightning cluster population while containing 37-41% of the total MCS population. In comparison, tropical ocean regions contain 40-45% of the total MCS population but only contained 15-21% of the total lightning cluster population. Lastly, mixed tropical land and ocean regions contained 19-26% of the total lightning cluster population and 17-22% of the total MCS population (Toracinta and Zipser 2001). Toracinta and Zipser (2001) concluded that this dramatic difference between land and ocean lightning populations is because over the ocean, weak updrafts through the mixed phase region with small ice particles and small amounts of supercooled liquid limits flashes.

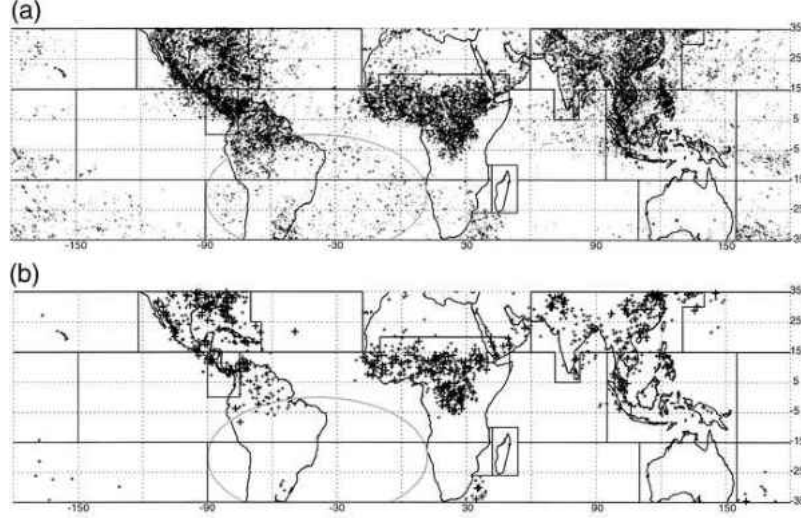


Figure 3: Lightning clusters flash counts detected from an Optical Transient Detector from June-August 1995 (Toracinta and Zipser 2001, Figure 3). Flash counts between 1-3 flashes in the top panel (a) are represented by small dots and small pluses are used to represent flash counts of 4-24 flashes. In the bottom panel (b), medium pluses represent 25-75 flashes and large pluses represent flash counts greater than 75.

Lightning frequency within tropical cyclones depends greatly on intensity, stage, and location. For example, Corbosiero and Molinari (2002) found that there is a correlation between the direction of the 850-200 hPa vertical wind shear in the environment and the azimuthal distribution of lightning. Furthermore, Molinari et al. (2012) found the lightning frequency maximum occurs in the downshear left quadrant (downshear of the environmental vertical wind shear) within 100 km of the cyclone eyewall, while the maximum is in the downshear right quadrant 100-300 km away. If the ambient wind shear exceeds 5 m s^{-1} , the ratio of downshear to upshear flashes is 9:1 (Molinari et al. 2012). The outer rainband region tends to produce more lightning than the eyewall or inner rainband region, producing 2-4 times more lightning than non-hurricane tropical ocean convection (Cecil et al. 2002). Together, lightning in the eyewall and outer rainband region is four times more likely to occur than in the inner rainband and general tropical oceanic convective samples (Cecil et al. 2002).

To summarize, tropical oceanic lightning with the exception of lightning produced by tropical cyclones, is less frequent than tropical lightning over land due to weaker updrafts that limit charge separation, and is thus less of an aviation hazard.

2.2.2 Hail

Hail with a diameter greater than 0.2 inches can only be produced by convective clouds (Changnon 1977) and can cause significant damage to aircraft (Mahinfalah and Skordahl 1998). Severe convective systems such as supercells have been well documented as hail producers (Gallo et al. 2009, Bunkers et al. 2006). According to Markowski and Richardson (2010), the lifecycle of hailstones within deep convective clouds in the midlatitudes begins with the growth of hail stone embryos eventually acquiring enough mass to begin falling, collecting supercooled cloud droplets, and forming graupel particles with diameters of a few millimeters. As the growth of the ice particle continues, the temperature of the hailstone surface may become greater than 0 °C, allowing for supercooled droplets to flow across the hailstone filling in the gaps instead of immediately freezing upon contact. The hailstone will continue to grow through accretion if it is in a region of high supercooled water content, increasing its fall speed.

The microphysics behind hail growth has been investigated thoroughly by numerous researchers. According to Foote (1984), in order for hail to grow by accreting supercooled water, the hailstone must remain in the mixed phase region, either by updraft motions, or transportation from storm circulations. In addition, Heymsfield and Musil (1982) concluded that the production of graupel that serve as hail embryos, from rimming of aggregates of crystals.

Updraft intensity and area can be extremely important for the development of hailstones (Markowski and Richardson 2010, Nelson 1983). The updraft must

be vigorous enough to support a growing hailstone in the mixed phase region and balance the terminal fall speed (Foote 1984). For example, an updraft with a vertical velocity greater than 10.8 m s^{-1} should be strong enough to support and produce a hailstone greater than 0.25 inches in diameter (AMS 2014). Once the updraft intensity has exceeded 20 m s^{-1} , hailstones greater than 0.875 inches in diameter are possible (AMS 2014). The largest hailstones can form if hailstones embryos travel through the center of the updraft at midlevels, high amounts of liquid water are present, and temperatures are approximately in the $-15 \text{ }^{\circ}\text{C}$ to $-20 \text{ }^{\circ}\text{C}$ range (Conway and Zrnich 1993).

Hail in the tropics is very uncommon due to weak vertical velocities at low levels, a lack of midlevel liquid water (Stith et al. 2004), and a large variability of precipitation structure above the freezing level (Petersen and Rutledge 2001). Though the formation of graupel is physically observed in deep tropical oceanic convection (Stith et al. 2004), updraft speeds are not strong enough to support the formation of hailstones. Of the tropical hailstorms that have been observed, most occurred over land and may have been forced by orography (Frisby and Swamson 1967). Cecil and Blankenship (2012) created a climatology of global severe hailstorms using Advanced Microwave Scanning Radiometer for Earth Observing System (AMSR-E) that once again demonstrates a lack of hailstorms over the tropical ocean with a majority in continental locations (Fig. 4). Overall, hail is not of major concern in tropical convection, especially for tropical oceanic convection.

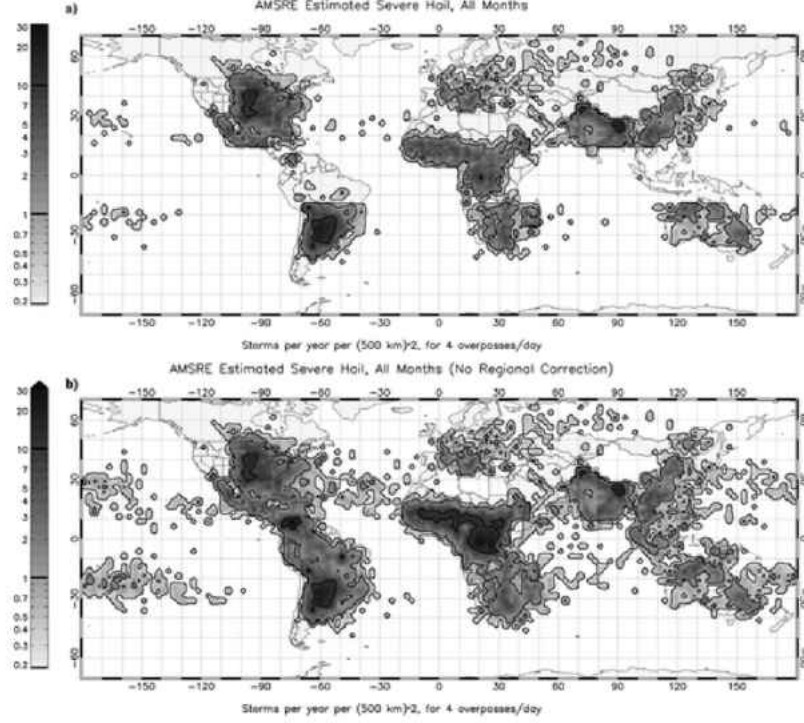


Figure 4: Hailstorm frequency estimated from Advanced Microwave Scanning Radiometer from 2003-2010, a) with a regional scaling of brightness temperature, and b) without a regional scaling of brightness temperature (Cecil and Blankenship 2012, Figure 6).

2.2.3 Turbulence

Turbulence is defined by the American Meteorological Society Glossary as random and continuously changing air motions that are superposed on the mean motion of the air (AMS 2015). In comparison, the Federal Aviation Administration (FAA) simply defines turbulence as the bumpiness in flight that has effects on the aircraft and passengers (FAA 1977). This broad definition includes mechanically induced turbulence, thermally induced turbulence, and the formation and breakdown of gravity waves (Vinnichenko et al. 1980). Thermally induced turbulence and gravity waves will be discussed in further detail in the following sections.

Scorer (1978) found that the process of thermally induced turbulence begins with the formation of dry thermals within the surface boundary layer. These dry thermals can be described as toroidal circulations with a narrow jet-like updraft in the center and gentler sinking towards the sides. As these buoyant features rise and expand, environmental air is entrained. If the thermal is able to pass through the convective condensation level, a cumulus cloud will form. The cumulus cloud is a visual guide to turbulent areas near the edge of the updraft. The continued growth of the cumulus cloud leads to a cumulus congestus and eventually a cumulonimbus if there is a large amount of static instability.

There are several forcing mechanisms that initiate gravity waves within convection (Fovell et al. 1992). The mechanical oscillator effect described by Clark et al. (1986) leads to the formation of gravity waves when updrafts and downdrafts encroach the region where the atmosphere changes from unstable to stable, in turn causing vertical displacements of the isentropes at the base of the stable layer and exciting vertically propagating gravity waves. The wavelength (λ) of vertically oscillating gravity waves can be mathematically expressed using

$$\lambda = \frac{2\pi\bar{u}}{N}, \quad (2.1)$$

where \bar{u} is the mean horizontal wind speed (m s^{-1}), and N is the Brunt-Väisälä frequency (s^{-1}), mathematically represented by

$$N = \left(\frac{g}{\theta} \frac{d\theta}{dz}\right)^{1/2}, \quad (2.2)$$

where g is the acceleration due to gravity (m s^{-2}) and θ is potential temperature (K). Furthermore, Clark et al. (1986) described the second mechanism responsible for gravity wave formation as the obstacle effect or quasi-stationary forcing. In this case,

gravity waves form when a pressure field produced by the upward (and downward) convective region obstructs the environmental horizontal flow.

Another type of wave that can produce turbulence hazardous to aircraft are shearing gravity waves, also referred to as shearing gravity waves (Sekioka 1970 and Pantley 1989). KH waves are generated due to the inconsistencies of temperature and velocity of an interface between two stable layers that becomes displaced vertically. KH waves propagating on a stable interface are known to cause clear air turbulence (CAT) in the upper troposphere and stratosphere (Reiter and Hayman 1962).

The presence of gravity waves does not necessarily indicate a region of turbulence. In order to determine if a region is favorable for the breakdown of gravity waves and therefore the production of turbulence, the gradient Richardson number (Ri ; Reiter and Lester 1968, Pantley 1989)

$$RI = \frac{N^2}{(\frac{\partial V}{\partial z})^2} \quad (2.3)$$

can be calculated. Several past theoretical studies have concluded that a Ri number of 0.25 or less is a good indicator of the breakdown of gravity waves, KH waves, and CAT. From the mathematical formulation of Ri , it is clear to see that the vertical shear of the environment is very important for turbulence production by both KH and gravity waves. The Ri number is known to become very low (<0.25) in regions where deep convection penetrates the tropopause and in convective outflow regions.

The breakdown of gravity waves in the environment is defined by Pantley (1989) as a transition from a coherent wave motion to turbulence. Prior to breakdown, as gravity waves vertically propagate and grow in a non-linear manner, regions of strong overturning of isentropes surfaces are produced (Walterscheid and Schurbert 1990). The overturning of isentropes occurs when the amplitude of the wave grows

large enough where the addition of the wave and the mean field of vertical temperature gradient becomes superadiabatic (Walterscheid and Schurbert 1990). Furthermore, Orlanski and Bryan (1969) found that the overturning of isentropes occurs in regions of upward propagating gravity waves when

$$u' + \bar{u} > c, \quad (2.4)$$

where c is the horizontal phase speed of the wave, u' is the wave horizontal velocity, and \bar{u} is the mean field horizontal velocity. The horizontal phase speed of gravity waves, c_{px} can be represented by

$$c_{px} = \frac{\pm N}{\sqrt{k^2 + m^2}} \quad (2.5)$$

where k and m are the wave number in the x and z direction, respectfully (Lin 2007). This equation demonstrates that as propagating gravity waves enters a more stable region the phase speed of these waves will increase. In summary, the breakdown of convectively-generated gravity waves occurs as a result of steep, large amplitude waves in the potential temperature field (absolutely unstable regions), leading to turbulence production (Walterscheid and Schurbert 1990), as well as encountering a location where $RI < 0.25$ (Reiter and Lester 1968, Pantley 1989), and encountering a critical level where the horizontal velocity of the wave becomes equal to the mean flow velocity (Fritts and Geller 1976).

Convectively induced turbulence (CIT) can be divided into either in-cloud or out-of-cloud based on the location of the turbulence (Lester 1994). Strong vertical variations of velocities within the convective updraft cause in-cloud CIT. These re-

gions are easily avoided by the detection of cloud boundaries both visually and with radar (Kim and Chun 2012).

An in situ measurement used in aviation to determine the intensity of turbulence is the eddy dissipation rate (Emanuel et al. 2013). Eddy dissipation rate (EDR) is a universal measurement of the rate at which energy dissipates in the atmosphere. The value of EDR is in units of turbulent kinetic energy (TKE). According to Emanuel et al. (2013), there are three operational algorithms used to calculate EDR. The first is an indirect method that uses the aircraft accelerometer, while the second uses vertical wind data directly measured from the aircraft, and the third estimates the longitudinal wind from the true airspeed. The following is a simplified example of an algorithm used to calculate EDR in flight using the aircraft accelerometer.

$$\varepsilon^{2/3} = \frac{\sigma_z^2}{I}, \quad (2.6)$$

where σ_z is the variance of the vertical acceleration spectrum, and is the integral of the aircraft response bandpass filtered function H (Cornman et al. 2004). A response bandpass filter is used to remove aircraft maneuver-induced accelerations. Eddy dissipation rates in thunderstorms can also be estimated using ground-based Doppler radar (Meischner et al. 2001), although this method has serious limitations such as poor resolution at large distances (Williams 2004).

Turbulence associated with midlatitude convection occurs in several regions immediately surrounding the storm (Fig. 5), including updrafts, directly above developing updrafts, downdrafts, and mammatus and anvil cloud features (Lane et al. 2012, Lilly 1986, USAF 1982). In addition, severe midlatitude turbulence can be encountered as far as 100 km or more from active convection (Lane et al. 2012).

Developing clouds can generate turbulent motions within themselves and nearby due to moist instabilities within updrafts and mixing (Lane et al. 2003). Out of cloud turbulence may also be generated by the enhancement of background wind shear by penetrating convection, cloud-induced deformation at the cloud boundary, and convectively generated gravity waves that propagate and break above convective systems (Lane et al. 2003). Using a three-dimension model it was found that a turbulent layer 1-2 km in depth is formed above convection in clear air minutes after the updraft penetrates the tropopause (Lane et al. 2003).

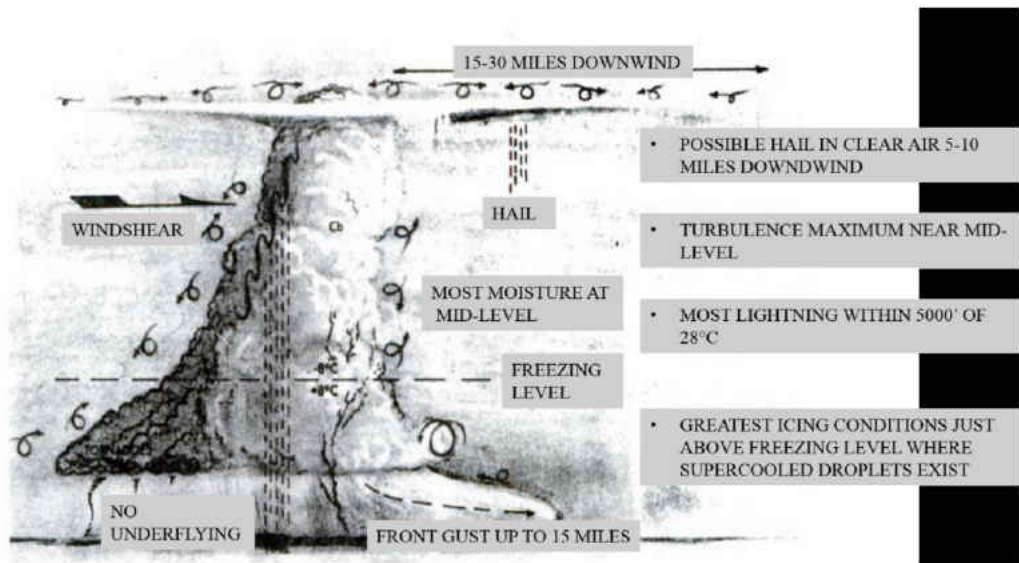


Figure 5: Turbulent regions associated with convection indicated by curled lines. Originally presented in USAF Weather for Aircrews Volume 1, 1982.

During the fall of 2000, the National Aeronautics and Space Administration (NASA) using a Boeing-757 conducted flight experiments in regions that were favorable for convectively induced turbulence to characterize turbulence and its environment, to test hazard detection algorithms for radar, and to test in situ detection (Hamiton and Proctor 2002). Test flights occurred in areas within the flight range of NASA Langley such as Louisiana, Florida, and Texas. This study used root mean square (RMS) of the normal load acceleration, $\sigma_{\Delta n}$, as the measure of in situ turbu-

lence. According to Ahmad and Proctor (2011), the RMS of the normal load acceleration is easy to calculate, airplane centric, quantifies accelerations felt by passengers, and is easily communicated by aircraft operators. Moderate turbulence corresponds to numerical values of $0.1 \text{ g} < \sigma_{\Delta n} \leq 0.2 \text{ g}$ and severe turbulence is numerically represented by $\sigma_{\Delta n} > 0.3 \text{ g}$. During this study significant turbulence was measured within rising cumulus plumes and precipitation shafts. All significant (moderate or severe) turbulence encounters occurred during the periods of along-track shear in the vertical wind. Furthermore, all severe encounters occurred at the interface of the updraft/downdraft couplet located on the downwind side of the convective plume. Finally, test flights showed that large pockets of turbulence can be observed in regions where radar reflectivities are lower than 28 dBZ.

A three year climatology of turbulence in the continental United States created by Wolff and Sharman (2008) indicated that 39% of turbulence encounters occurred above convective clouds, 53% of which were moderate or greater intensity. In addition, 9% of encounters occurred in convective cloud, 80% of which were moderate or greater (Wolff and Sharman 2008). A second climatology created for clear sky turbulence showed that turbulence encounters occurred 44% of the time, 48% of which had moderate or greater intensity (Wolff and Sharman 2008). An important finding from this study was that as cloud height increases to approximately 9-12 km, moderate or greater turbulence intensity encounters increase to 85% of encounters (Wolff and Sharman 2008).

Alexander and Holton (1997) stated that the morphology and generation of convectively induced gravity waves in equatorial regions is still unclear. Even now, almost 20 years later, it is clear that there is still much to learn. Additionally, tropical turbulence observations are very limited and most conclusions have been drawn from model simulations. However, in situ observations of turbulence were obtained in 1953-

1954. 378 cloud penetrations were completed using aircraft in the Caribbean and the most turbulent area was found to increase as the cloud aged and was focused on the downshear side of the cloud (Ackerman 1958).

Lane et al. (2001), using a three-dimensional, nonhydrostatic, and anelastic model developed by Clark (1977), simulated deep convection in the tropics. Lane et al. (2001) concluded that convectively-generated gravity waves develop in both the troposphere and stratosphere when convective updrafts rapidly decelerate. Furthermore, convectively induced gravity waves have the largest amplitude when convection deepens and reaches the upper troposphere. In addition, Lane et al. (2001) and Alexander and Holton (1997) state that tropical squall lines are strong gravity wave radiators. Interestingly, in the study by Lane et al. (2001), the obstacle effect was found not to be the mechanism that generated the gravity waves and, therefore, shear was not important for the generation of gravity waves in simulated tropical convection.

Overshooting cloud tops can also be indicators of possible strong turbulence in both the tropics and midlatitudes. Romps and Kuang (2009) found that clouds in the tropics often overshoot into and beyond the tropopause. Zipser (2003) found that this can only happen if the updraft above 500 mb is reinvigorated by freezing of condensates and air parcels rise along an ice adiabat. However, from a seven year climatology of tropical cloud fraction conducted by Hong et al. (2008), less than 0.6% of tropical clouds over the ocean and less than 0.8% over tropical land have convective overshooting. Lastly, Lane et al. (2012) found that turbulence associated with tropical cyclones is located in the cloud bands that extend outward.

2.3 Convection and Aviation

According to the U.S. Department of Transportation Federal Aviation Administration Advisory Circular from 2013, all thunderstorms have potential conditions

that are hazardous to aviation. These hazards include tornadoes, turbulence, icing, hail, low ceiling and visibility, altimeter effects due to rapid pressure changes, lightning, and engine water ingestion. As the focus of this study is hazards within high-altitude flights above tropical convection and not takeoff or landing procedures, only turbulence discussed further.

Turbulence, in particular, is the number one cause of injuries to flight crew and passengers (Mecikalski et al. 2007). Turbulence is dangerous to aircraft because additional stresses are placed on the aircraft while pilots attempt to hold a constant altitude (DOT-FAA 2013). Kaplan et al. (1999) found that 82% of reported turbulence incidents between 1990 and 1996 occurred near or within convective activity. Pantley (1989) summarized five main types of CIT hazardous to aviation: 1) updrafts and downdrafts within and near deep cumulus convection, 2) rapidly growing thunderstorms, 3) Kelvin-Helmholtz instability induced by outflows near the tropopause, 4) turbulent vortices that are formed due to breaking of convectively initiated waves above and downwind of thunderstorms, and 5) turbulent wakes caused by barrier type effects around and within the lee of thunderstorms.

With so many potential hazards associated with convection, there are several aviation avoidance policies in place to limit the number of convection related accidents (U.S. DOT-FAA 2013). The first is that pilots should avoid any severe thunderstorm (i.e., thunderstorm with an intense radar echo) by at least 20 miles. Next, pilots should circumnavigate an entire area if the respective region has six-tenths thunderstorm coverage. Furthermore, the use of extreme caution when flying near any thunderstorm with echo tops greater than 35,000 feet is advised. Finally, pilots should also avoid flying beneath the anvil region and through thunderstorms even if the path through to the other side is visible. It is important to note that prior to 2013, thunderstorms identified as severe required a vertical clearance of 1,000

ft for every 10 kt wind speed at cloud top (FAA 2012, Table 2). NASA also has a rendition of the thunderstorm avoidance policies for their research Global Hawk (Cecil et al. 2014). The first is that thunderstorms must be laterally avoided by at least 25 nautical miles when flying at or below 50,000 ft. The second is that aircraft must have a 5,000 ft vertical separation between any significant convective cloud top. Furthermore, if any cloud top height is greater than 50,000 ft the aircraft must have a lateral 25 nautical mile clearance. Next, if cloud tops are below 50,000 ft a 10,000 ft vertical separation is necessary from any region reporting lightning. The final two policies are that no flight should be conducted in a region where icing conditions and moderate or severe turbulence is forecasted or reported.

Table 2: Federal Aviation Administration vertical clearance recommendations prior to 2012.

Wind Speed	Vertical Clearance	
kts	km	kft
100	3.05	10
90	2.74	9
80	2.44	8
70	2.13	7
60	1.83	6
50	1.52	5
40	1.22	4
30	0.92	3
20	0.61	2
10	0.31	1

The FAA categorizes turbulence into four verbal descriptors (see Table 3) that are easy to communicate between pilots and traffic control, and corresponds to in-situ numerical eddy dissipation rates ε ($\text{m}^2 \text{s}^{-3}$) and vertical acceleration (m s^{-2}) (Pololovich et al. 2011, Lane et al. 2012, Bowles and Buck 2009, FAA 2015). Light turbulence is described by the FAA as turbulence that momentarily causes slight, erratic changes

in altitude and or pitch, roll, and yaw, and passengers may feel a slight strain against their seat belts. Moderate turbulence is described as being similar to Light turbulence but with a greater intensity. During Moderate turbulence, changes in altitude and attitude occur but the aircraft remains in positive control at all times, and variations in indicated airspeed are experienced. Furthermore, passengers feel a definite strain against their seat belts and walking around the cabin is difficult. Turbulence that causes large, abrupt changes in altitude, attitude (orientation of the aircraft to Earth's horizon), and indicated airspeed is described as Severe. In addition, the aircraft may be temporally out of control. Severe turbulence also causes passengers to be violently forced against their seats. Lastly, Extreme turbulence is described as a situation when the aircraft is violently tossed about, is practically impossible to control, and can suffer structural damage. This magnitude of turbulence is described as truly frightening for those aboard.

Table 3: Turbulence level descriptions, aircraft vertical acceleration $\sigma_{\Delta n}$ magnitude g ($m\ s^{-2}$), and the cube root of eddy dissipation rates $\varepsilon^{1/3}$ ($m^{2/3}\ s^{-1}$) that would induce such responses in B737 and B757 at cruising altitude (Politovich 2011 Table 1, Aeronautical Information Manual Chapter Chapter 7-1-23, Lane et al. 2012 Table 1, Bowles and Buck 2009).

Turbulence	Aircraft Reaction	RMS of Aircraft Vertical Acceleration $\sigma_{\Delta n}$	Aircraft Vertical Acceleration Magnitude (g)	$\varepsilon^{1/3}$
		$m\ s^{-2}$	$m\ s^{-2}$	$m^{2/3}\ s^{-1}$
Light	Turbulence that momentarily causes slight, erratic changes in altitude and/or attitude (pitch, roll, and yaw).	0.1 g	0.2-0.5	0.1-0.3
Moderate	Turbulence that is similar to Light turbulence but of greater intensity. Changes in altitude and/or attitude occur but the aircraft remains in positive control at all times. It usually causes variation in indicated speed.	$0.1\ g < \sigma_{\Delta n} \leq 0.2\ g$	0.5-1.0	0.3-0.5
Severe	Turbulence that causes large, abrupt changes in altitude and/or attitude. It usually causes large variations in indicated airspeed. Aircraft may be momentarily out of control.	$0.3\ g < \sigma_{\Delta n} \leq 0.6\ g$	1.0-2.0	0.5-0.7
Extreme	Turbulence in which the aircraft is violently tossed about and is practically impossible to control. It may cause structural damage.	$0.6 < \sigma_{\Delta n}$	>2.0	>0.7

Several studies of aviation accidents involving thunderstorms and turbulence have been conducted. A case study performed by Fovell et al. (2007) considered convectively-induced clear air turbulence experienced by two commercial 757 flights over Northwest Indiana, on 5 August 2005. According to satellite imagery, both aircraft were at least 20 km away from any large convective cloud and flying at approximately 37 kft and 39 kft when severe turbulence was encountered. Weather Research and Forecasting model (WRF) simulations showed that the forcing mechanism responsible for the turbulence was rapid growth of strong convection along a synoptic-scale cold front. In addition, the convection altered its environment farther than the distance of a detectable anvil, causing a decrease in stability and an increase in shear. This lowered the Richardson number, thereby bringing it closer to the critical value for turbulence generation.

Kim and Chun (2012) thoroughly examined a severe turbulence encounters by a commercial aircraft flying from Jeju, South Korea, to Osaka, Japan on 2 September, 2007 using the Advanced Research WRF (ARW-WRF). The aircraft was flying above an area of above an area of dissipating convection near 33.68 °N, 131.26 °E. Shortly after reaching the cruising altitude of 10.7 km, the aircraft experienced two strong changes in vertical acceleration, corresponding to strong peaks in wind speed and direction. These events are considered to be of extreme and moderate-severe turbulence intensities and caused 6 injuries. The pilots reported that there was no visual warning of deep convection or well defined echoes on the aircraft radar at the time of the turbulence encounters. Kim and Chun (2012) found that three hours prior to the encounter, there was deep convection ahead of a cold front southwest of the encounter location. As the dominant southwest wind advected the convection to the encounter location, the turbulence generated along the convective cloud boundary was also advected, even as the convection began to dissipate. At the same time,

vertically propagating convective gravity waves were breaking as they reached their critical level. WRF simulations showed that out-of-cloud CIT was located 2 km above the dissipating convection. This study illustrated that dissipating convection also has the potential for significant turbulence encounters.

A third example occurred in 1983 on 12 October (Pantley 1989). At 0418 GMT, an American Airlines DC-10 was flying at 11.3 km southwest of Bermuda (27 °N, 68.65 °W) when it experienced a vertical acceleration of $-1.58\ g$ from normal gravity. Pilots reported that the plane was located within the top of a growing cumulonimbus cloud, though onboard radar detected no precipitation. 12 passengers were injured as a result of this encounter. Convective activity along the flight path was visible on satellite imagery and ship reports confirmed cumulonimbus clouds in the area (Pantley 1989). After analysis of meteorological and aircraft records, Pantley (1989) suggested that the aircraft was in a generally stable environment when it flew through a gravity wave approximately 10 km in length and experienced Moderate turbulence in the updraft region. Following this, the aircraft entered the convective cloud, which extended past the flight level and severe turbulence was encountered. As the aircraft exited the cloud, Light turbulence was experienced due to shorter-wavelength-gravity waves. Pantley (1989) also suggests that the aircraft may have passed through a thunderstorm anvil region.

2.4 WRF Simulations of Tropical Convection and Turbulence

2.4.1 Convection

Model simulations of convection in tropical regions are becoming more frequent as the understanding of tropical dynamics improves. Many of these modeling studies involve the simulation of tropical cyclones in the Pacific and Indian oceans

(Pattanayak et al. 2008, Osuri et al. 2010, Raju et al. 2011, and Potty et al. 2012). Though the goal of this study is not to simulate tropical cyclones, it is important to compare the setup of WRF used in other tropical simulation studies to gain a sense of which parameterizations are appropriate for tropical convection simulations (see Table 4). A majority of these studies favored using the Kain-Fritsch cumulus scheme, which is a mass flux parameterization that uses the Lagrangian parcel method to determine if any instability does exist or will exist to promote cloud growth, and what the convective properties of the clouds will be (Kain 2004). Furthermore, the Kain-Fritsch scheme is divided into three parts: the trigger function, the mass flux formulation and the closure function. Results from various tropical cyclone simulation studies have shown that using the Kain-Fritsch scheme produced better cyclone track forecasts (Osuri et al. 2010, and Raju et al. 2011). When Kain-Fritsch is paired with the Yonsei University planetary boundary layer scheme (PBL YSU), WRF accurately simulates the thermodynamical and dynamical properties of a cyclone (Raju et al. 2011).

Table 4: A summary of known WRF simulation studies of tropical convection.



2.4.2 Turbulence

As previously stated, numerous studies have implemented WRF to analyze turbulence. However, a majority of these modeling studies focused on simulating turbulence in midlatitude regions. Nevertheless, it is valuable to be familiar with model configurations for turbulence studies in any region. Kim and Chun (2012) used the ARW-WRF model, version 3.1, with six nested domains to investigate turbulence encountered by a commercial flight near Japan. The horizontal grid spacing of this study's domains were 30, 10, 3.3, 1.1, 0.37, and 0.12 km. The model top was 20 hPa ($z = 27$ km), with 113 vertical sigma levels. The vertical grid spacing used in all domains for this study were as follows: 300 m in the planetary boundary layer, 100 m from 2 km to 13 km in the vertical, and then increasing linearly from 100

m at $z = 13$ km to 500 km at the model top. This study used a sponge layer with Rayleigh damping in all of the domains highest 5 km and five relaxation grid points for the lateral boundaries. Furthermore, two-way nesting was implemented for specific time intervals. Physical parameterizations implemented in this study included the WRF single-moment 6 class (WSM6) microphysics scheme, the Kain-Fritsch convective parameterization, the Mellor–Yamada–Janjić (MYJ) PBL scheme, and the Rapid Radiative Transfer Model radiation model (RRTM) longwave radiation scheme. Some differences were noted between the simulations and observational data included sea level pressure differences in the western section of the 30 km domain and a typhoon of weaker intensity in the simulation than observations, which was most likely due to the absence of the cyclone during model initialization. In addition, simulated soundings had four discrepancies when compared to the observed soundings. First, the dewpoint temperature was not accurately simulated. Secondly, the lifting condensation level (LCL) was lower than the observed LCL, which could be due to the inaccurate moisture profile. Due to the inaccurate moisture profile and lower LCL, CAPE was greater than the observed CAPE. Finally, the simulated wind speed was slower than the observed. Most importantly, Kim and Chun (2012) determined that the simulations of deep convection agreed well with the observed timing, location, and structure of convection. To conclude, Kim and Chun (2012) stated that by changing the PBL scheme to the Yonsei University (YSU) scheme, turbulence near the dissipating convection was more widespread and CAPE values were greater than both the previous simulation and observations, but further sensitivity tests to investigate additional factors were not performed.

Triar and Sharman (2009) investigated how far convectively induced turbulence can propagate from MCSs in the Great Plains using WRF version 2.2. A single-subcontinental domain was used with 600 x 500 horizontal grid points, and a 3 km

grid spacing. The vertical grid in this study had 64 levels and the model top was near 31 km. The vertical spacing was between 60-170 m in the lowest 1 km, approximately 400 m between 1-15 km, and approximately 500-1500 m from 15 km to the model top. The reflection of vertically propagating waves off the rigid upper boundary was lessened by the use of diffusive damping. The Thompson microphysical scheme was implemented in this study. According to Triar and Sharman (2009), the resolution of this study was too coarse to simulate turbulence and the mechanisms of the turbulence production could not be resolved due to limited observations. Nevertheless, they were able to suggest that strong vertical shear in the upper level outflow of an MCS can favor turbulence over a large region far from the source due to Kelvin-Helmholtz instabilities.

Tropical modeling studies of turbulence induced by convection using WRF have mostly been limited to tropical cyclones, strong MCSs, and aviation encounters with turbulence. Large eddy simulations of severe convectively-induced turbulence experienced by commercial flights in tropical regions were conducted by NASA Langley using the Terminal Area Simulation System (Ahmad and Proctor 2011). The Terminal Area Simulation System (TASS) used environmental conditions obtained from WRF to initialize the model. One example TASS-WRF simulation was for 3 August, 2009. On this day, Continental Airlines Flight 128 (Boeing 767) encountered turbulence north of Bavaro, Dominican Republic, while flying at an altitude of 11.0 km over isolated cumulus congestus and cumulonimbus. This simulation had two high resolution nests, with a mesh resolution of 7.38 km in the innermost domain (Ahmad and Proctor 2011). This simulation showed that light to moderate turbulence occurred in the top of the storm even though radar reflectivity values were low, agreeing with a previous study performed by Hamilton and Proctor (2002).

CHAPTER 3

DATA AND METHODOLOGY

3.1 Data

In this study a classification of tropical storm types for 2005, 2010, and 2011 is created using Level-III NEXRAD radar short range data products collected at the Andersen Air Force Base in Guam (PGUA), and NASA Tropical Rainfall Measuring Mission (TRMM) products. The years were chosen by examining the annual average rainfall rate around Guam for a 14 year period using the TRMM satellite product 3B43. 3B43 provides monthly rainfall rate estimates gridded over 0.25° latitude x 0.25° longitude (GES DISC, 2014). This evaluation showed that the annual average precipitation rate between 1998 and 2011 is 0.23 mm hr^{-1} (Fig. 6). The years 2005, 2010, 2011 were selected for further analysis because they represent a year with average rain rate, below average rain rate, and above average rain rate, respectively. The classification of storm types is completed for two domains (Fig. 7). The first domain is a circular area centered around 13.449°N , 144.815°E and represents the area covered by the PGUA radar, hereafter the small radar domain. The radius of the small radar domain is 230 km and has a total area of approximately $1.6 \times 10^5 \text{ km}^2$. Both a ground-based and a satellite-based classifications are performed for this domain. The second larger domain is a rectangular area that covers $6\text{--}21^\circ\text{N}$, $134\text{--}150^\circ\text{E}$, hereafter the large domain. The total area of the large domain is approximately $2.9 \times 10^6 \text{ km}^2$. Only a satellite-based classification is performed for this domain due to a lack of ground-based radar coverage.

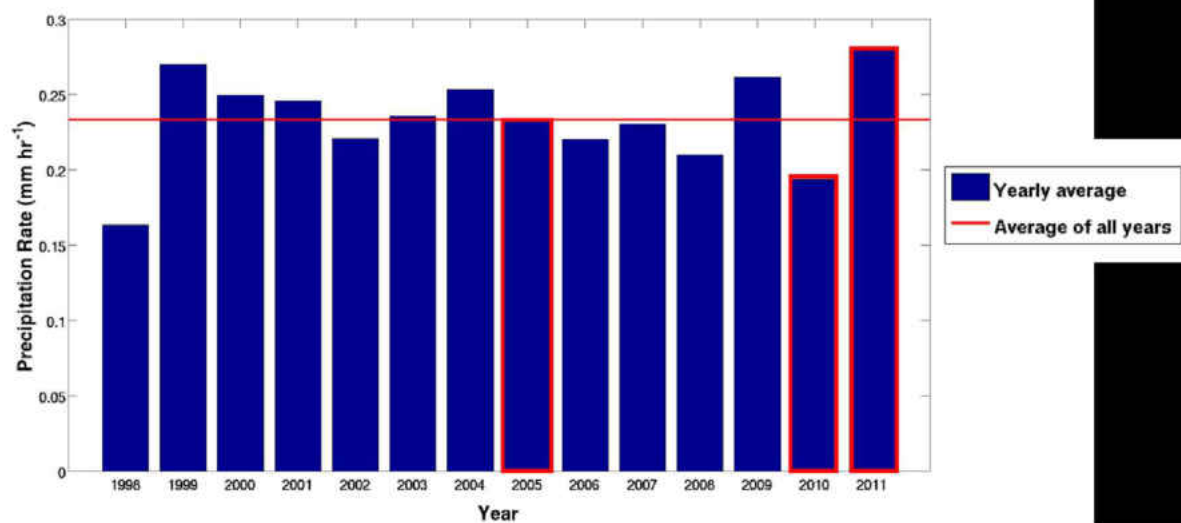


Figure 6: Annual average rainfall rates derived from TRMM 3B43 over Guam (courtesy of E. Maddox).

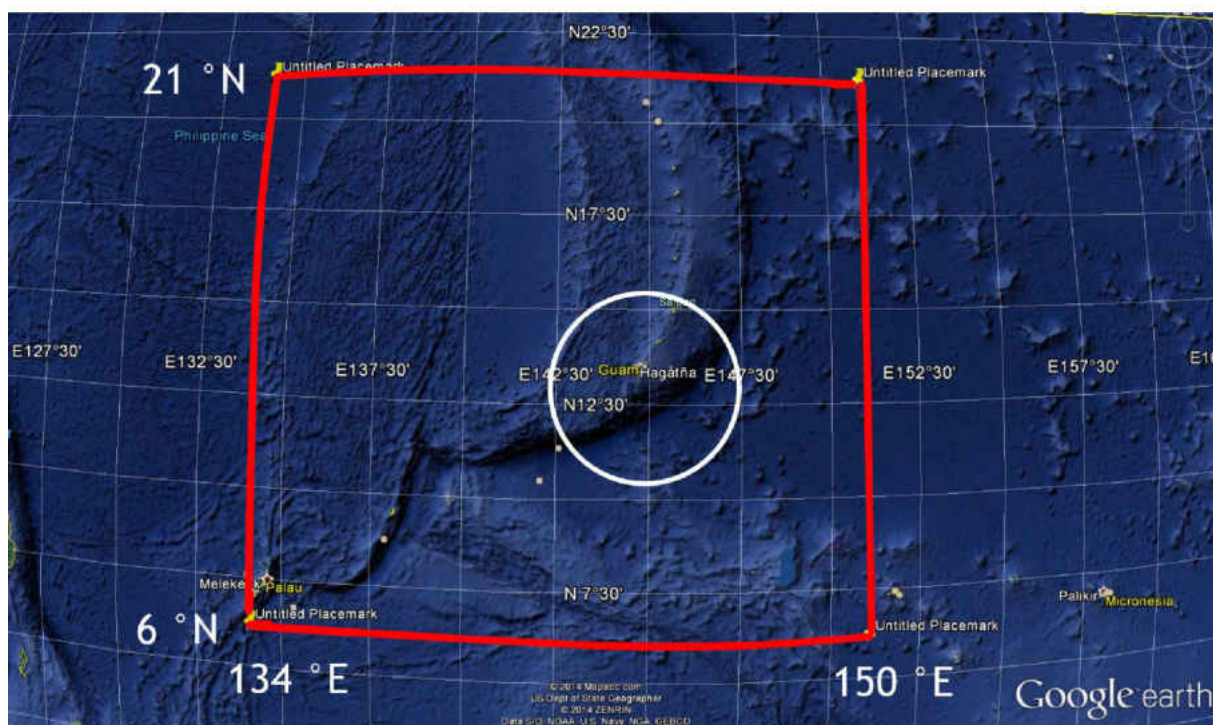


Figure 7: Domain used in the classification study. The white circle represents the area covered by PGUA ground-based radar (230 km radius, 12-15 °N, 142-147 °E). The red box represents the large domain of the classification study (6-21 °N, 134-150 °E).

Level-III radar data are processed analysis products that originated from Level-II radar base reflectivity, mean radial velocity, and spectrum width data (NCDC 2014). Level-III data products are used in this study because Level-II data from the Andersen Air Force Base radar are unavailable for the study years (Fig. 8). The products used in this study are base reflectivity and echo tops. Base reflectivity (N0R) provides reflectivity data with 5 dBZ increments at an elevation scan angle of 0.5° grid spacing of 1.0 km x 1.0 km, and range of approximately 230 km (Hamer 2009). An example of base reflectivity data file is provided in Fig. 9. The average heights of the radar beam at varying distances from the radar site are provided in Table 5. The echo top product (NET) provides the height of storm tops in thousands of feet in 5,000 feet increments, has a grid spacing of 4 km x 4 km, and a range of approximately 230 km (Hamer 2009). An example of an echo top data file is provided in Fig. 10. Each of these products is originally in NIDS (NEXRAD Information Dissemination Service) radial format and needs to be converted to gridded NetCDF (Network Common Data Form). This is accomplished using NOAAs Weather and Climate Toolkit which allows users to specify the export format and grid size. Using this toolkit, both N0R and NET are converted to NetCDF with a horizontal spacing of 1.266 km in 10 minute increments with the intention of capturing the majority of storm lifecycles and slightly decreasing the total number of observations. The number of PGUA radar observations in the small radar domain used in this study from 2005 is 30035, 28611 from 2010, and 30423 from 2011 (Table 6).

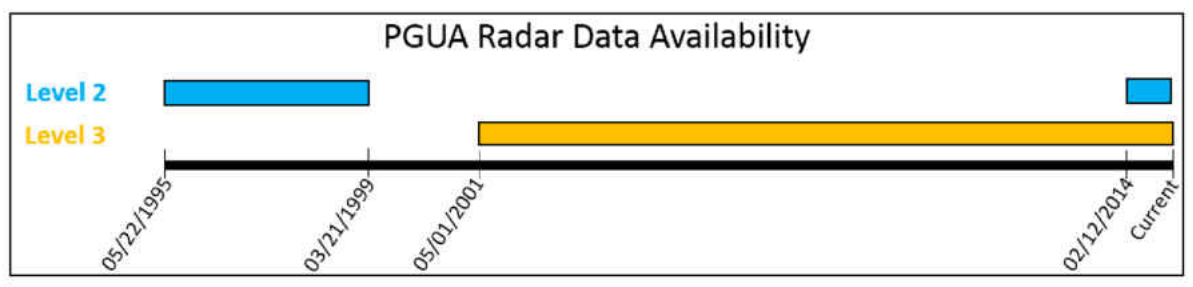


Figure 8: Years Level-II and Level-III radar data are available (courtesy of C. Theisen).

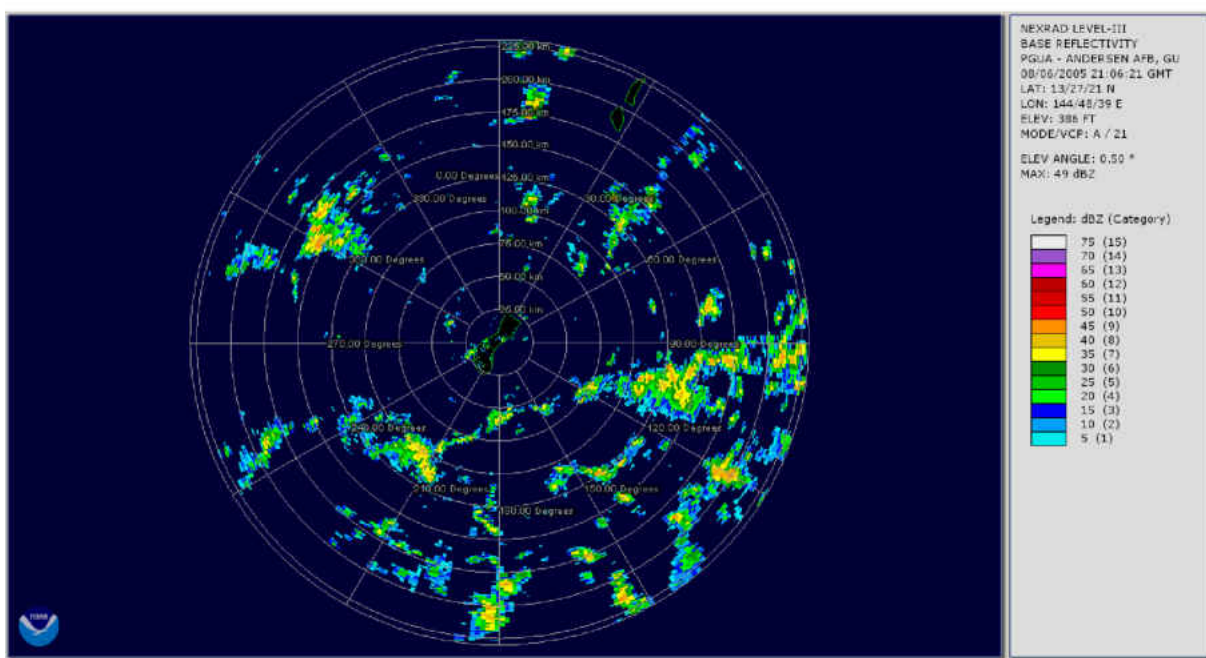


Figure 9: Level-III short range (i.e. 230 km radius) base reflectivity from Guam. Image created using the NOAA Weather and Climate Toolkit.

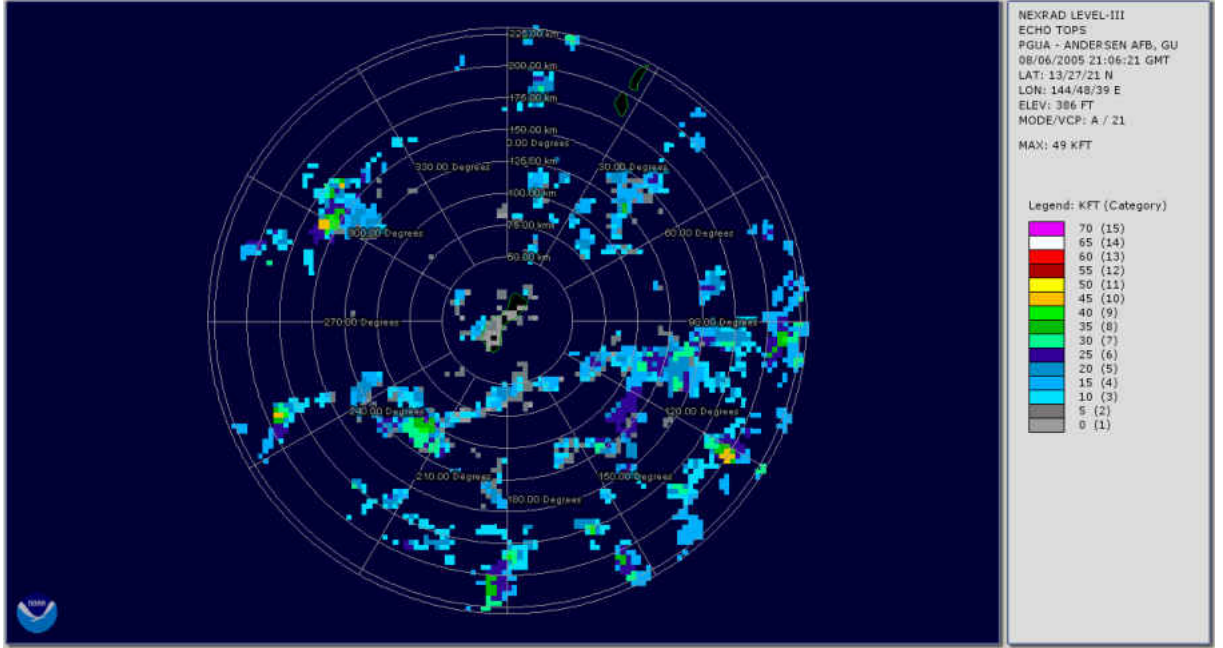


Figure 10: Level-III short range (i.e. 230 km radius) echo tops from Guam. Image created using the NOAA Weather and Climate Toolkit.

Table 5: Summary of PGUA radar beam (0.5°) average height and width at varying distances from the radar.

Distance from Radar (km)	Beam Height (km)	Beam Width (km)
25	0.26	0.41
50	0.59	0.81
75	1.02	1.22
100	1.50	1.6
125	2.17	2.03
150	2.77	2.44
175	3.51	2.84
200	4.31	3.23
225	5.21	3.65

Table 6: Number of Observations for the small radar and large satellite domain.

Product	Domain	2005	2010	2011
PGUA Radar	Small Radar	30035	28611	30423
TRMM Radar	Small Radar	347	349	346
	Large	1268	1289	1300

Storm classifications for the same study years are completed using radar products from TRMM product level 2A precipitation radar rainfall rate and profile (2A25) data and rainfall characteristics (2A23) data for the two domain regions. Product 2A25 provides an estimate of the vertical profile of rainfall rate for each radar beam, while product 2A23 provides a Rain/no-Rain flag, a bright band indicator, storm top heights, and rain type classes. Near surface reflectivity (dBZ) from 2A25 and storm top height in meters from 2A23 are analyzed in this study (Figs. 11 and 12). Both 2A23 and 2A25 have a swath width of 247 km, horizontal spacing of approximately 4.0 km at nadir, and are available in the small radar domain once a day and approximately five times a day in the large domain (TRMM Precipitation Radar Team, 2011). Products 2A25 and 2A23 are originally in HDF-4 (Hierarchical Data Format) format and are converted to NetCDF using NCL (NCAR Command Language). Because TRMM is an equatorial orbiting satellite, an additional step must be taken to identify scans that are present in the radar domain and the large domain. By setting latitude and longitude boundaries representative of the edges of domains, scans that are in these domains are linearly interpolated to a 1.266 km x 1.266 km grid for the small radar domain and a 4 km x 4 km grid for the large domain. In this study, a total of 347 swaths passed through the small radar domain in 2005, 349 swaths in 2010, and 346 swaths in 2011. Furthermore, 1268 swaths passed through the large domain

in 2005, 1269 swaths in 2010, and 1300 swaths in 2011. A summary of observations is provided in Table 6 and data spacing is provided in Table 7.

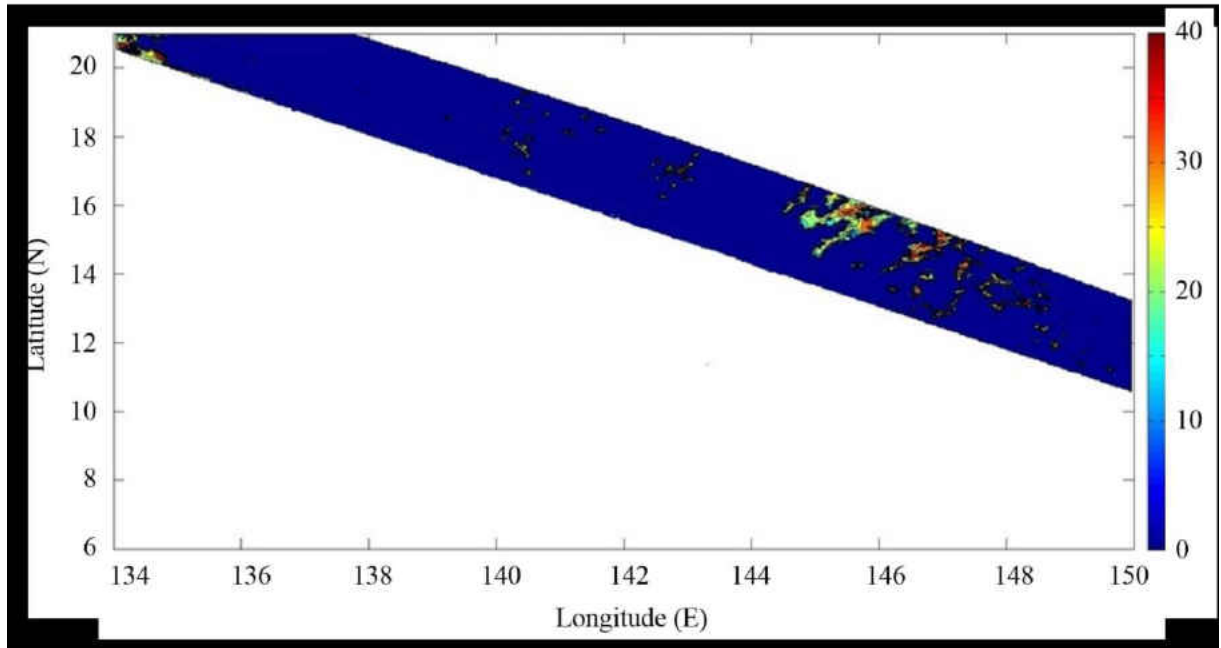


Figure 11: TRMM product 2A25 near surface reflectivity swath through the large domain on 5 August 2005.

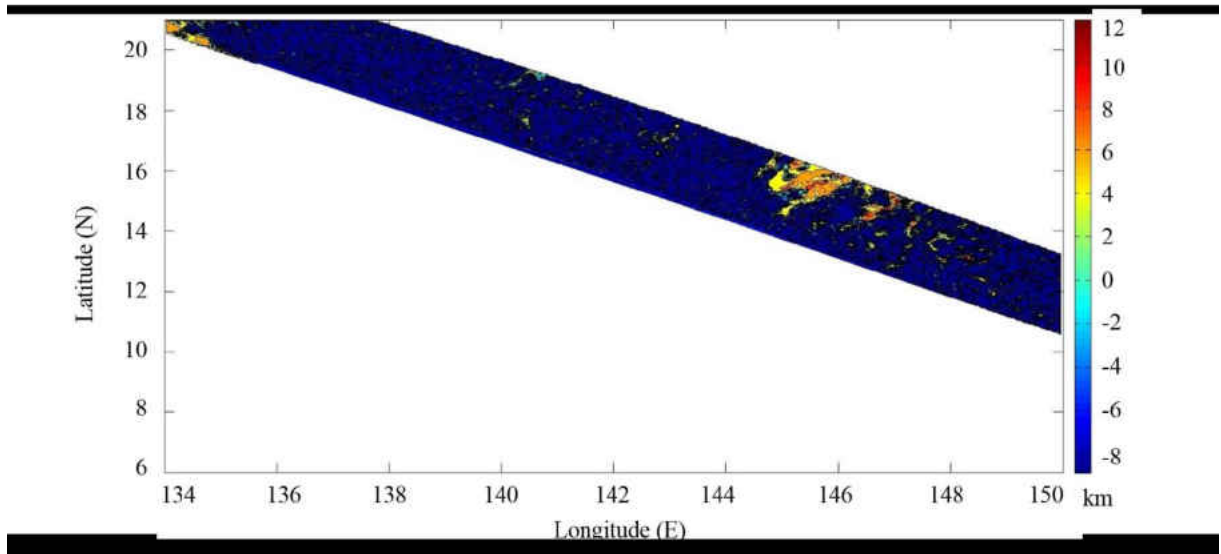


Figure 12: TRMM product 2A23 storm top height swath through the large domain on 5 August 2005.

Table 7: Summary of data grid spacing.

Domain	Data Type		Original Grid Spacing (km)	Interpolated Grid Spacing(km)
Small Radar	PGUA	N0R	1.266	N/A
	PGUA	NET	4.00	1.266
Small Radar	TRMM	2A25 NS	~4.00	1.266
Small Radar	TRMM	2A23 ST	~4.00	1.266
Large	TRMM	2A23 NS	~4.00	4.00
Large	TRMM	2A23 ST	~4.00	4.00

3.2 Identification of Objects Using Method for Object-Based Diagnostic Evaluation

To complete the storm classification, regions of interest (objects) need to be identified in the reflectivity data from the ground and satellite radars. To accomplish the object identification, reflectivity NetCDF data files are converted into a gridded format that is in the Method for Object-Based Diagnostic Evaluation (MODE; e.g. Developmental Testbed Center 2013) software by linearly interpolating to the model resolution. Using MODE, reflectivity data are resolved into objects by convolution thresholding. The thresholds that were altered in the configuration file of MODE are the raw threshold, convolution radius and the convolution threshold. The raw threshold is used to threshold the raw observation field, in this case reflectivity. The convolution radius is defined as the radius of the circular convolution applied to smooth the raw fields in this case the reflectivity data. The convolution threshold is defined as the threshold value that is applied to the convolved field in order to define objects. Table 8 displays the MODE thresholds used for both the ground-based and satellite-based classifications. Several properties about each individual object are calculated and documented. These properties include total area, length, width, axis angle, central location, and original reflectivity values. Fig. 13 shows an example of MODE output for TRMM data for two sequential swaths from 16 August 2005 within the large domain. For the first swath at 10 UTC, 15 objects were identified by MODE and eight were evaluated at 17 UTC.

Table 8: Method for Object-Based Diagnostic Evaluation Configuration file.

MODE Configuration	
Threshold	Length (km)
Convolution Radius	6.33
Convolution Threshold	5.06
Raw Threshold	≥ 6.33

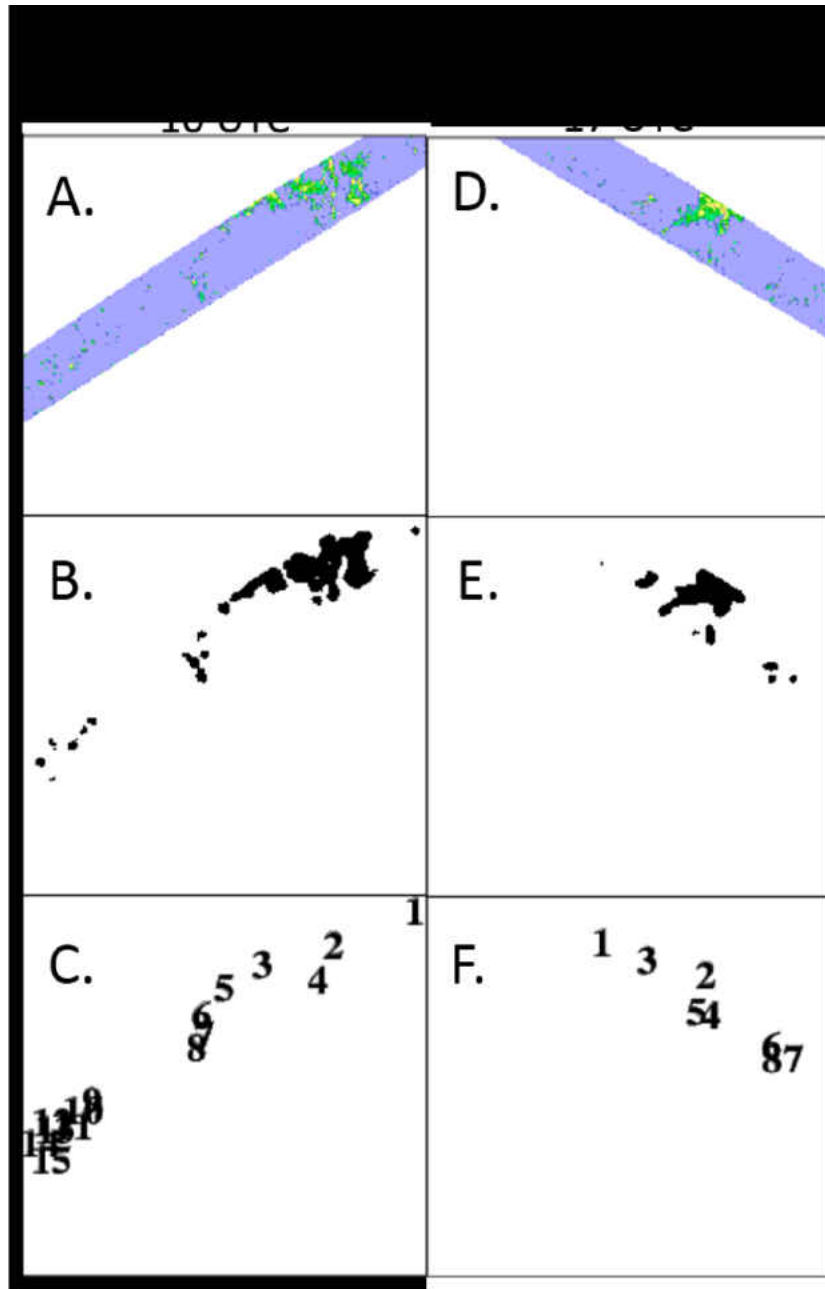


Figure 13: Example object identifications using the Method for Object-Based Diagnostic Evaluation for 16 August 2005 at 10 UTC and 17 UCT. A and D represent TRMM 2A25 near surface radar reflectivity within the large domain. B and E represent objects identified in the TRMM 2A25 data using MODE. C and F show the numerical value assigned to each object using MODE.

3.3 Storm Type Classification

After objects are created using MODE, each grid square within each object is classified into either convective or stratiform by setting reflectivity thresholds similar to the Steiner Method. Any point that exceeds 40 dBZ is considered convective and any point that is less than 40 dBZ is considered stratiform (Steiner et al. 1995). In addition, echo top heights are also used as a threshold to further classify convective regions. An echo top is defined in this study as the highest height of 18 dBZ within a storm. Five height thresholds were chosen based on height thresholds used in previous studies of convection in sub-tropical and tropical regions using various remote sensing instruments (Table 9). Liu et al. (2007) defined intense convection as any storm that has an echo top height between 10 and 14 km as indicated from TRMM data. Furthermore, deep convection was defined by Stephans and Wood (2007) as any storm with an echo top heights greater than 5 km and shallow convection as any storm with echo top heights less than 5 km. Lastly, Masunagai et al. (2005) defined deep convection as any storm with echo top heights greater than 6 km. Therefore, in this study a storm is considered Low if the echo top height is less than 6 km; a storm is considered Middle if the echo top height is between 6 and 10 km; and a storm is considered Upper if the echo top height is between 10 and 14 km. A storm is considered TTL (tropical tropopause layer) if the echo top height is between 14 and 18 km, which coincides with the height of the TTL in the tropics. Lastly, a storm is considered Stratosphere if the echo top height is greater or equal to 18 km, which is representative of typical lower stratosphere boundary layer height in the tropics. A summary of echo top height thresholds is provided in Table 10. Finally, object length is also used to classify storms, such that any object with a length greater or equal to 100 km is classified as an MCS or tropical cyclone. Because this classification is being

performed in a limited domain, the edges of the domain are a potential source of error. More specifically, the properties of these storms that exist past the edge of the domain are completely unknown, possibly leading to improper classification. To address this issue, for the ground-based radar a separate classification is also performed where storms on the edge are excluded from the classification. However, because TRMM swaths are limited temporally and spatially, no storms on the edge are excluded from the classifications.

Table 9: Previous studies that used echo top height thresholds for classification purposes.

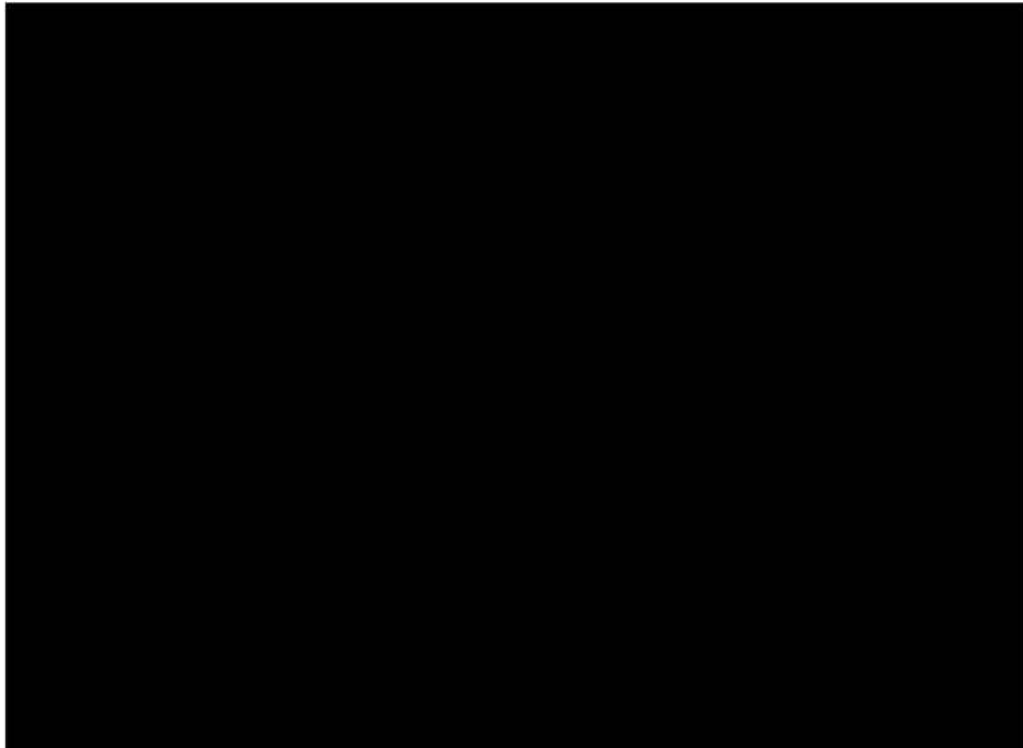


Table 10: Storm height thresholds in km and kft used in this study. TTL represents the tropical tropopause layer.

Storm Height Class	Height	
	km	kft
Low	<6	<20
Middle	$6 \leq x < 10$	$20 \leq x < 33$
Upper	$10 \leq x < 14$	$33 \leq x < 46$
TTL	$14 \leq x < 18$	$46 \leq x < 59$
Stratosphere	$x \geq 18$	$x \geq 59$

In summary, objects are either classified as shallow stratiform regions, Isolated, MCSs, or tropical cyclones. Subsets of these four storm types are also classified based on echo top heights. Shallow stratiform regions are classified if an object has no convective area and has echo top height less than 6 km. Objects are classified as Isolated Low when a convective area is present and echo top heights are less than 6 km, representing isolated shallow convection. Objects are classified as Isolated Middle when a convective area is present and echo top heights are greater or equal to 6 km but less than 10 km. When a convective region is present and echo top heights are greater or equal to 10 km but less than 14 km, an object is classified as Isolated Upper. Objects are classified as Isolated TTL when a convective region is present and echo top heights are greater or equal to 14 km but less than 18 km. Finally, objects are classified as Isolated Stratosphere when a convective region is present and echo top heights are greater than 18 km. Storms classified as Isolated with echo top heights greater than 6 km represent isolated deep storms. The same convective area and echo top height thresholds are implemented for the classification of MCSs, with the addition of the 100 km object length criteria. A summary of the thresholds used to determine storm types and the subtypes of storms is provided in Table 11. An example classification is demonstrated for 16 August 2005 (Fig. 13).

The classification of all 15 objects from the 10 UTC TRMM swath on 16 August 2005 in the large domain determined that 9 objects were shallow stratiform regions, 1 single object was Isolated Middle, 2 objects were Isolated Upper, 1 single object was MCS Middle, and the remaining 2 objects were MCS TTL. Likewise, the classification of storms for the 17 UTC TRMM swath determined that of the 8 objects, 4 were shallow stratiform regions, 3 were Isolated Upper, and the remaining object was an MCS TTL.

Table 11: A summary of the storm type classification thresholds. ET represents the echo top height of each grid point and TTL represents the tropical tropopause layer. The blue shading represents how each object is classified.

Following the classification of each object into individual storm types, the occurrence frequency for each storm type occurs was calculated. For example, using the two TRMM swaths on 16 August 2005, shallow stratiform regions are present in the domain 100% of the time, as is Isolated Upper storms, and MCS TTL. Moreover, Isolated Middle and MCS Middle were present in the domain 50% of the time. In addition, the percentage of total area covered by each storm type was calculated to

deduce which storm type occupies more than 12.5% of the domain most frequently and how often the total area of all convection occupies more than 60% of the domain. For instance, using the classification of two TRMM swaths on 16 August 2005, only the area of MCS TTL covered more than 12.5% of the domain and this only happened 50% of the time. Because TRMM swaths only cover portions of the entire domains, the percentage of area covered by each storm type is determined relative to the area of the swath. A threshold of 12.5% of total area covered is used to distinguish between clear skies to greater than few clouds in the sky. A threshold of 60% is used because the Federal Aviation Administration does not allow flights into regions where thunderstorm coverage is greater than six-tenths. The purpose of these calculations is to determine which storm type is most frequent and potentially hazardous to aviation. In addition, such quantification is necessary to determine if analyses using ground-based radar data and satellite-based radar data produce statistically similar results. To determine if the results of the climatologies are statistically significant, two tailed proportions tests with 95% confidence are used.

3.4 Model Configuration and Setup

The Advanced Research WRF (ARW) model version 3.5 with two-way nested domains is used to simulate storms that occurred near Guam (Fig. 14) on 5-6 August 5, 2005. Convection was actively present in the small PGUA radar domain during this time period, and echo top heights were generally between 6-10 km, although echo tops near 14 km were present towards the beginning of the time period. A discussion of how the case study period was selected is presented in Chapter 5. The outermost domain encompassed 2.30-27.71 °N, 130.17-173.15 °E and has a horizontal grid spacing of 15 km; the middle domain covered 7.49-20.73 °N, 136.71-160.12 °E with a horizontal grid spacing of 5 km; and the innermost domain is centered about

the PGUA radar site, and covered 10.02-17.94 °N to 139.99-149.96 °E, with a horizontal grid spacing of 1.66 km. The area of the inner domain is approximately $5.8 \times 10^5 \text{ km}^2$. The model top is set to 10 hPa (approximately 30 km) and a damping layer 5000 m deep is used at the model top. Multiple simulations are conducted with changes in vertical resolution and microphysics for various run times. Simulations are initialized at 00 UTC with ERA-Interim (ECMWF Reanalysis) global atmospheric reanalysis data which has 60 pressure levels and 80 km spatial resolution (Berrisford et al. 2011), and provided boundary conditions for the parent domain. Because there have been a limited number of tropical studies involving WRF simulations thus far, this is important to determine the model configuration that most accurately simulates tropical storms. Simulated reflectivity at 1 km altitude and echo top heights are used to determine if simulated storm morphology and areal coverage is similar to the radar observations from the same period. The results of these sensitivity tests are discussed below. Once the most accurate configuration and parameters were identified, a 48 hour simulation is performed, followed by the estimation of turbulence.

3.4.2. Model Sensitivity Analysis

Sensitivity tests are performed to assess the accuracy of simulated convective storm morphology and areal coverage of convection, which are evaluated using radar observations. Model parameters that were altered in the simulations include vertical grid spacing and the microphysics scheme, which influence how convection is resolved, as well as the strength and duration. Furthermore, the same cumulus, planetary boundary layer (PBL), shortwave and longwave radiation, surface layer, and land surface parameterizations are used in each simulation. More specifically, the Kain-Fritsch scheme is used for the cumulus parameterization in domains 1 and 2, and the Yonsei University scheme is used for planetary boundary layer (PBL) physics. The Rapid Radiation Transfer Model (RRTM) scheme is used for longwave radiation parameterization and the Dudhia scheme is used for shortwave

radiation parameterization. The surface layer is parameterized using the Mesoscale Model version 5 (MM5) similarity scheme, and the Noah Land Surface Model is used to parameterize the land surface. A summary of the specific parameterizations used in each simulation is provided in Table 12.

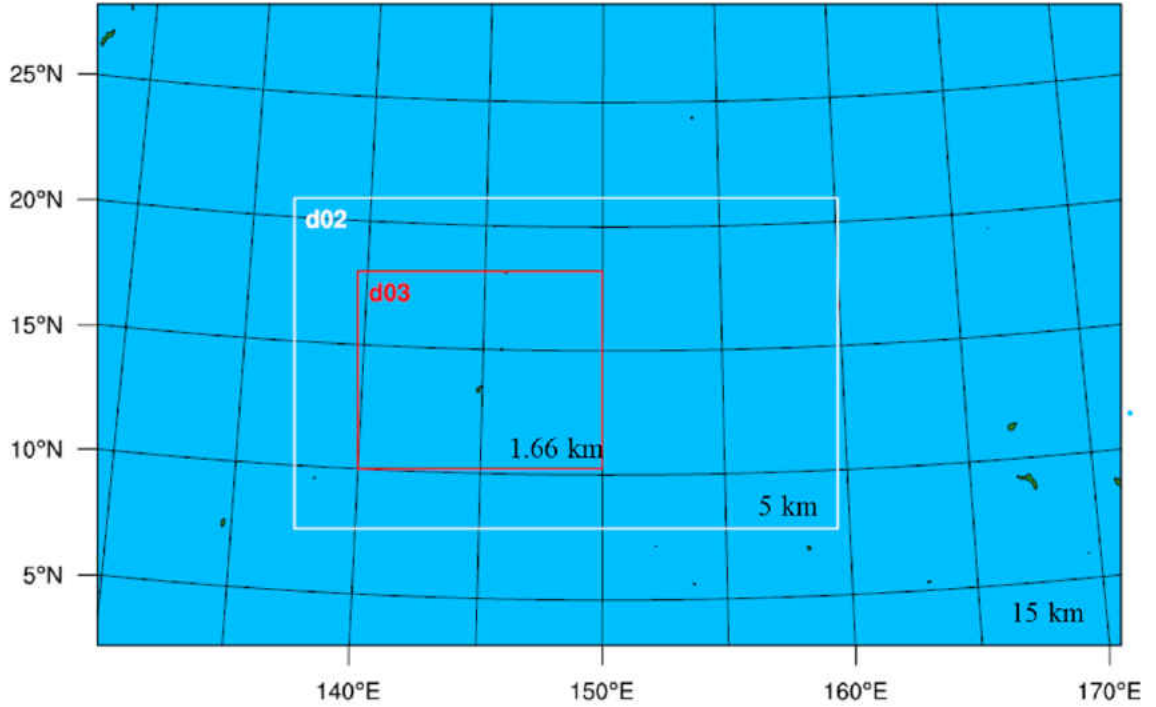


Figure 14: Location of model domains with horizontal grid spacing. Domain 1 has a horizontal grid spacing of 15 km, domain 2 5 km, and domain 3 1.67 km.

3.5 Model Sensitivity Analysis

Sensitivity tests are performed to assess the accuracy of simulated convective storm morphology and areal coverage of convection, which are evaluated using radar observations. Model parameters that were altered in the simulations include vertical grid spacing and the microphysics scheme, which influence how convection is resolved, as well as the strength and duration. Furthermore, the same cumulus, planetary boundary layer (PBL), shortwave and longwave radiation, surface layer, and

land surface parameterizations are used in each simulation. More specifically, the Kain-Fritsch scheme is used for the cumulus parameterization in domains 1 and 2, and the Yonsei University scheme is used for planetary boundary layer (PBL) physics. The Rapid Radiation Transfer Model (RRTM) scheme is used for longwave radiation parameterization and the Dudhia scheme is used for shortwave radiation parameterization. The surface layer is parameterized using the Mesoscale Model version 5 (MM5) similarity scheme, and the Noah Land Surface Model is used to parameterize the land surface. A summary of the specific parameterizations used in each simulation is provided in Table 12.

3.5.1 Simulation 1

Simulation 1 is run for a 24 hour period beginning at 00 UTC on 5 August 2005 and uses the suite of parameters previously discussed with the addition of WRF-Single Moment 6-Class (WSM6) for the microphysics scheme. Furthermore, this simulation utilizes 55 vertical levels. Simulation 1 produces an abundance of convective features that begin to propagate through the domain near the fifth hour of simulation time (Fig. 15). These features are evenly spaced and equal in size indicating that they are numerical noise. By the eleventh hour of the simulation small convective features are present in the majority of the domain and are representative of true convection. However at the same time larger storms near the southern boundary begin to form and strengthen with little propagation, which may indicate possible boundary issues. Small cellular storms continue to be present in the domain for the remainder of the simulation, with the addition of larger cells in a linear orientation east of Guam after the twentieth simulation hour that continue to propagate westward. This simulation indicates that a spin up time greater than 6 hours is needed. In addition, echo top heights are similar to those observed using radar during this time, with a few storms

Table 12: Model setup.

Simulation	Duration(hours)	Parameterizations							Number of Vertical Levels
		Microphysics	Cumulus	LW Radiation	SW Radiation	Surface Layer	Land Surface	Planetary Boundary Layer	
1	24	WSM-6	Kain-Fritsch	RRTM	Dudhia	MM5 Similarity	Noah Land Surface Model	YSU	55
2	12	WSM-6	Kain-Fritsch	RRTM	Dudhia	MM5 Similarity	Noah Land Surface Model	YSU	75
3	6	WDM-6	Kain-Fritsch	RRTM	Dudhia	MM5 Similarity	Noah Land Surface Model	YSU	100
4	12	WDM-6	Kain-Fritsch	RRTM	Dudhia	MM5 Similarity	Noah Land Surface Model	YSU	75
5	24	WDM-6	Kain-Fritsch	RRTM	Dudhia	MM5 Similarity	Noah Land Surface Model	YSU	75
6	48	WDM-6	Kain-Fritsch	RRTM	Dudhia	MM5 Similarity	Noah Land Surface Model	YSU	75

reaching 14 km but the majority of storms having echo top heights between 10 and 12 km (Fig. 16).

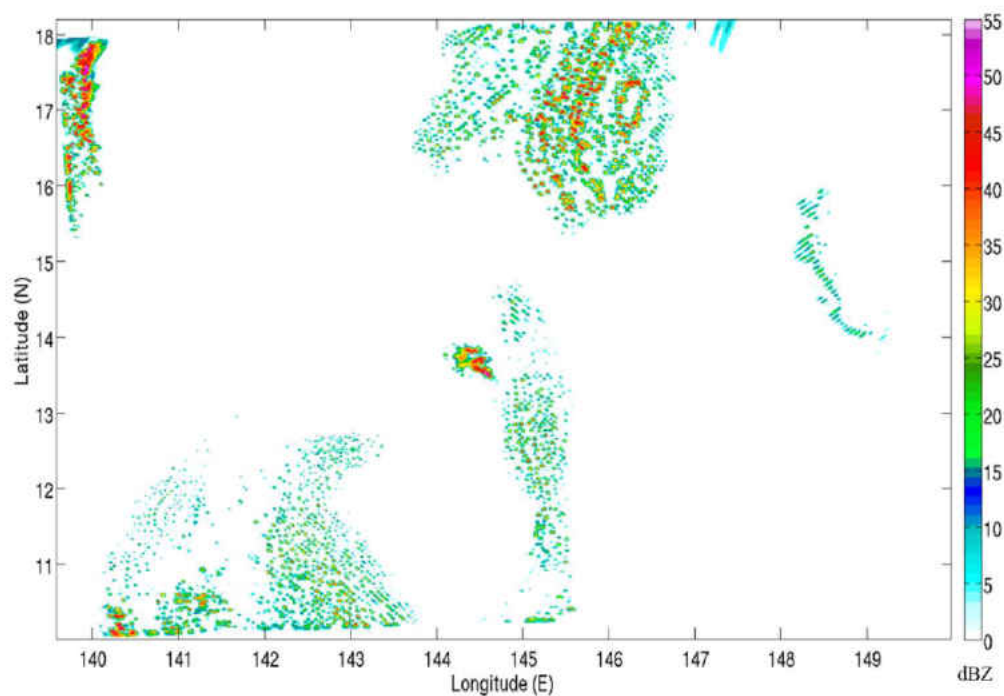


Figure 15: Simulated 1 km reflectivity on 5 August 2005 at 5:00 UTC for Simulation 1.

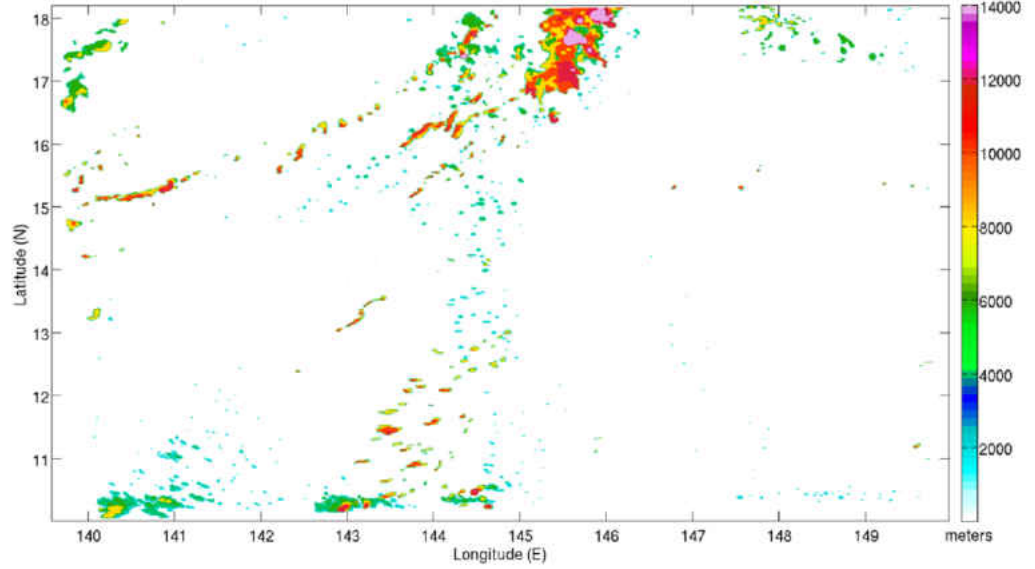


Figure 16: Echo top height calculated using an 18 dBZ threshold for Simulation 1 on 5 August 2005 at 10:00 UTC.

3.5.2 Simulation 2

Simulation 2 covers a 12 hour period beginning at 00 UTC on 5 August 2005 and uses the same parameterizations as Simulation 1, but contains 75 vertical levels instead of 55. This simulation was only run for a 12 hour period to determine the increase in computational time associated with using a more vertical levels. In Simulation 2, the 1 km reflectivity field once again shows small convective features similar to Simulation 1 that are evenly spaced at the fifth hour of simulation time, and therefore are concluded to be numerical noise. By the tenth hour, the majority of numerical features have dissipated and small convective cells with larger cells near the southern boundary are present. Echo top heights are similar to those from radar observations in Simulation 2, as most storms have echo top heights that are less than 10 km while a limited amount of storms reach 14 km (Fig. 17). This simulation indicates that increasing the vertical resolution does not improve the issue of numerical

noise during the beginning hours of the simulation but does produce echo heights that are more representative of those observed using radar.

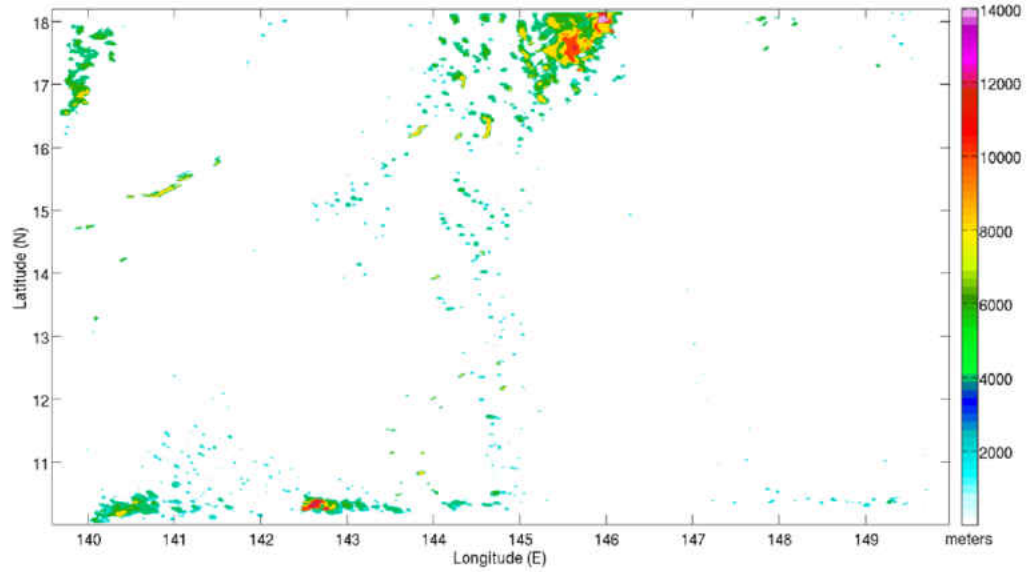


Figure 17: Echo top height calculated using an 18 dBZ threshold for Simulation 2 on 5 August 2005 at 10:00 UTC.

3.5.3 Simulation 3

Simulation 3 is run for a 6 hour period and uses the same physics as Simulation 1, with the exception of the microphysical scheme, which was changed from WSM6 to the WRF-Double Moment 6-Class (WDM6) scheme. The vertical resolution of Simulation 3 is also increased that 100 vertical levels are used. One hundred vertical levels was chosen in order to determine if increasing the vertical resolution would reduce numerical noise and more accurately simulate convection. In Simulation 3, the numerical noise that was found in both Simulations 1 and 2 was no longer present (Fig. 18). However, due to the necessary increase in computation time and power, the increased vertical resolution is not a feasible choice for this study.

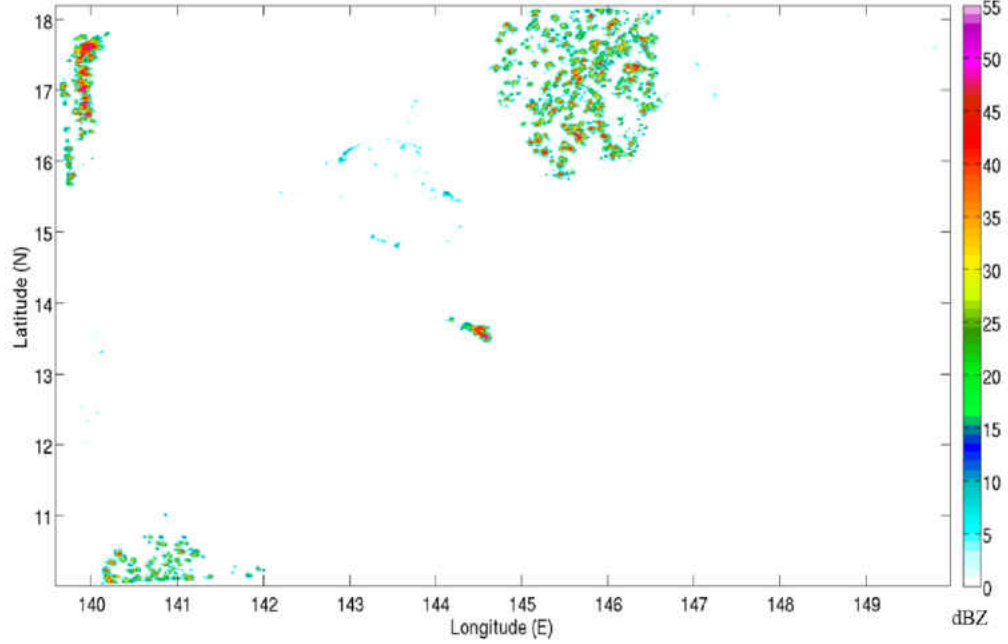


Figure 18: Simulated 1 km reflectivity on 5 August 2005 at 5:00 UTC for Simulation 3.

3.5.4 Simulations 4 and 5

Simulations 4 and 5 are run for a 12 and 24 hour period and use the same physics as Simulation 3, but utilize 75 vertical levels. The results from Simulation 4 indicate that altering the microphysics to WDM6 does influence the simulated convection. Compared to the previous simulations, Simulation 4 reduces the numerical noise and reduces the number of abundant small convective cells early in the simulation. The amount of convection does decrease throughout the period, which was the case after 09 UTC in the PGUA observations. Furthermore, storms that are near the southern boundary did not enter the domain until the ninth hour of the simulation and are weaker in intensity. Lastly, echo top heights are once again representative of those observed using radar (Fig. 19) especially later in the period as convection become shallower in depth. These results indicate that using WDM6 for the mi-

crophysical parameterization with 75 vertical levels enables accurate simulation of convection for the specified time period. To further confirm that these settings were appropriate, Simulation 5 was run for 24 hours beginning at 00 UTC on 5 August 2005. This simulation showed the same transition of more convective features towards the beginning of the run and then a transition to weaker deep convection to more shallow convection. Afterwards, an increase in amount of convection was simulated towards the end of the period, possibly depicting the diurnal cycle. This agrees with the radar observations and the classification of storm types from this time period. Interestingly, as Simulation 5 continues past hour 15, convection on the southern boundary begins to propagate slowly towards the northwest and decreases in areal size. The settings for Simulation 5 are used for an analysis run (Simulation 6), which is run for 48 hours beginning at 00:00 UTC on 5 August 2005 and is discussed further in Chapter 5.

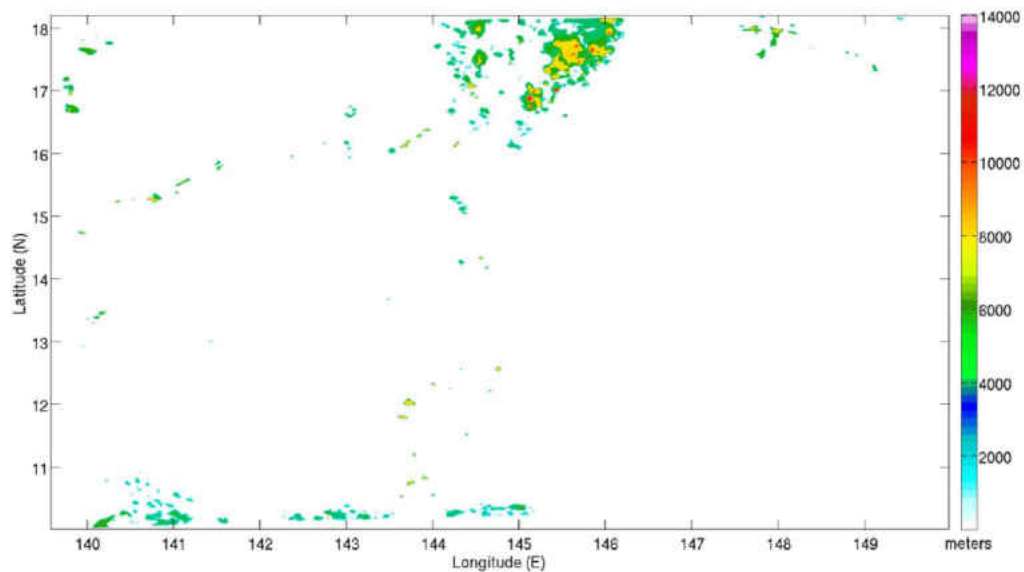


Figure 19: Echo top height calculated using an 18 dBZ threshold for Simulation 4 on 5 August 2005 at 10:00 UTC.

3.6 Turbulence Calculation

In order to estimate the intensity of turbulence in model simulations, the Ellrod and Knapp method (Ellrod and Knapp 1992) is applied. The Ellrod Index is commonly used to forecast turbulence in aviation operations in the U.S. (Fig. 20). Two equations that can be used in the estimation of turbulence: Turbulence Index 1 (TI1) which is given by

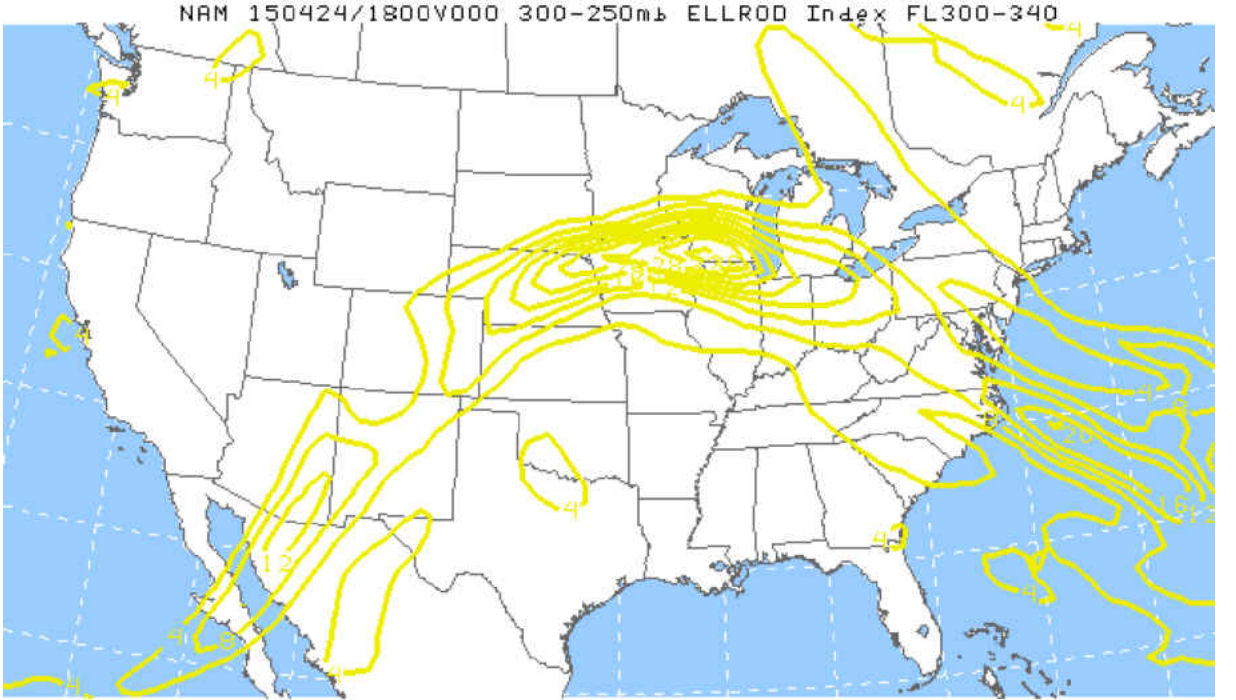


Figure 20: An example of a turbulence forecast estimated by the Ellrod Index for the continental United States for flight levels 30,000 ft to 34,000 ft on 24 April, 2015 (Aviation Weather Center)

$$TI1 = VSH \times DEF [s^{-2}], \quad (3.1)$$

and Turbulence Index 2 (TI2) which is given by

$$TI2 = VSH \times [DEF + CVG] [s^{-2}], \quad (3.2)$$

where VSH is vertical wind shear, DEF is deformation, and CVG is convergence, as defined in equations

$$VSH = \frac{(\Delta u^2 + \Delta v^2)^{1/2}}{\Delta z}, \quad (3.3)$$

where u and v are the horizontal wind components and Δz is the thickness between pressure levels,

$$DEF = (DST^2 + DSH^2)^{1/2}, \quad (3.4)$$

$$DST = \frac{\partial u}{\partial x} - \frac{\partial v}{\partial y}, \quad (3.5)$$

$$DSH = \frac{\partial v}{\partial x} + \frac{\partial u}{\partial y}, \quad (3.6)$$

and

$$CVG = -\left(\frac{\partial u}{\partial x} + \frac{\partial v}{\partial y}\right). \quad (3.7)$$

TI2 is used by the Air Force Weather Agency (AFWA) turbulence diagnostics and other aviation applications (Creighton et al. 2014; Aviation Weather Center 2015; Ellrod and Knapp 1992) and was calculated in this study. TI2 was chosen over TI1 because it is an output for both the Air Forces version of WRF and the Aviation Weather Center, and furthermore is a product available to all pilots. A threshold value representative of light-moderate turbulence is $4 \times 10^{-7} \text{ s}^{-2}$, while $8 \times 10^{-7} \text{ s}^{-2}$ represents moderate turbulence, and $12 \times 10^{-7} \text{ s}^{-2}$ corresponds to moderate-severe turbulence (Ellrod and Knapp 1992; Creighton et al. 2014; Aviation Weather Center 2015). In this study, TI2 was calculated to determine the strength and extent of turbulence at various heights around simulated storms.

CHAPTER 4

RESULTS AND DISCUSSION: WESTERN TROPICAL PACIFIC OBSERVED STORM CLIMATOLOGY

4.1 Sensitivity of the Ground-based Radar Storm Climatology Using Three Different Methods

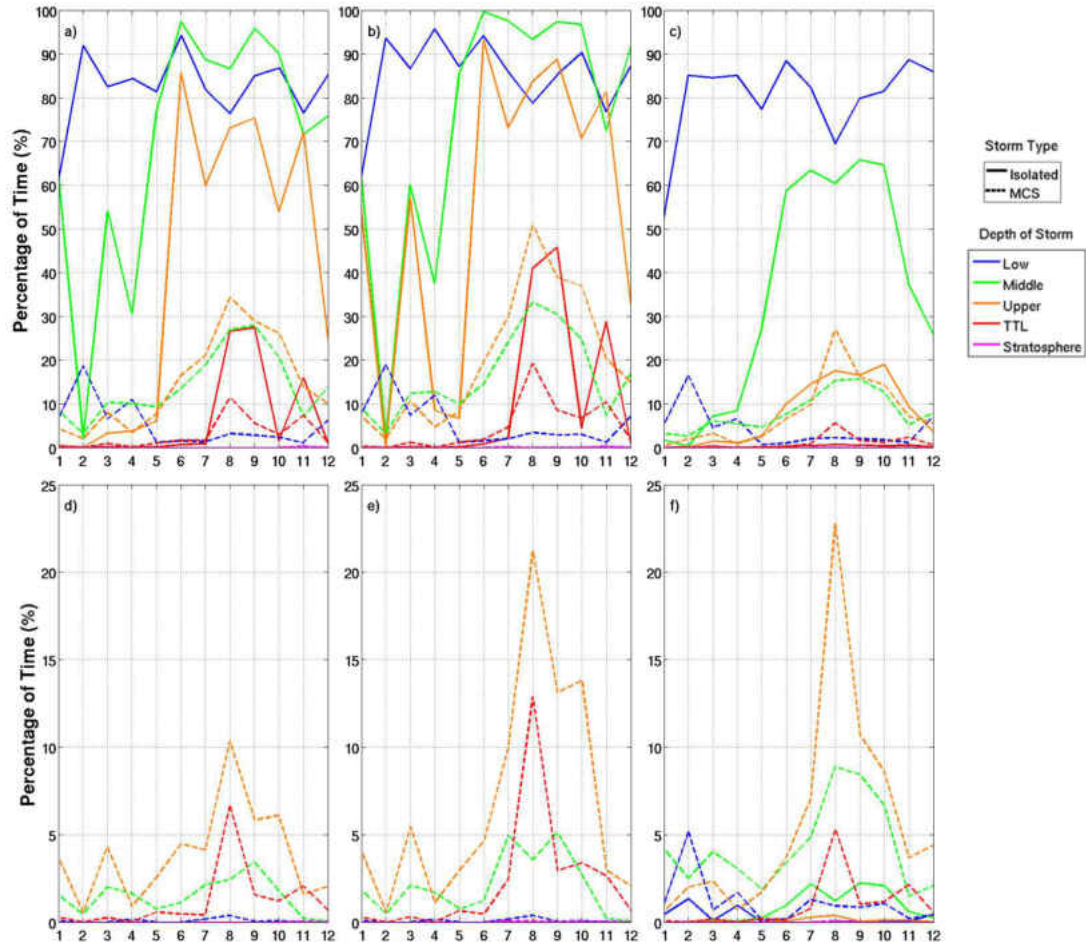
The number of observations for the ground-based radar classification for the years 2005, 2010, and 2011 are shown in Table 6. Three separate ground-based radar classifications were created using two different domain sizes and by either flagging or not flagging storms on the edge of the domain. As previously stated in Section 3.3, four types were classified: shallow stratiform, isolated convection (shallow and deep), MCS, and tropical cyclones. However, shallow stratiform does not significantly impact high altitude turbulence, so shallow stratiform statistics will not be presented. In addition, during the study years chosen, tropical cyclones never progressed into the radar domain (National Climatic Data Center Storms Event Data Base 2014), and therefore will not be classified or discussed.

In order to determine the most appropriate method of classifying storm types using only base radar reflectivity and echo top height data, three sensitivity tests were performed for 2005. The first classification of storms excluded storms on the edge of the small radar domain because storm properties past the radar domain are unknown. This method will hereafter be referred to as Method 1. The second classification method was also performed in the small radar domain, but storms on the edge of the domain were included. This method will hereafter be referred to as Method 2. The third method classified all storms within 115 km of the radar

site, hereafter referred to as Method 3. More specifically, Method 3 does include those storms on the edge of the domain in the classification because of the restricted domain area. Furthermore, 115 km was chosen as the radius of the domain because it is half the radius utilized in Methods 1 and 2. The purpose of the Method 3 classification was to determine if the height of base reflectivity data causes any biases in the classification. To remind the reader, the depths of storms are listed in Table 10. In the first analysis the percentage of time isolated storms and MCSs are present in the radar domain is considered. The percentage of time storms are in the domain is important for aviation operations because flight plans and times can be adjusted based on predominant storm types. Afterward, the percentage of time that the area of convection covers more than 12.5% and 60% of the domain is examined. These percentages are important for aviation operations because lateral clearance between storms is required in the Federal Aviation Administration (FAA) avoidance policies and aviation operations are not allowed in regions where more than six-tenths of area is convective. Furthermore, the percentage of time that the total area of convection types (CT), such as isolated and MCSs with Low echo top heights, is more than 12.5% of the domain area will be identified as $P_{CT > 12.5}$. The percentage of time that the area of isolated convection and MCSs exceed 12.5% of the domain area will be referred to as $P_{IC > 12.5}$ and $P_{MCS > 12.5}$. Next, the percentage of time that the total area of all convective storms types exceeds 60% of the domain area will be identified as $P_{CONV > 60}$. Lastly, the percentage of time that the total area of all convective storms types with echo top heights greater than 6 km exceeds 60% of the domain area will be identified as $P_{DCONV > 60}$.

The first analysis to be discussed is the percentage of time that convection was classified in the small radar domain using Method 1, during 2005. This clearly demonstrates that isolated storms are most commonly present in the domain (Fig.

21a). During 2005, over 60% of the time at least one isolated storm was present. Furthermore, this analysis shows that isolated storms and MCSs with higher echo tops are more commonly present in the domain during the months of June through October.



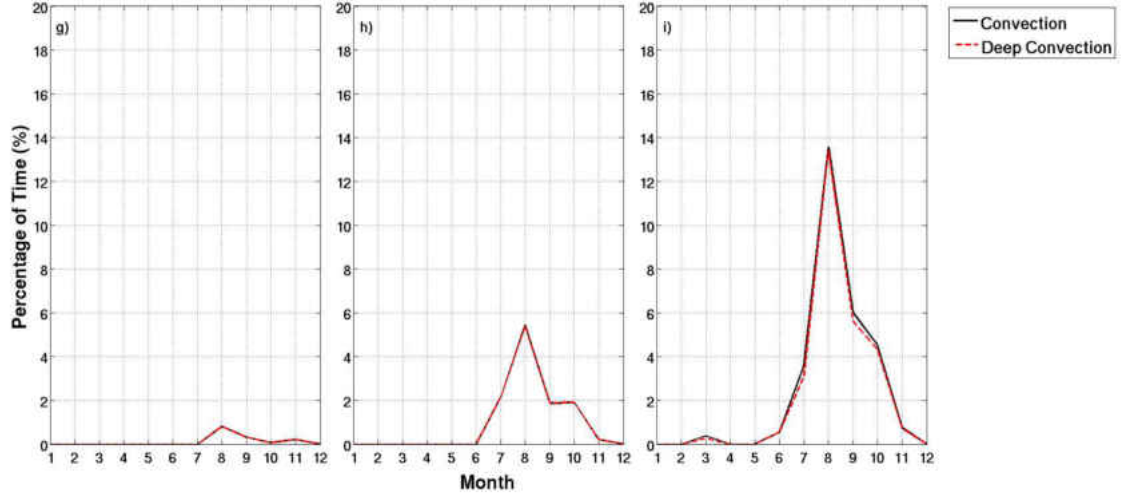


Figure 21: Percentage of time convection is present in the small radar domain during 2005 using three methods, a) Method 1, b) Method 2, and c) Method 3, and the percentage of time the area of convection exceeds 12.5% of the small radar domain area using d) Method 1, e) Method 2, and f) Method 3. The percentage of time the area of all types of convection exceeds 60% of the small radar domain g) Method 1, h) Method 2, and i) Method 3. Solid lines represent isolated storms and dashed lines represent MCSs.

The climatology of storms in 2005 using Method 2 again demonstrates that isolated storms are commonly present in the small radar domain (Fig. 21b). However, in comparison to Method 1, isolated storms and MCSs with Middle, Upper, and TTL heights are more frequently present in the domain. The percentage of time increase is most apparent for MCSs with Upper depths, increasing nearly 20% from Method 1. This increase in percentage of time is due to the fact that additional storms were on the edge of the domain in Method 1 were excluded from the classification, but are now included. As was the case for Method 1, a seasonal variation is observed for isolated storms and MCSs classified using Method 2.

Finally, the classification of storms using Method 3, when storms are only classified within 115 km of the radar site, shows lower percentages of time that isolated deep storms are present in the domain than Methods 1 and 2 (Fig. 21c). The

most noticeable difference is the decrease in percentage of time isolated deep storms with Upper and TTL echo top heights are present in the domain. This decrease in percentage of time can be attributed to an absence of these storms within 115 km of the radar site. The percentage of time MCSs are classified within 115 km of the radar domain was less than the percentage of time in both Methods 1 and 2, which is due to the spatial limitation of the domain in this method.

The second analysis is the percentage of time the area of both isolated storms and MCSs exceed 12.5% and 60% of the radar domain. As was previously mentioned, these percentages are important for aviation because aircraft not only needs to have vertical clearance around convection, but also needs horizontal clearance of convection for take-off and landing procedures. Furthermore, aircraft operations are not allowed in regions where more than six-tenths of the area is covered by convection. Examinations of storm climatologies using Methods 1 and 2 demonstrate that $P_{IC > 12.5}$ was never greater than zero. On the other hand, $P_{MCS > 12.5}$ and $P_{CONV > 60}$ was occasionally greater than zero. $P_{MCS > 12.5}$ and $P_{CONV > 60}$ was greater than zero most frequently during the summer months. Both were, however, less than 25% of the time. Lastly, in comparison to Methods 1 and 2, Method 3 demonstrates $P_{IC > 12.5}$ was often greater than zero during the summer months, but was always less than 1%. $P_{MCS > 12.5}$, $P_{CONV > 60}$, and $P_{DCONV > 60}$ using Method 3 is greater than both Methods 1 and 2. More specifically, MCSs with Middle, Upper, and TTL echo top heights exceed the area threshold most often in the summer, with a maximum near 25% of the time. This increase in percentage of time can be explained by the decrease of domain area size from approximately 166,000 km² to 41,500 km², meaning storms classified as MCSs are naturally covering more of the domain area.

4.2 Statistical Comparison of Sensitivity Tests

Determining if there are significant statistical differences between the classifications of storm types using the three different methods aids in understanding the limitations of these methods. The percentages of time convection (isolated and MCSs) was present in the domain using Methods 1 and 2 appear similar (Fig. 22a-b). Percentages of isolated storms decrease as storm depth increases, though the values are lower for Method 1 because storms on the edge were excluded. On the other hand, the percentage of time MCSs were present in the domain increases with storm depth for both methods. However, from the p-values calculated from a two-tailed proportion test with 95% confidence (Table 13), it can be concluded that there are significant statistical differences in the percentage of time convection is in the domain using Method 1 and 2, except for convection with Stratosphere depths. Furthermore, there are significant statistical differences between $P_{CT > 12.5}$, $P_{CONV > 60}$, and $P_{DCONV > 60}$ using Methods 1 and 2 (Tables 14 and 15, Fig. 22c). In summary, though qualitatively the results of Method 1 and Method 2 climatologies are similar, quantitatively, these results differ significantly.

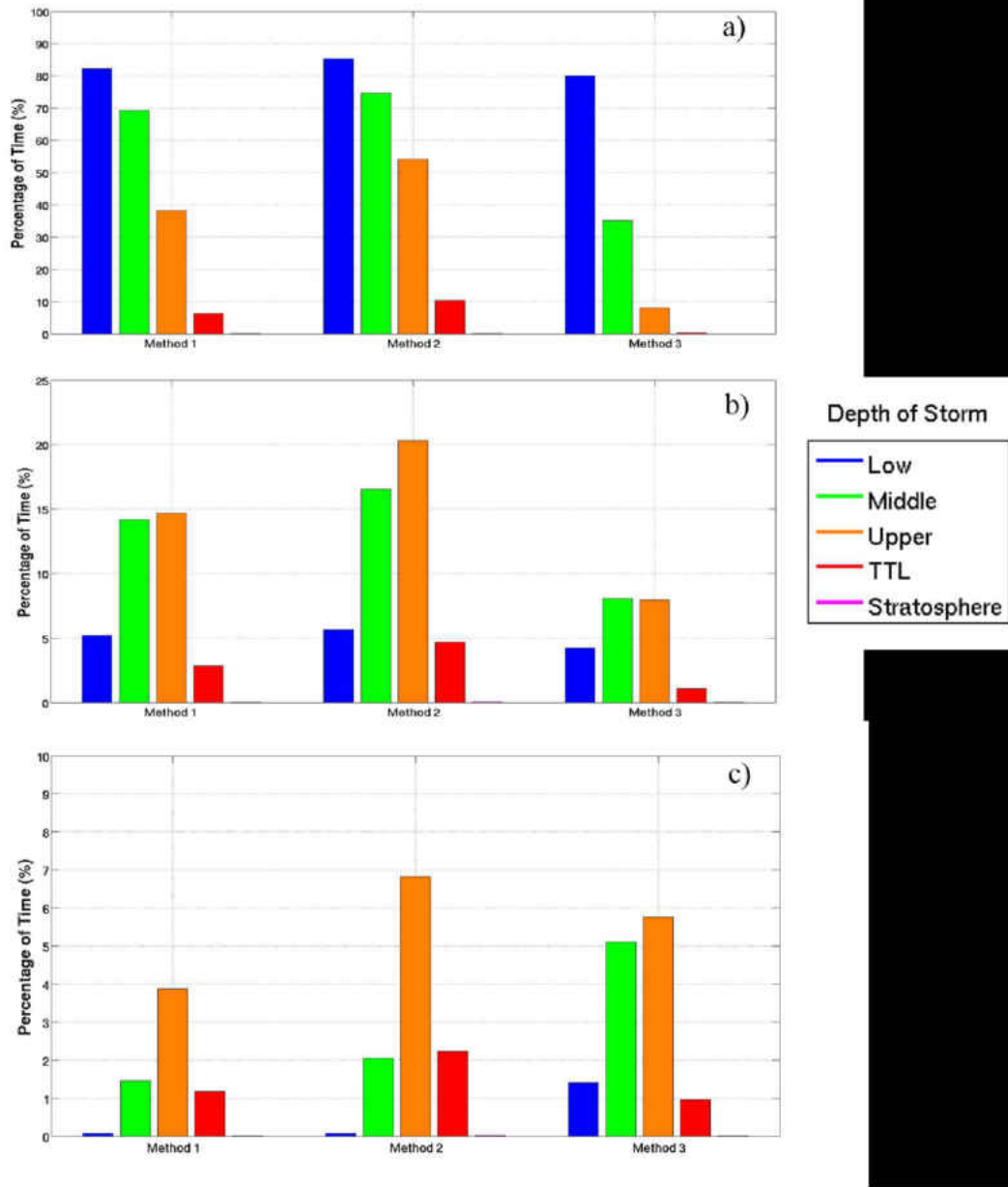


Figure 22: Percentage of time a) isolated storms and b) MCSs are present for the three methods. In c), the percentage of time the area of convection exceeds 12.5% of the domain during 2005 is illustrated

Table 13: p-values calculated from a proportion test with 95% confidence for the percentage of time convective storms are present in the small radar domain using Method 1 and Method 2 during 2005.

	Low	Middle	Upper	TTL	Stratosphere
p-value	1.61E-41	5.47E-177	9.06E-661	8.16E-113	0.2513

Table 14: p-values calculated from a proportion test with 95% confidence for the percentage of time the area of convective storms cover more than 12.5% of the small radar domain using Method 1 and Method 2 during 2005.

	Low	Middle	Upper	TTL	Stratosphere
p-value	1	3.64E-8	2.96E-58	3.60E-23	0.1025

Table 15: p-value calculated from a proportion test with 95% confidence for the percentage of time the area of all types of convective storms and only deep convective storms exceeds more than 60% of the small radar domain using Method 1 and Method 2 during 2005.

	p-value
Convection	1.97E-45
Deep Convection	3.19E-45

Determining if there are statistical differences between the 2005 classification results using Method 2 and Method 3 is also of interest (Fig. 22). Tables 16, 17, and 18 display the p-values calculated from a two-tailed proportion test with 95% confidence for the percentage of time convection is present, $P_{CT > 12.5}$, $P_{CONV > 60}$, and $P_{DCONV > 60}$. The p-values calculated from the proportion tests once again demonstrate that while qualitatively the results are similar, quantitatively there are significant statistical differences between the results from the classification using Method 2 and Method 3 for all depths except Stratosphere. The reasons for these significant differences are

related to the height of the radar beam as the radius increases from 115 km to 230 km. More specifically, the radar beam height is approximately 2 km at a range of 115 km, while at 230 km the radar beam is at an altitude of approximately 5 km, which is near the reflective freezing level. This is further confirmed by examining the classification of shallow stratiform regions using Methods 2 and 3. This analysis shows that shallow stratiform regions are present in the domain more frequently when classified using Method 3.

Table 16: p-values calculated from a proportion test with 95% confidence for the percentage of time convective storms are present within the small radar domain (Method 2) and within 115 km of the radar site (Method 3)

	Low	Middle	Upper	TTL	Stratosphere
p-value	5.89E-181	4.33E-447	<1E-1000	3.29E-208	0.0023

Table 17: p-values calculated from a proportion test with 95% confidence for the percentage of time the area of convective storms covers more than 12.5% of the small radar domain Method 2 and the domain area within 115 km of the radar site (Method 3).

	Low	Middle	Upper	TTL	Stratosphere
p-value	8.68E-70	5.57E-103	0.0004	2.94E-25	0.1797

Table 18: p-value calculated from a proportion test with 95% confidence for the percentage of time the area of all types of convective storms and deep convective storms exceeds more than 60% of the small radar domain using Method 2 and Method 3 during 2005.

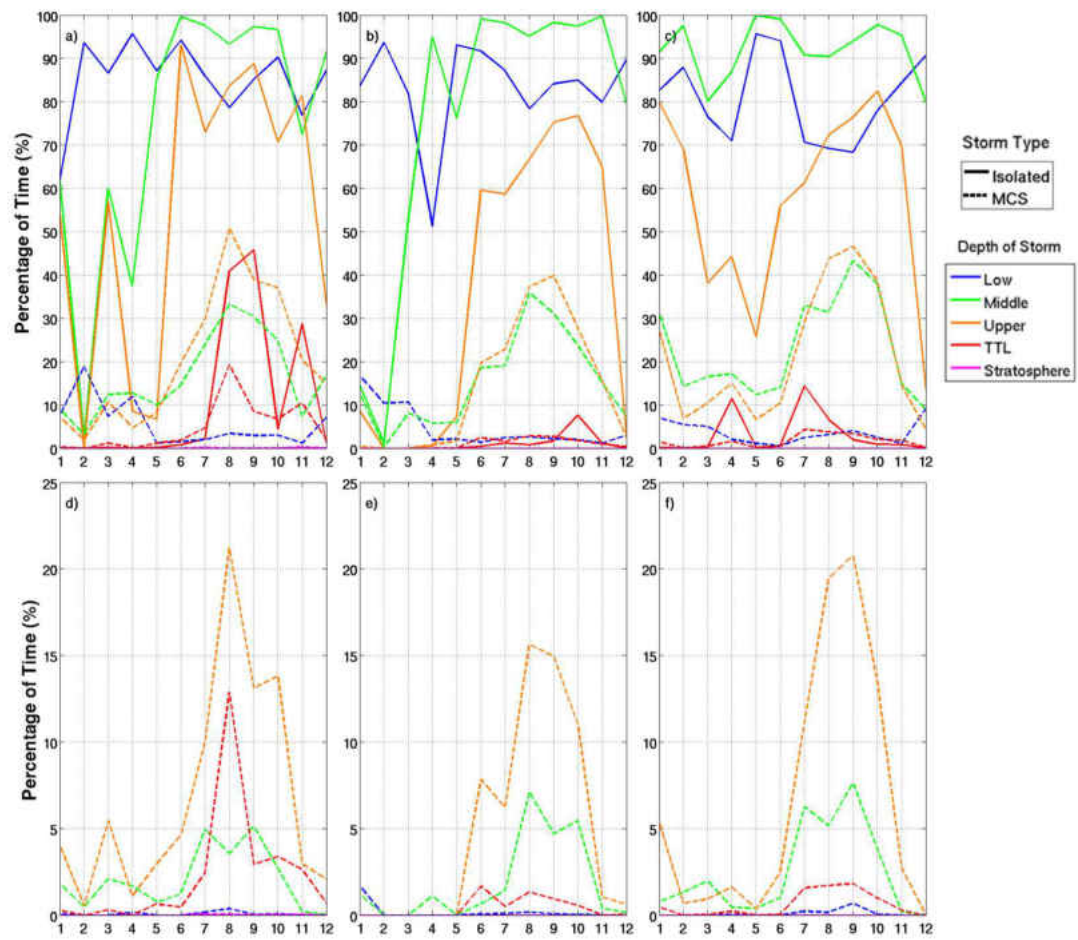
Storm Type	p-value
Convection	1.02E-44
Deep Convection	1.02E-39

Although altering the domain size and excluding storms on the edge of the domain does create significant statistical differences in the percentage of time that storms are present and cover a portion of the domain, the remainder of the study will utilize the results of Method 2. Though the classification of storms using Method 2 may be significantly different than Method 1, having at least some sense of convective type at the boundary is advantageous in an operational aviation setting, especially for vertical clearance. Furthermore, because both the ground-based and satellite-based radar data are very limited spatially and temporally, any information about storm properties is of value. Lastly, Method 2 maximizes the percentage of time storms are present in the domain, which would entail a conservative approach utilized in aviation operations.

4.3 Ground-based Radar Classification

In this section, the results of Method 2 are discussed to understand the differences between the storm climatologies from 2005, 2010, and 2011. This is an important comparison because enhanced amounts of convective features throughout a year affects aviation operations, and thus, has economic impacts. To recapitulate, 2005 was a normal year in terms of rainfall, 2010 produced below average rainfall, and 2011 produced above average rainfall near Guam. To begin, an overview of the percentage of time isolated storms and MCSs were present is provided to develop a sense of which storm type was most frequently present in the domain and if seasonal variations like that in 2005 are apparent in 2010 and 2011. In addition, $P_{\text{DCT} > 12.5}$, $P_{\text{CONV} > 60}$, $P_{\text{DCONV} > 60}$ are discussed. Afterwards, the difference in the percentage of time convective storms were present in the domain between 2005, 2010, and 2011 is presented.

The storm type climatology for the years 2005, 2010, and 2011 (Fig. 23), indicates that isolated storms with Low and Middle echo top heights occur frequently year round, while the presence of isolated with Upper and TTL echo top heights peak during the summer and fall. The percentage of time MCSs with higher echo top heights are present in the domain during these years clearly shows that MCSs are much less common than isolated storms during the first six months of the year. Furthermore, after June, the percentage of time MCSs are present increases to maximum values during the summer months. In summary, isolated storms and MCSs with higher echo top heights are more frequent in the summer months. With regard to areal coverage, the area of isolated storms is never greater than 12.5% of the domain. On the other hand, the area of MCSs frequently exceeds 12.5% of the domain. This is especially true June through October for MCSs with Middle and Upper echo top heights. Furthermore, more than 60% of the domain was covered by convection most often during the summer months.



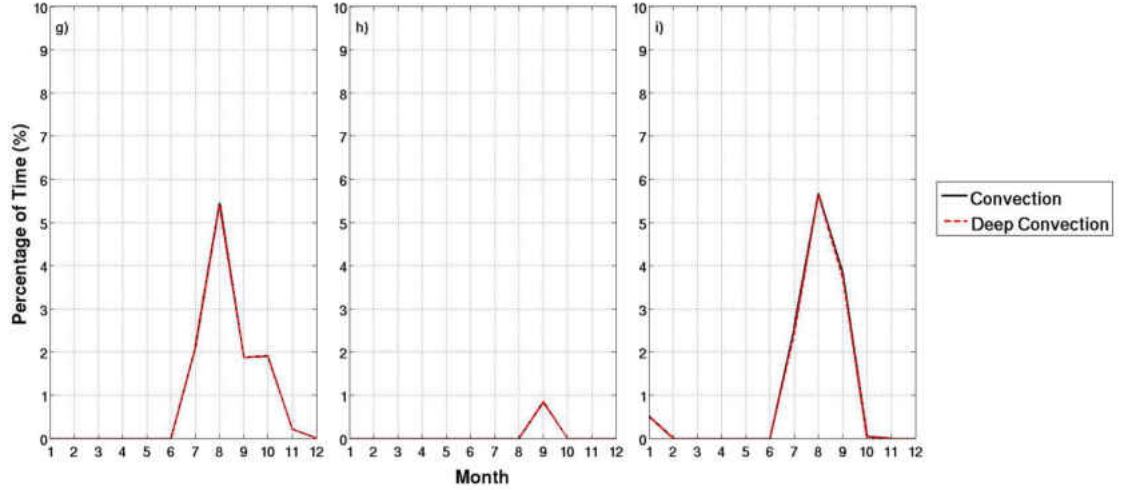


Figure 23: Percentage of time convection is present using ground-based radar within the small radar domain (Method 2) during a) 2005, b) 2010, c) 2011. d-f) Percentage of time the area of convection exceeds 12.5% of the domain area during 2005, 2010, and 2011. g-i) Percentage of time the area of convection (all types of isolated deep and MCSs) and only deep convection exceeds 60% of the small radar domain during 2005, 2010, and 2011. Solid lines represent isolated deep storms and dashed lines represent MCSs.

Evidence of annual variability is present in Fig. 23. For example, the percentage of time convective storms were present in the small radar domain during 2010 is subtracted from 2005 because 2010 had below average rainfall (Fig. 24a). In general it is observed that the percentage of time isolated storms were present in the domain was greater for 2005 than 2010, especially for isolated with Upper and TTL echo top heights (Fig. 24). This higher percentage during 2005 also occurs for MCSs with Upper and TTL heights (Fig. 25a). This suggests that convective storms with higher echo top heights are present in the small radar domain less often during a below-average rainfall year. On the other hand, weaker storms occur as often or more often during a below average rainfall year. Secondly, the difference in the percentage of time convective storms were present in the domain between 2005 and 2011 is provided in Figs. 24b and 25b. In this case, because 2011 is above average, the percentage of time

convective storms were present in the domain during 2005 is subtracted from 2011. It is clear that during the winter and spring of 2011 the percentage of time isolated storms and MCSs are present is greater than in 2005. However, during the summer the opposite is true. This may indicate that the enhanced precipitation during the winter and spring led to greater precipitation amounts during 2011. In addition, this may also suggest that during years when greater precipitation is predicted, aviation should be more concerned during the winter and spring (discussed further in Section 4.6.1). Relative to 2010, 2011 also had a higher occurrence of isolated storms during the winter and spring (Fig. 24c). To summarize, isolated storms and MCSs with higher echo top heights were more commonly found in the domain in 2005 than in 2010 (Fig. 24a). Furthermore, in 2011, there was a higher percentage of convection in the domain during the winter and spring months when compared to 2005 and 2010.

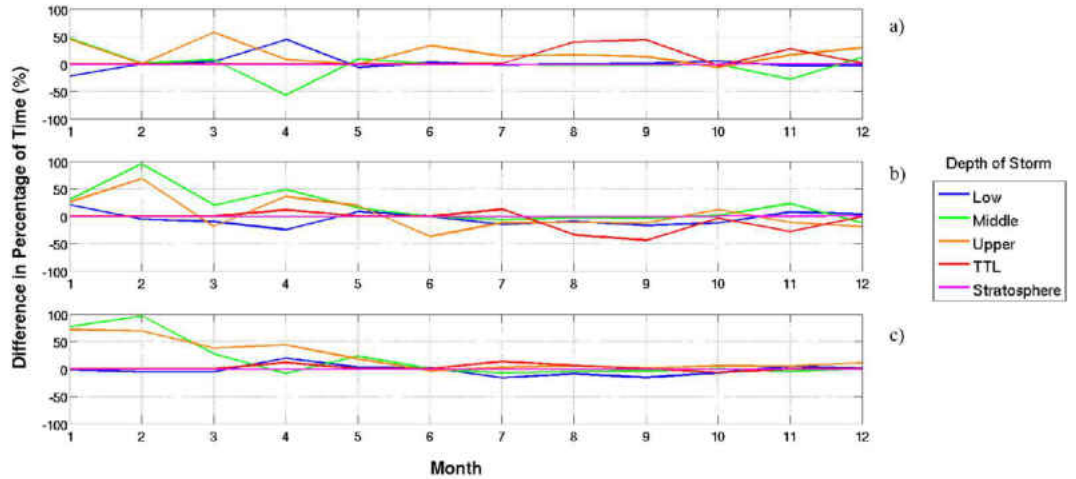


Figure 24: Difference of the percentage of time isolated storms are present in the domain from a) 2005-2010, b) 2011-2005, and c) 2011-2010.

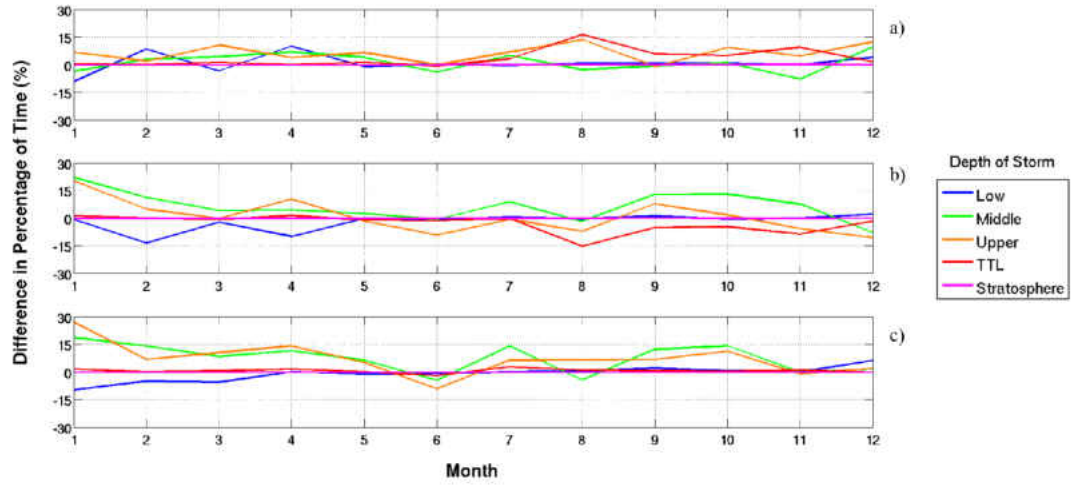


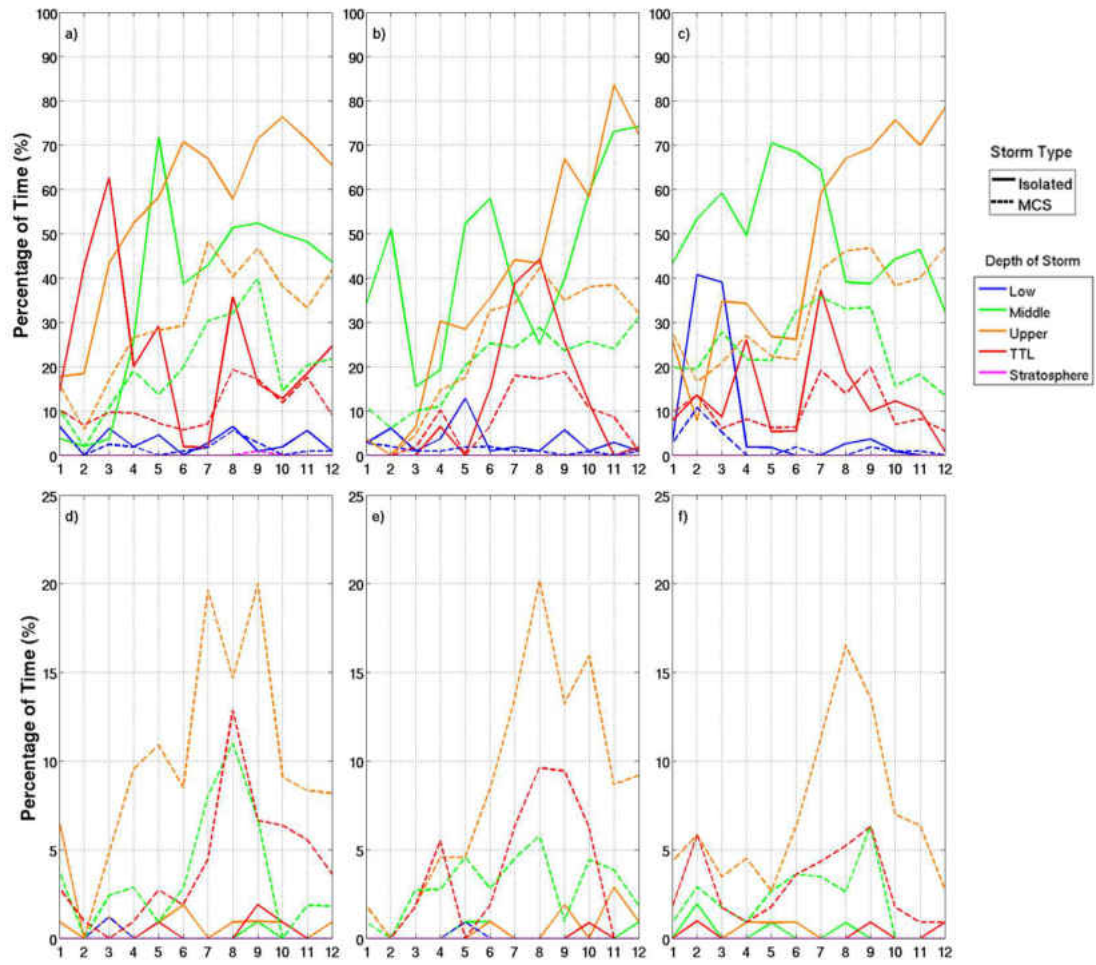
Figure 25: Difference of the percentage of time MCSs are present in the domain from a) 2005-2010, b) 2011-2005, and c) 2011-2010.

4.4 Satellite-based Radar Classification

The number of observations for the satellite-based radar classification for the years 2005, 2010, and 2011 is shown in Table 6. For the purpose of this study and the investigation of turbulence, isolated shallow will not be discussed. In addition, because tropical cyclones never progressed into the radar domain (National Climatic Data Center Storms Event Data Base 2014) during the study years, and the limited swath width of TRMM, tropical cyclones were not classified using TRMM data.

In this analysis, storms classified using the TRMM satellite precipitation radar that were located on the edge of the swath are included in the classification, in the same manner as Method 2. However, unlike the ground-based radar domain, the area covered by the satellite swath is not consistent and changes each orbital pass. When referring to the domain, this is defined to be the area covered by the TRMM swath (Fig. 11 within the large rectangular box shown in Fig. 7. An examination of the location of each TRMM swath during 2005, 2010, and 2011 indicates that 51% of all swaths passed through the latitudinal range of the ground-based radar

($\sim 12\text{-}15^\circ$ latitude), 28% of swaths passed below the latitudinal range of the ground-based radar, and the remaining 21% of TRMM swaths passed above the latitudinal range of the ground-based radar. The effects of use of an inconsistent sampling location and area on the results of the climatology are discussed in Sections 4.5 and 4.6.2. To begin, the percentage of time isolated storms are present in the large domain for all three climatology years is provided in Fig. 26. All types of isolated storms, with the exception of Stratosphere, are present in the domain throughout all three years. In general, from April to December isolated storms with Middle and Upper heights are the most common storm type present in the domain, though the maximum percentage of time is less than the percentage of time determined using the ground-based radar. Unlike the ground-based radar climatology, seasonal variation is not as apparent, especially for isolated storms with Upper and TTL heights. The most noticeable difference between the ground-based and satellite-based radar climatology is the decrease in the percentage of time isolated storms with Low heights were classified with the satellite-based data. This difference may be caused by different methods used to calculate the echo top height with each radar. More specifically, in order for TRMM to output an echo top height, the pixel must have a high confidence of rain present. Furthermore, the frequency of low convective storms may be overestimated in the ground-based radar climatology due to ground clutter or beam blockage.



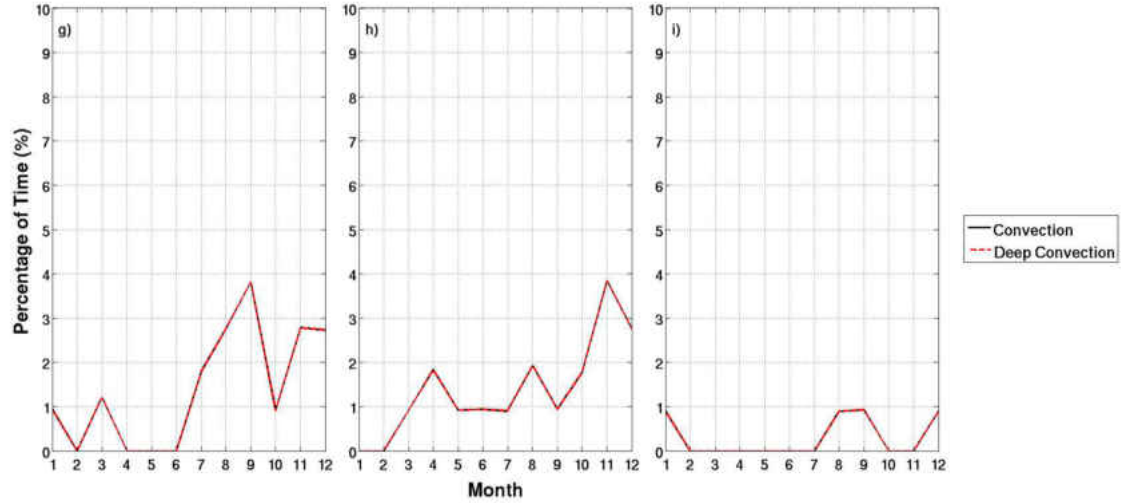


Figure 26: Percentage of time convection is present in the large domain during a) 2005, b) 2010, and c) 2011 using satellite-based radar. Percentage of time the area of convection exceeds 12.5% of the satellite swath area during d) 2005, e) 2010, and f) 2011. Percentage of time the area of deep convection (all types of isolated deep and MCSs) and only deep convection exceeds 60% of the satellite swath area during g) 2005, h) 2010, and i) 2011. Solid lines represent isolated deep storms and dashed lines represent MCSs.

The climatology of MCSs classified using TRMM data demonstrates that all MCS types were present in the domain at least once (Fig. 26). In comparison with ground-based radar climatology, the following are noted:

- the satellite-based climatology also shows that MCSs with Middle and Upper depths are generally the most common MCS storm types;
- there is a similar increase in the percentage of time MCSs with Middle, Upper, and TTL heights are present in the domain during the months of June through September;
- the percentage of time that MCSs with Middle and Upper depths are present in the domain during the months of August through October is very comparable to those percentages found using ground-based radar;

- the percentage of time that MCSs with TTL depths were present in the domain is generally greater when classified with TRMM data. This implies that the spatial limitation of the ground-based radar may influence the classification of deeper MCSs.

The results of $P_{IC > 12.5}$ demonstrates that the irregular swath size may influence this percentage of time (Fig. 26 d-f). $P_{IC > 12.5}$ reaches 3%, where in the ground-based radar classification this area threshold was never surpassed. This may indicate that when the swath area is much less than the area of the radar coverage and isolated storms are present, that the area threshold is more likely to be surpassed. On the other hand, $P_{MCS > 12.5}$ had values similar to those in the ground-based climatology (Fig. 26d-f) and was greater than $P_{IC > 12.5}$. The MCSs with Upper depths were the most common storm type to exceed the area threshold, especially during the summer months, which was also the case for the ground-based radar climatology. Furthermore, as with the ground-based radar climatology $P_{CONV > 60}$ and $P_{DCONV > 60}$ was greater than zero most often in the summer and fall, but the maximum percentages of time determined from the satellite-based climatology was less (Fig. 26g-i).

As in Section 4.3, the percentage differences between each study year are discussed in order to determine if using a different data source alters the results, and ultimately, the way aviation operations would be assessed during above- and below-average rainfall years (Figs. 27 and 28). In comparison to 2010, the percentage of isolated storms and MCSs present in the domain for the majority of 2005 was greater. This increase in percentage of time is also noted when the climatology from 2011 is compared to 2010. However, when the first portion of 2011 is compared to 2005, the percentage of time isolated storms with higher echo top heights are present in the domain is greater in 2005, while lower isolated storms are more common in 2011.

This contradicts the findings from the ground-based radar climatology, at least for the first seven months.

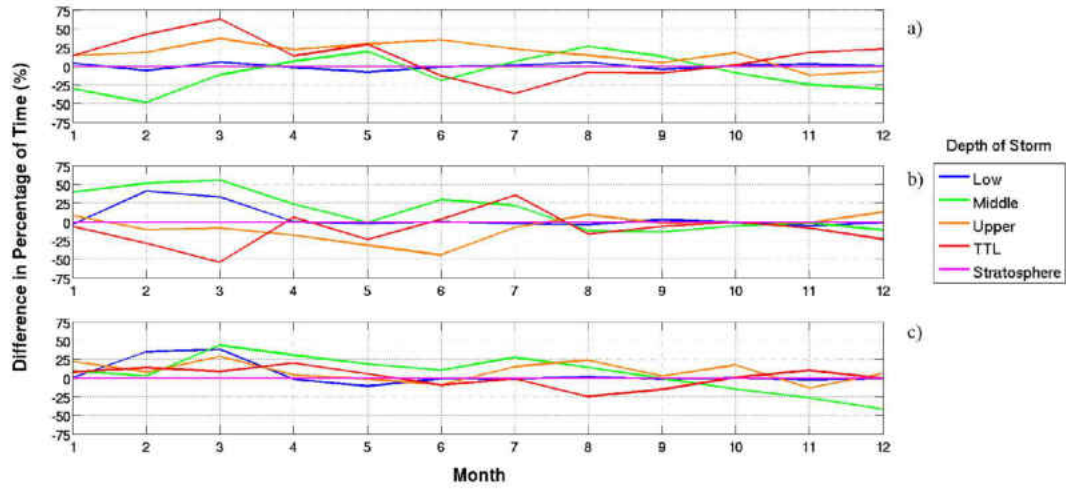


Figure 27: Difference of the percentage of time isolated storms are present in the large domain using satellite-based data. a) 2005-2010, b) 2011-2005, and c) 2011-2010.

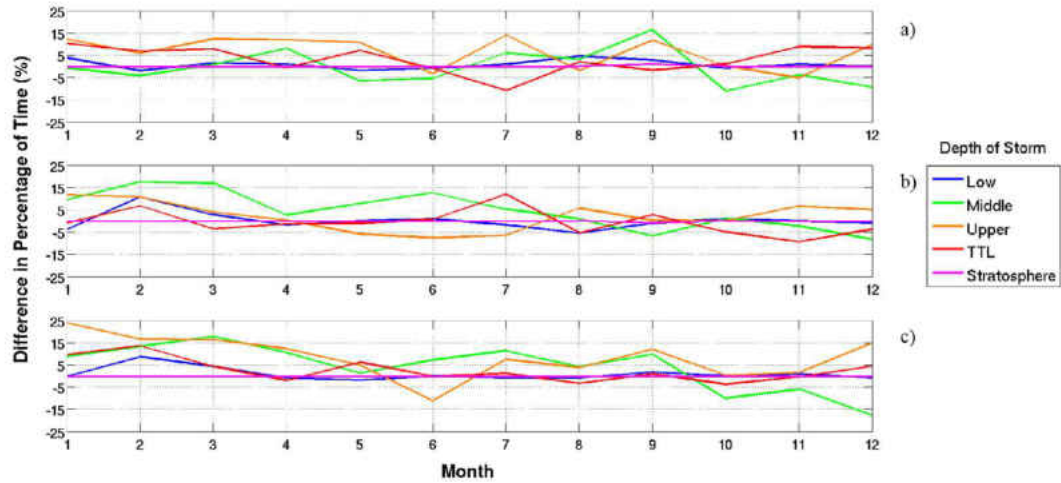


Figure 28: Difference of the percentage of time MCSs are present in the large domain using satellite-based data. a) 2005-2010, b) 2011-2005, and c) 2011-2010.

4.5 Statistical Comparison of Ground-based Radar and Satellite-based Radar Classification

A statistical comparison of the ground and satellite-based radar classifications is necessary because in an operational setting, multiple data sources would be available and an understanding of the limitations with each is important. As done previously, two-tailed proportion tests with 95% confidence are used to statistically compare the results of the ground-based radar and satellite-based radar classifications (Fig. 29). The p-values from this analysis are provided in Tables 19 and 20. First, there is a significant statistical difference between the percentage of time convection is present in the small radar and large domain for all of the study years, with the exception of convection with Stratosphere depths. There are four reasons that significant statistical differences are found between the ground-based and satellite-based climatologies. These reasons are the sampling of different storm populations, the convolution radius utilized in the methodology, the convective threshold of 40 dBZ, and the influence of beam blockage and the "cone of silence". Analysis indicated that the satellite-based radar sampled storms outside of the latitudinal range of the ground-based radar almost 50% of the time. An example of the ground-based and satellite-based radars sampling different storm populations at approximately the same time is provided in Fig. 30. In this example the satellite-based radar classified a majority of MCSs while the ground-based radar classified only isolated storms. In addition, because TRMM is capable of sampling a large latitudinal range, storms associated with the progression of the Intertropical Convergence Zone (ITCZ) can be sampled more frequently.

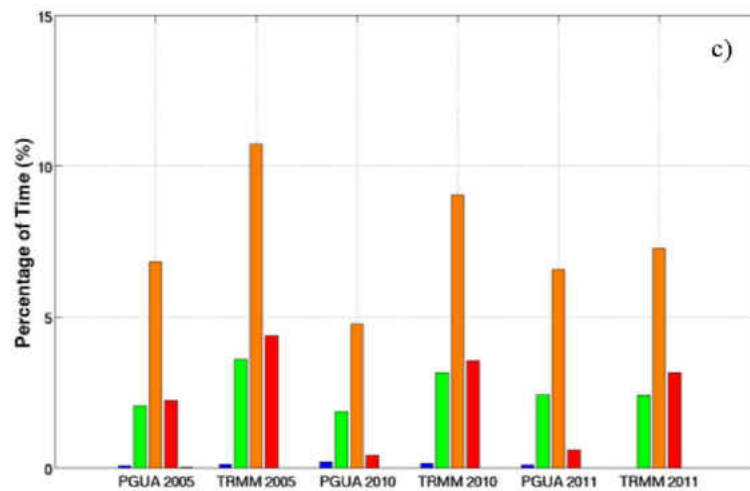
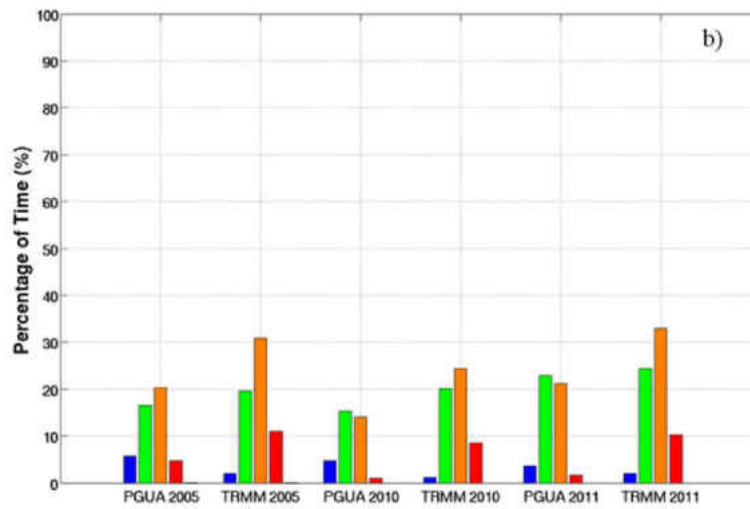
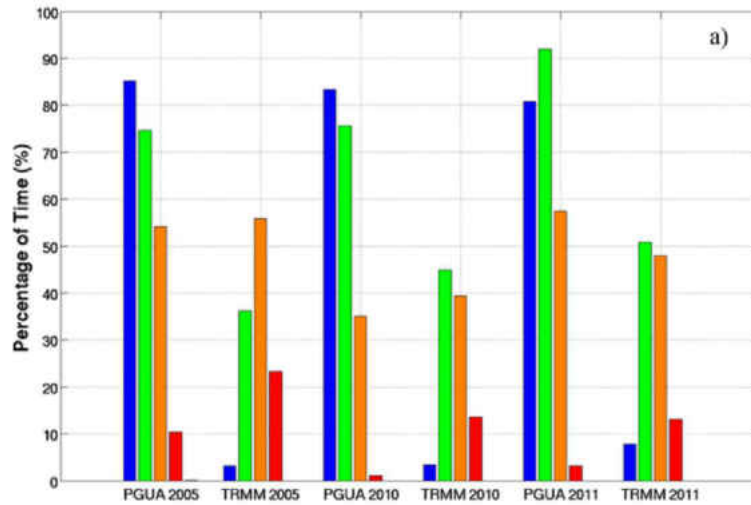
The second cause for the significant statistical differences in the percentage of time storms were present in the domain is the convolution radius implemented in the Method for Object-Based Diagnostic Evaluation (MODE). Due to the coarser horizontal resolution of TRMM precipitation data storms were not identified as objects

in MODE. This was especially the case for the climatology of Isolated Low storms. When the convolution radius was decreased to 4 km for satellite-based radar data for August 2005, the percentage of time Isolated Low storms were present in the domain increased. Figure 31 represents objects identified using MODE using the original and decreased convolution radius. Overall, when the convolution radius decreased, significant statistical differences were still found in the percentage of time storms were present in the domain.

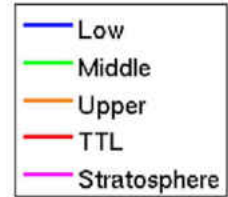
The third reason significant statistical differences were found in the percentage of time storms were present in the domain is also related to the horizontal resolution of the satellite-based radar data. Because the satellite-based radar data has a coarse resolution, finer reflectivity details that are shown in ground-based radar data are smoothed out in the satellite-based radar data. An additional investigation was performed to determine how the convective threshold of 40 dBZ influences the classification of storm types from satellite-based radar. Decreasing the convective threshold from 40 dBZ to 35 dBZ for August 2005 for the satellite-based radar data, increased the percentage of time Isolated Low storms were present in the domain to nearly 70%. An increase in percentage of time also occurs for the remaining storm types. These percentages of time are also more comparable to the results of the ground-based radar climatology when the convective threshold is decreased to 35 dBZ for the satellite-based climatology.

The final explanation for the significant statistical differences in the percentage of time storms were present in the domain is caused by beam blockage and the "cone of silence" in the ground-based radar data. Beam blockage frequently caused objects that were originally one storm to be divided into two regions which would then influence the classification increasing the percentage of time that Isolated Low storms were present in the domain. Finally, storms within the cone of silence (the

region directly above the radar) causes the distribution of storms to shift between deeper to lower storms.



Depth of Storm



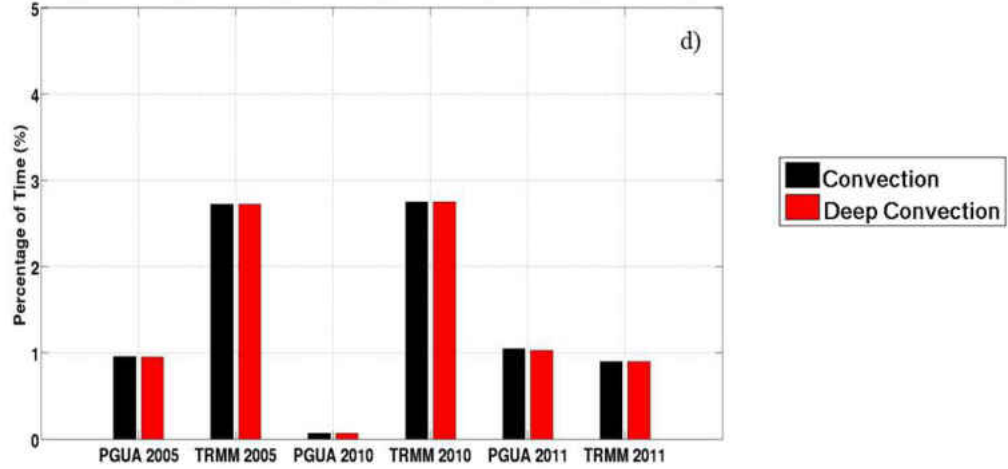


Figure 29: Percentage of time a) isolated storms and b) MCSs are present in the small radar domain from the ground-based radar climatology and the large domain from the satellite-based radar climatology. The percentage of time the area of convection exceeds 12.5% of the small radar domain from the ground-based radar climatology and the large domain from the satellite-based radar climatology is represented in c). The percentage of time the area of all types of convective storms and only deep convective storms exceeds more than 60% of the small radar domain from the ground-based radar climatology and the large domain from the satellite-based radar climatology is represented in d).

Table 19: p-values calculated from a proportion test with 95% confidence for the percentage of time convective storms are present in the small radar domain from the ground-based radar climatology and the large domain from the satellite-based radar climatology.

	Year	Low	Middle	Upper	TTL	Stratosphere
p-value	2005	<1E-1000	6.45E-360	4.77E-23	1.89E-75	0.5053
p-value	2010	<1E-1000	4.88E-198	3.79E-25	4.77E-371	N/A
p-value	2011	1.46E-994	<1E-1000	0.0411	1.97E-182	N/A

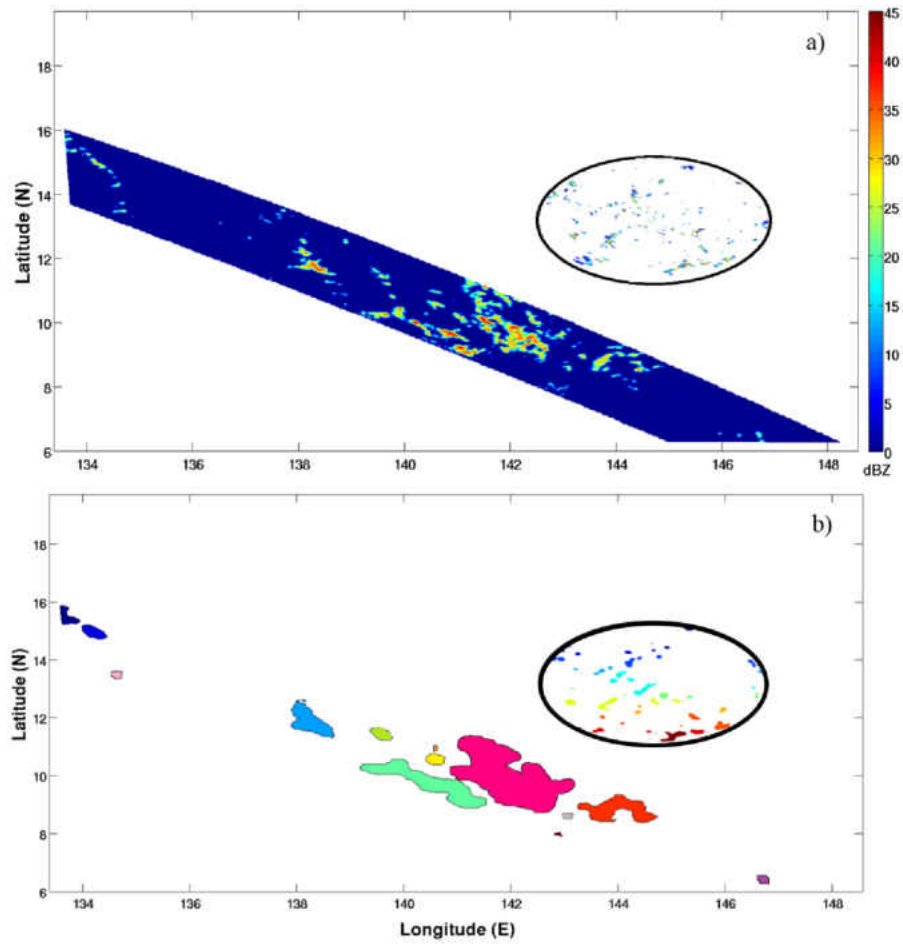


Figure 30: a) An example of reflectivity (dBZ) from TRMM 2A25 and PGUA radar on 10 August 2005 at 21 UTC and b) objects identified by the Method for Object-Based Diagnostic Evaluation at 21 UTC on 10 August 2005.

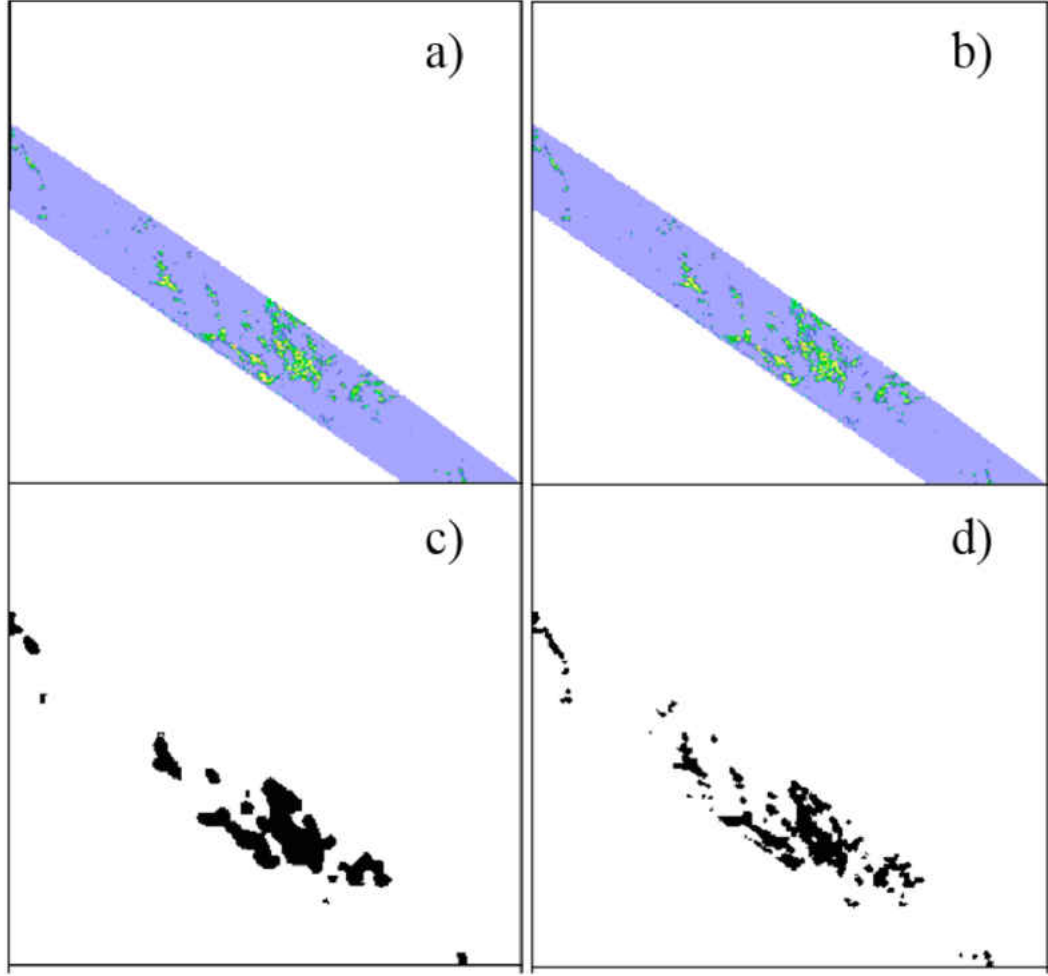


Figure 31: a-b) Reflectivity determined from TRMM on 10 August at 21 UTC. Objects identified by the Method for Object-Based Diagnostic Evaluation using a convolution radius of c) 8 km and d) 4 km.

In comparison, the $P_{CT > 12.5}$ calculated from both original classifications demonstrates that there is not always a significant difference between the climatologies. To elaborate, in 2005 and 2010 there is not a significant statistical difference in the percentage of time the area of convection with Low and Stratosphere depths exceeds 12.5% of the domain area. In addition, there is not a significant statistical difference between the classifications during 2011 for convection with Middle, Upper, and Stratosphere depths. Furthermore, there are no significant differences of $P_{CONV > 60}$

and $P_{\text{DCONV} > 60}$ between the ground and satellite-based climatologies during 2011 (Table 21).

Table 20: p-values calculated from a proportion test with 95% confidence for the percentage of time the area of convective storms more than 12.5% of the small radar domain from the ground-based radar climatology and the large domain from the satellite-based radar climatology.

	Year	Low	Middle	Upper	TTL	Stratosphere
p-value	2005	0.6949	0.0002	8.86E-8	3.43E-7	0.6145
p-value	2010	0.8643	0.0007	9.27E-14	1.23E-47	N/A
p-value	2011	0.0006	0.9816	0.334	1.52E-27	N/A

Table 21: p-value calculated from a proportion test with 95% confidence for the percentage of time the area of all types of convective storms and only deep convective storms exceeds more than 60% of the small radar domain from the ground-based radar climatology and the large domain from the satellite-based radar climatology.

	Year	p-value
Convection	2005	5.79E-10
Deep Convection	2005	5.07E-10
Convection	2010	2.31E-108
Deep Convection	2010	2.31E-108
Convection	2011	0.665
Deep Convection	2011	0.7189

4.6 Discussion of Observational Results

4.6.1 Seasonal Variability

As was discussed in the previous result sections, seasonal trends for several storm types are apparent, in the PGUA and TRMM classifications, in both the percentage of time storms are present and in the domain percentage that is covered. Figure 32 shows the average $P_{\text{CT} > 12.5}$ for all three study years. It is clear that from

June to October the percentage of time increases substantially for convection with Middle, Upper, and TTL depths.

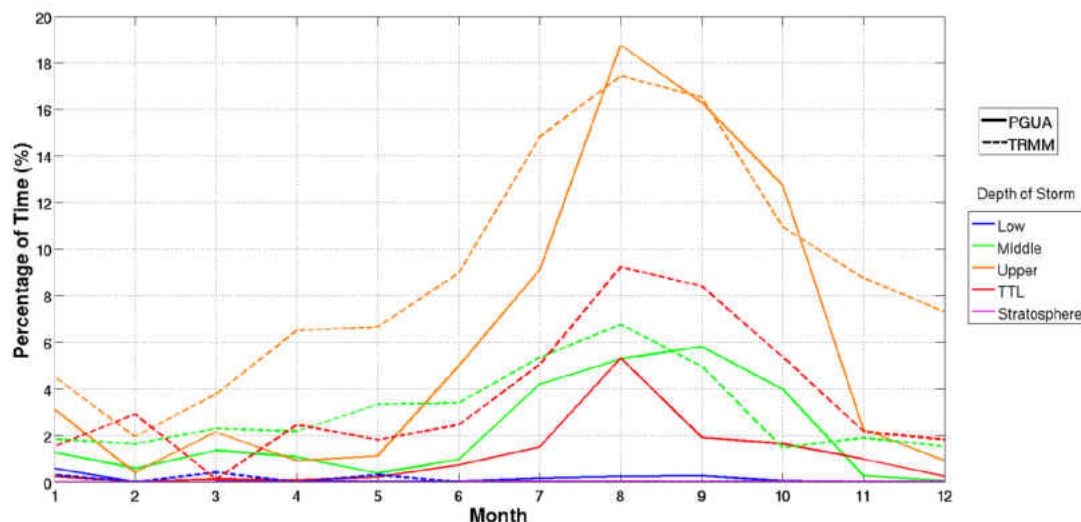


Figure 32: Percentage of time the area of convection covers more than 12.5% of the domain. Solid lines represent the percentage of time calculated from PGUA in the radar domain, and dashed lines represent the percentage of time calculated from TRMM in the large domain.

It is important to assess the results of this storm type climatology in relationship to past convection related climatologies in tropical regions. Kodama et al. (2009) created a climatology of precipitation types using a nine year average from 1998-2006 using TRMM precipitation radar (PR) data in order to identify seasonal trends (Fig. 33). Their study included the region encompassed by the large domain in this current study. Kodama et al. (2009) showed that in the majority of the large domain in January, convective rainfall accounts for more than 2 mm day^{-1} and stratiform rainfall accounts for less than 2.5 mm day^{-1} . Alternatively, during the month of July, convective rainfall in the large domain accounts for more than 3 mm day^{-1} and stratiform rainfall accounts for more than 4 mm day^{-1} . This increase in precipitation during summer months can be attributed to the northward progression of the ITCZ

and increasing sea surface temperatures (SST), upon which deep convection in the tropics has been found to be dependent (Zhang 1993, Lau et al. 1997). Though this study does not consider amounts of specific types of rainfall, the increased frequency of convection during summer months are consistent with the climatology created by Kodama et al. (2009). In addition, Biasutti et al. (2012) studied climatological patterns of rain frequency, defined as the percentage of observations at a given location during which rain was detected using TRMM PR near surface reflectivity, and rainfall intensity from 1998 to 2007. In the area of interest for the current study, they determined that rainfall is frequent in the Maritime Continent throughout the year, and has a less pronounced dry season, which is evident in the current study as isolated storms with lower echo top depths are present more than 60% year round (Figs. 24 and 27). Furthermore, Biasutti et al. (2012) found that there is a noticeable increase in rainfall frequency during the summer months (Fig. 34), which is consistent with the increased presence of deeper convection identified in this study.

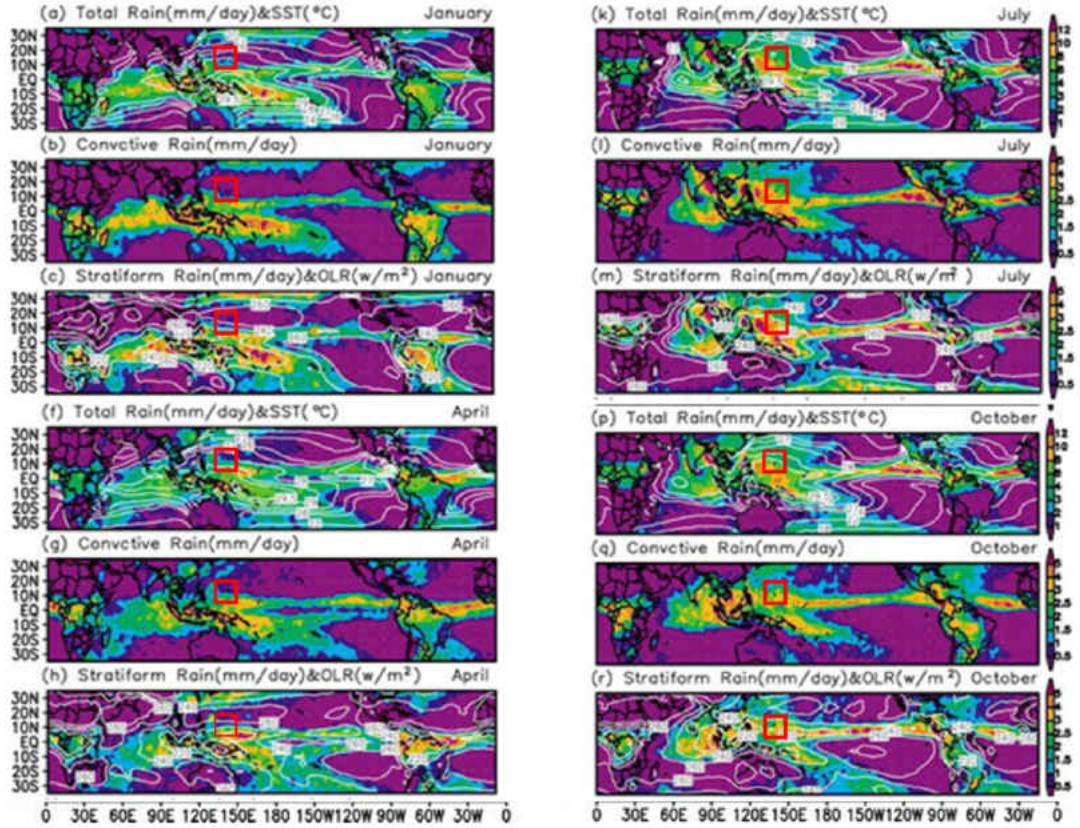


Figure 33: Near surface rain categorized by rain type for January, April, July, and October from 1988-2006 in mm day^{-1} analyzed from TRMM precipitation radar data (shaded; Aparted from Kodama et al. 2009, Figure 1). The area in the red box represents the large domain.

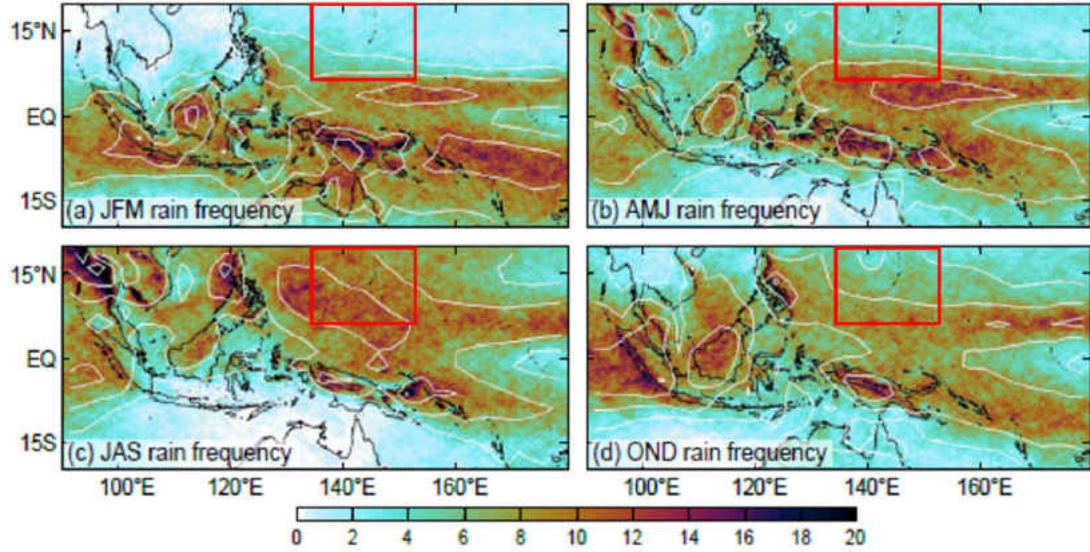


Figure 34: Seasonal mean rain frequency in the TRMM precipitation data (shaded; Biasutti et al. 2012, Figure 12). The area in the red box represents the large domain.

Another important factor that could influence the percentage of storms present in both of the domains used in this study is the El-Niño Southern Oscillation (ENSO). As was previously stated, Zhang (1993) and Lau et al. (1997) found that the formation of deep convection is dependent on SST. El-Niño is defined as a significant increase in sea surface temperature over the eastern and central equatorial Pacific (Glickman 2000). Furthermore, El-Niño occurs at irregular intervals, generally ranging between two and seven years. Simplistically, an El-Niño produces lower SSTs in the western Pacific, which could hinder the formation of deep convection. On the other hand, a La-Niña produces higher SSTs in the western Pacific, favoring the formation of deep convection. The Climate Prediction Center (CPC; Climate Prediction Center ENSO Diagnostic Discussion 2005) recorded a weak El-Niño environment during the beginning of 2005 and then a weak La-Niña towards the end of the year (Table 22). In 2010, a moderate El-Niño was present in the first three months, then a more neutral environment occurred until the summer months when a strong La-Niña was present

(Climate Prediction Center ENSO Diagnostic Discussion 2010). Lastly, during 2011, a strong La-Niña was present in the first few months but decreased to a weak La-Niña throughout the year (Climate Prediction Center ENSO Diagnostic Discussion 2011). As previously mentioned, seasonal trends are apparent in the percentage of time both isolated and MCSs were in the domains. However, the percentage of time varies considerably for each year, raising the question if El-Niño patterns did influence the results. A qualitative analysis for only isolated storms in the small radar domain during 2010 shows that during the month of January when a moderate El-Niño was observed, the percentage of time isolated storms with Middle and Upper depths were present is different from 2005 and 2011, which is also the case for isolated storms with Upper depths in the months of March and April (Fig. 24). However, when a La-Niña was observed during 2010, only the percentage of time isolated storms with Middle depths are in the domain is actually greater than the same storm type in 2005 and 2010 (Fig. 24). Therefore, El-Nio and La-Niña can influence the percentage of time storm types are present in the domain. Nonetheless, more analysis of SST and climatic oscillations is needed to verify this preliminary finding.

4.6.2 Limitations of the Climatology

The results of this study are limited by several factors. First and foremost, the results are exclusively from three separate years. In general for climatologies, a large number of years is preferred to reduce the impact of extreme values in the data. In addition, the influence of climatic patterns, such as ENSO may significantly affect the results with limited years. Secondly, the use of Level 3 ground-based radar data introduces quality control (QC) that was performed by an outside source for which detailed documentation is not available. QC includes the removal of non-meteorological objects such as buildings and birds, and corrections due to the attenuation of the radar

Table 22: Oceanic Niño Index (3 month running mean of SST anomalies for 5 °N-5 °S, 120-170 °W; Climate Prediction Center 2015).

Year	DJF	JFM	FMA	MAM	AMJ	MJJ	JJA	JAS	ASO	SON	OND	NDJ
2005	0.6	0.4	0.3	0.3	0.3	0.3	0.2	0.1	0.0	-0.2	-0.5	-0.8
2010	1.6	1.3	1.0	0.6	0.1	-0.4	-0.9	-1.2	-1.4	-1.5	-1.5	-1.5
2011	-1.4	-1.2	-0.9	-0.6	-0.3	-0.2	-0.2	-0.4	-0.6	-0.8	-1.0	-1.0

beam by hydrometeors. Furthermore, several radar scans suffered beam blockage that created two separate objects in MODE that were in reality one object. These objects were then classified as individual storms. Another limitation with Level 3 radar data is that reflectivity values were output in 5 dBZ increments, without documentation on what dictates what rounding method is used. This could influence the amount of storms classified as convective if the true reflectivity values were less than 40 dBZ. Thirdly, the use of base reflectivity with an elevation angle of 0.5° may influence the storm type classification when it is farther from the radar site. More specifically, at the farthest distance the radar beam is near the freezing level, which is highly reflective. Additionally, the cone of silence causes the radar to miss storms directly over the radar site. Lastly and most importantly, the inconsistency in TRMM swath area could influence the convective coverage percentages. An additional investigation was performed for 2005 to determine how often the area of the satellite swath was greater or significantly less than the areal coverage of the ground-based radar (Table 23). Each month, over 55% of the satellite-based radar observations had a swath area greater than the ground-based radar area. Furthermore, less than 11% of satellite-based radar observations each month had a swath area less than 6% of the area of the small radar domain. This indicates that the percentage of time the area of storms exceeded 12.5% of the domain area was less influenced by the scans with very small areas.

Table 23: The number of satellite-based radar swaths per month in the large domain along with the percentage of observations whose areas were greater or less than the ground-based radar area domain (GBR; $1.66 \times 10^2 \text{ km}^2$) during 2005.

Month	Number of Observations (Obs.)	Average Area ($\times 10^5 \text{ km}^2$)	Percentage of Obs. > GBR	Percentage of Obs. < GBR	Percentage of Obs. < 10^4 km^2
January	107	2.73	62.6	37.4	4.7
February	103	2.22	56.3	43.7	13.6
March	83	2.69	72.3	27.7	7.2
April	105	2.33	63.8	36.2	5.2
May	110	2.28	60.9	39.1	9.1
June	106	2.33	59.4	40.6	8.5
July	112	2.29	60.7	40.3	9.8
August	109	2.35	63.3	36.7	4.6
September	105	2.26	60	40	10.5
October	110	2.3	59.1	40.9	7.3
November	108	2.31	60.2	40.8	9.3
December	110	2.30	61.8	38.2	8.2

4.6.3 Influences of Climatology Results on Aviation Operations

The results of the storm type climatologies indicate that aviation operations would be influenced the most during the summer months. During this time isolated and MCSs with higher echo top heights and larger areal coverage are present more frequently which would impact flight routes, takeoff and landing procedures, and delay or cancel flights. In regards to vertical separation requirements used by NASA's Global Hawk and previous FAA avoidance policies to avoid convective hazards, the flight height would need to increase in order to remain a safe distance above significant convective tops during the summer months. Furthermore, during years when greater precipitation amounts are predicted in association with climatic oscillations aviation operations could be altered.

4.6.4 Storm Type Hazard Risk

It has been determined that isolated storms are present in both the small radar and large domains more frequently than MCSs (Figs. 23 and 26). However the area of MCSs more commonly cover more than 12.5% of the domains. Still, isolated storms with deeper depths have the potential to create turbulent regions more frequently than MCSs because these storms are more frequently in the domains.

CHAPTER 5

RESULTS AND DISCUSSION: MODEL INVESTIGATION OF CONVECTIVELY-INDUCED TURBULENCE

5.1 Case Day Selection

A 48 hour period beginning on 5 August 2005 was used to simulate tropical convection near Guam using WRF. This period was chosen by determining the consecutive 48 hour period from the three year climatology study (see Chapter 4) that had the highest percentage of time both isolated deep storms and MCSs were present in the domain. This 48 hour period represents a worst case scenario of convection. Simulating a period in which convection was present the majority of the time is done in order to ensure gravity wave signatures and to gain a sense of how intense turbulence could be during an active period. The average number of objects present in each radar scan during the 48 hr period was 24. During the full 48 hr period, isolated deep storms with Low, Middle, Upper, and TTL (tropopause transition layer) depths are in the radar domain more than 87% of the time. MCS Middle, Upper, and TTL depths are present in the radar domain more than 15% of the time. Breaking the time period into 24 hr segments, on 5 August shallow stratiform regions accounted for 39% of the objects classified, Isolated Deep storms with Low heights accounted for more than 25% of the objects, and MCSs accounted for less than 1% of storms (Fig. 35a). However, on 6 August the total percentage of MCSs classified increases to more than 5%, the majority being MCSs with Upper and TTL depths (Fig. 35b).

The majority of objects classified as Isolated Deep in the second half of the 48 hr period had Upper echo top heights.

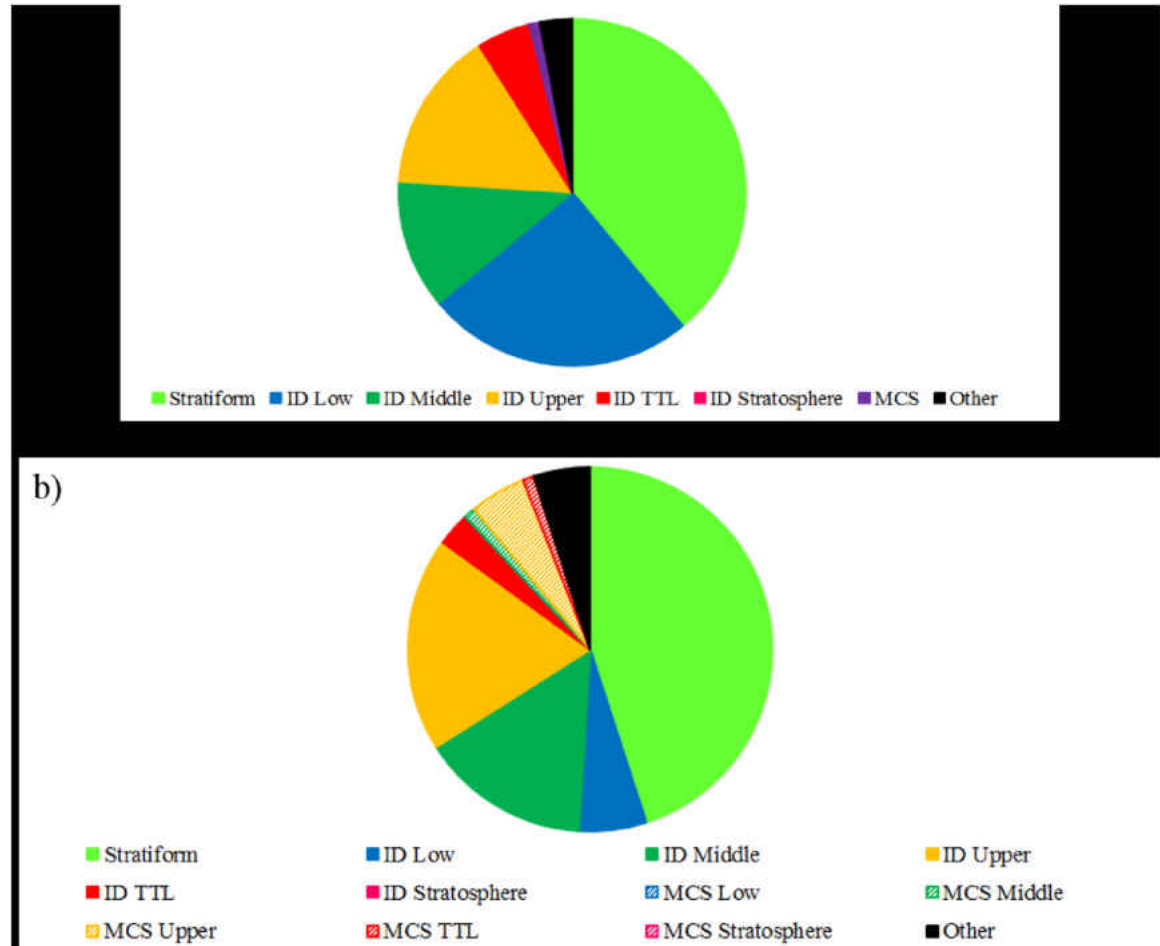


Figure 35: Percentage of echo storm type present in the domain on a) 5 August 2005, and b) 6 August 2005, as determined from the climatology.

5.2 Overview of Observed and Simulated Synoptic and Mesoscale Features

5.2.1 5 August 2005

From the analysis of radiosondes launched from Guam International Airport at 00 UTC and 12 UTC on 5 August (Fig. 36) the equilibrium level was near 128 hPa and 120 hPa, respectfully (University of Wyoming 2015). The freezing level at

00 UTC and 12 UTC was near 550 hPa, approximately 5.2 km in height mean sea level (MSL). Furthermore, convective available potential energy (CAPE) at 00 UTC and 12 UTC was 1713 J kg^{-1} and 1983 J kg^{-1} . In comparison to 00 UTC, at 12 UTC a drier environment was present from 800 hPa to 400 hPa.

WRF simulated soundings on 5 August at 00 UTC and 12 UTC (Fig. 36) indicate that the equilibrium level was near 125 hPa and 120 hPa, respectfully. The freezing level was near 560 hPa (5 km in height) at 00 UTC and 540 hPa (5.3 km in height MSL) at 12 UTC. In addition, CAPE during 00 UTC and 12 UTC was 1953 J kg^{-1} and 1913 J kg^{-1} . In comparison to the 00 UTC simulated sounding, the 12 UTC sounding has a drier environment, similar to that of the observed 12 UTC sounding. Overall, the observed and simulated atmospheric parameters are very similar indicating the model simulation was initialized well.

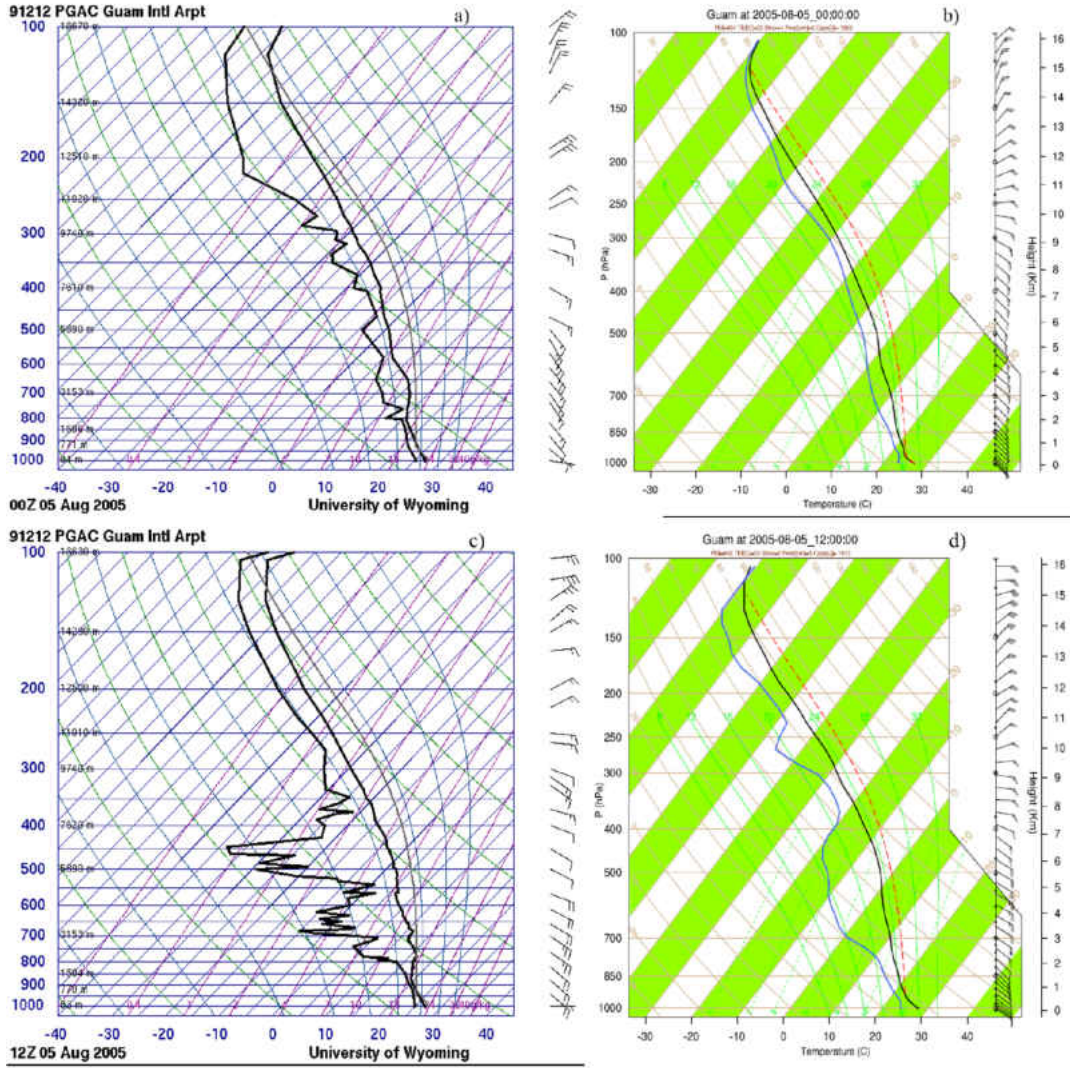


Figure 36: Observed and model simulated soundings at a-b) 00 UTC and c-d) 12 UTC on 5 August 2005.

Mean sea level pressure reanalysis from 00 UTC on 5 August for the South Pacific region (Fig. 37a) indicates an area of low pressure south of Guam near New Guinea (Australian Government Bureau of Meteorology 2015). In addition, Typhoon Matsa was located at approximately 25 °N, 124 °E (CIMSS 2015). Furthermore, satellite-derived regions of low level convergence (850-925 mb) were present between 10-14 °N, 143-148 °E (Fig. 37b; CIMSS 2015). Likewise, regions of upper level

divergence (150-300 mb) were present between 12-20 °N, 144-150 °E (Fig. 37c; CIMSS 2015). In regards to deep layer shear, regions extended from the northwest to the northeast and southeast of Guam (Fig. 37d; CIMSS 2015). It is also important to note the location of the Intertropical Convergence Zone (ITCZ) during this month. According to a 17 year satellite climatology of highly reflective clouds created by Waliser and Gautier (1993), the ITCZ in the West Pacific is located near 13 °N in August. Moreover, between 10-17 °N, more than seven highly reflective cloud days occur within the month.

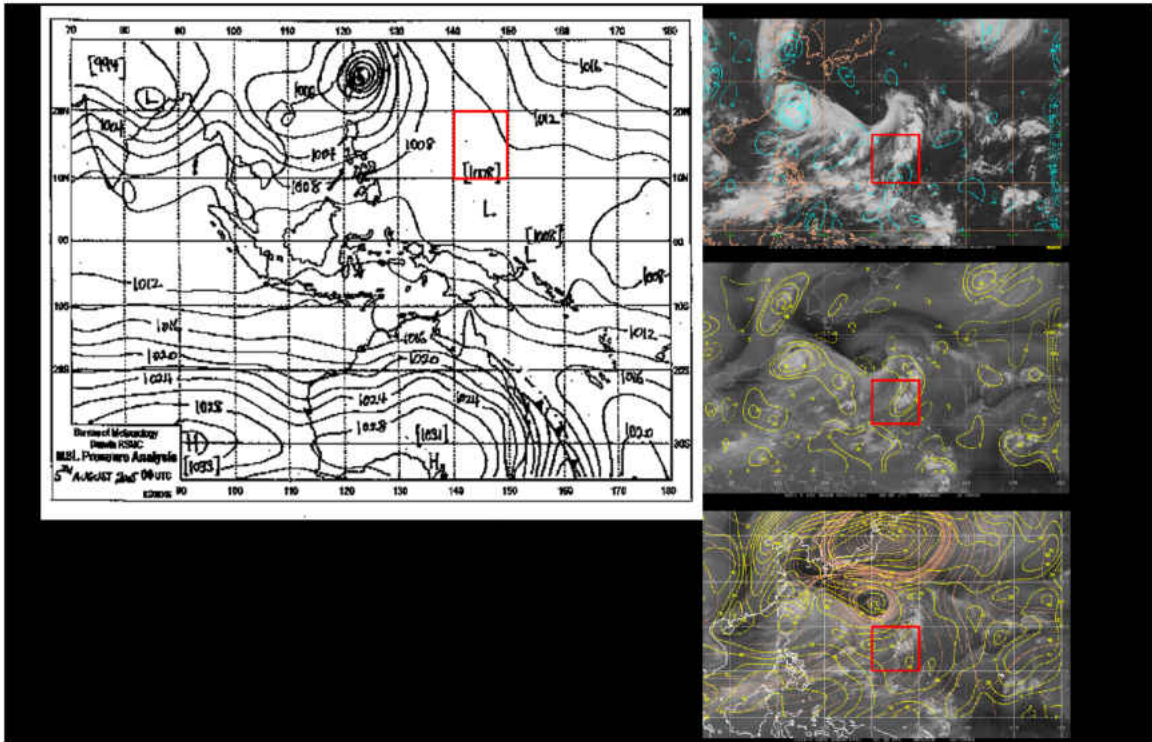


Figure 37: a) Mean sea level pressure reanalysis, b) low level convergence, c) upper level divergence, d) deep layer shear at 00 UTC on 5 August 2005.

Base reflectivity radar observations from Guam during the first 12 hours of 5 August show isolated cells to the east and south of Guam with reflectivities greater than 45 dBZ. However, as these isolated cells propagate to the northwest, the vast majority dissipate. With time the cells increase in areal size, especially to the south

of Guam. By 19 UTC, the number of isolated cells present in the radar domain has decreased, but isolated cells continue to be present in the domain through 23 UTC. Climatological observations collected at Guam International Airport on 5 August indicated 0.15 inches of precipitation over the 24 hour period.

Simulated convection from 00 UTC to 12 UTC on 5 August was of similar intensity to storms observed with the radar, as 1 km reflectivity was between 45 dBZ and 50 dBZ. Numerous cells were present in the model domain, although the location of the majority of these storms were to the north and northwest of Guam and outside the radar domain. Furthermore, these cells were collocated with one another and a part of a larger complex of cells. With time the number of cells and intensity decreased, especially to the north of Guam. By 19 UTC, simulated storms within the radar domain are mostly absent, and stronger convective features are present to the south and northeast of Guam. In contrast to the observations collected with the radar, the size and longevity of simulated storms was greater. However, the intensity of simulated convection was similar to that observed.

5.2.2 6 August 2005

From analysis of radiosondes launched from Guam International Airport at 00 UTC and 12 UTC on 6 August the equilibrium level was near 117 hPa and 125 hPa, respectfully (Fig. 38). The freezing level at 00 UTC and 12 UTC once again was located at 550 hPa, approximately 5.2 km in height MSL. CAPE at 00 UTC and 12 UTC was 1961 J kg^{-1} and 1583 J kg^{-1} . In comparison to 12 UTC, at 00 UTC a drier environment was present from 900 hPa to 300 hPa.

Simulated soundings on 6 August at 00 UTC and 12 UTC indicate that the equilibrium level was near 125 hPa (Fig. 38). The freezing level at 00 UTC and 12 UTC was located at 570 hPa, approximately 5 km in height MSL. In addition, CAPE

at 00 UTC and 12 UTC was greater than observed CAPE, approximately 2262 J kg^{-1} and 2822 J kg^{-1} . This increase in CAPE can influence the the strength and longevity of the simulated storms. In comparison to the 12 UTC simulated sounding, the 00 UTC simulated sounding has a drier environment, similar to that of the observed 00 UTC sounding.

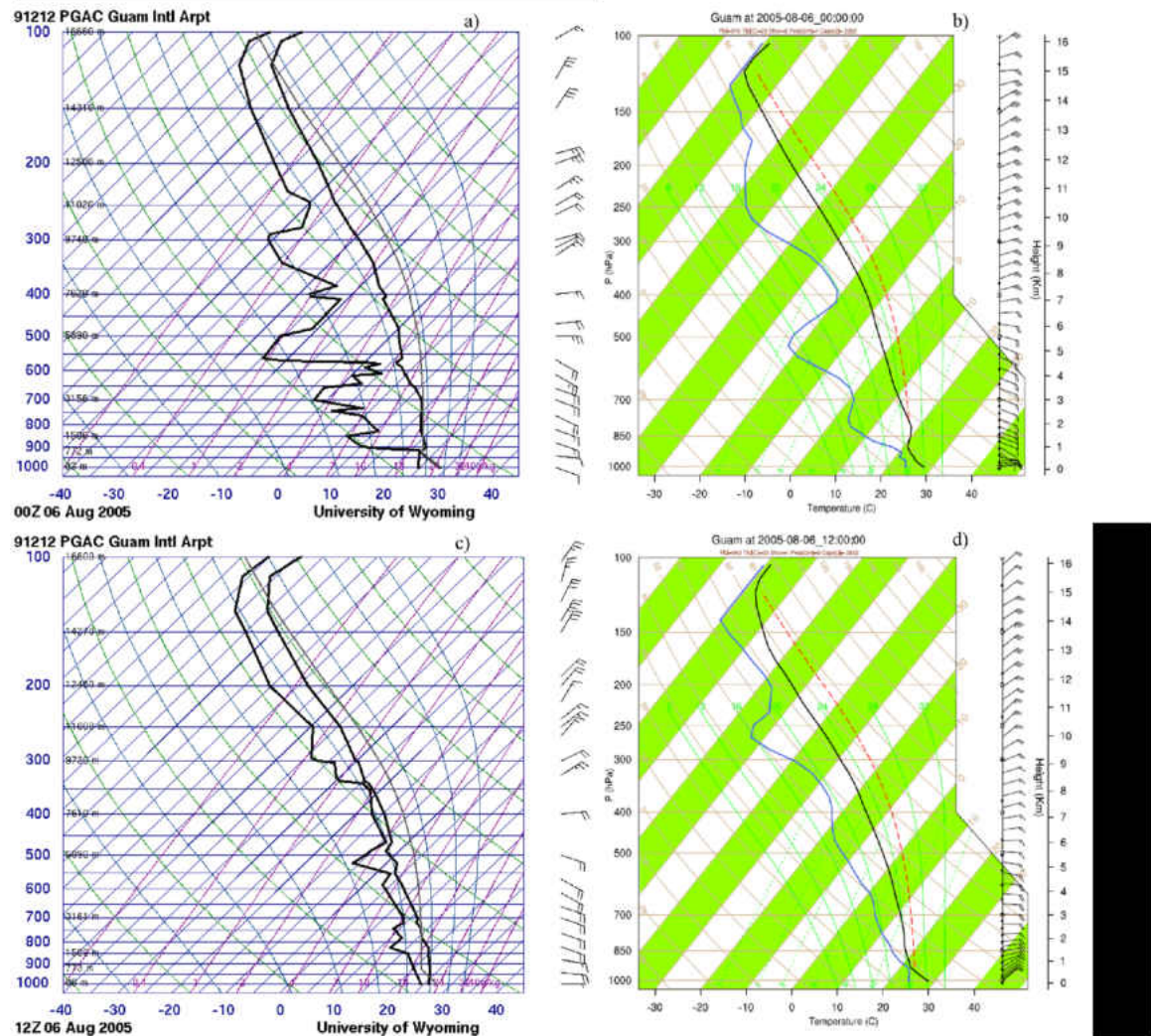


Figure 38: Observed and model simulated soundings at a-b) 00 UTC and c-d) 12 UTC on 6 August 2005.

At 00 UTC on 6 August an area of low pressure centered around 10°N , 150°E is present at mean sea level (Fig. 39a; Australian Government Bureau of Meteorology

2015). During this time the center of Typhoon Matsa had passed over 28 °N, 122 °E (CIMSS 2015). Low level convergence at this time is limited to a small region near 18 °N, 143 °E, and a region of low level divergence is present to the southwest of Guam (Fig. 39b; CIMSS 2015). At 00 UTC there is also a large region of upper level convergence to the west-southwest of Guam (Fig. 39c; CIMSS 2015). In regards to deep layer shear, between 10-20 °N, 140-150 °E a moderate shear environment is present (Fig. 39d; CIMSS 2015).

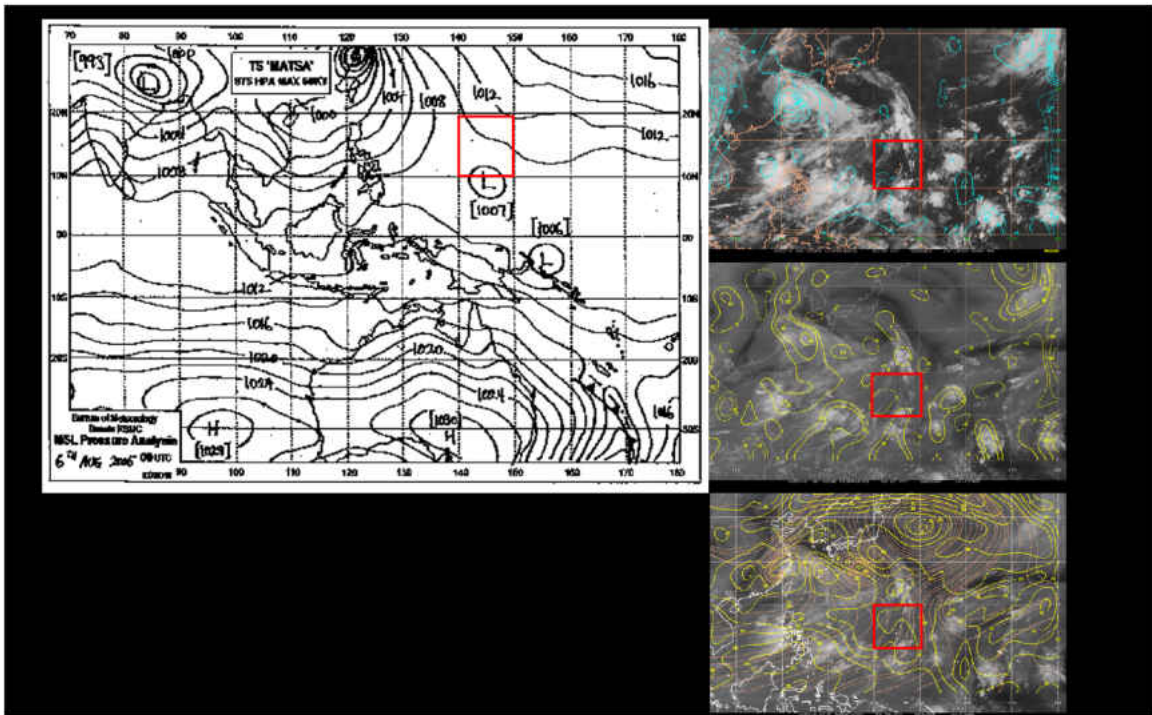


Figure 39: a) Mean sea level pressure reanalysis, b) low level convergence, c) upper level divergence, d) deep layer shear at 00 UTC on 6 August 2005.

Base reflectivity radar observations collected from Guam on 6 August shows larger, more intense convective features within the radar domain slowly propagating from the east to due west. By 11 UTC almost no convection was present in the southern portion of the radar domain as the majority was present as large regions of weaker convection to the north of Guam. By 15 UTC more isolated storms are

once again present in the southern portion of the radar domain, with reflectivity at 1 km greater than 40 dBZ. The number of isolated cells in the entire radar domain continues to increase throughout the remaining nine hours of 6 August. According to climatological records, Guam received 0.48 inches of precipitation on 6 August (NCDC 2015).

Simulated convection from 00 UTC to 12 UTC on 6 August indicated that storms with areal coverage less than 1% of the domain area were present to the east and north northeast of Guam. To the south of Guam stronger larger convective features were present. Convection continued to propagate from the east to the southwest and from the south to the northwest. By 14 UTC, more isolated cells are simulated to the north of Guam and propagate into the radar domain. The intensity of these cells increases as they move south. In comparison to the radar observations, the areal coverage and lifespan of simulated convection was more similar on 6 August than on 5 August. In addition, the direction of propagation of simulated storms was more similar to radar observed propagation on this day as well.

In the following section results from the first 24 hours of the 48 hour modeling study, which are divided into 6 hour periods, are discussed. Turbulence is analyzed at altitudes of 10, 14, 18, and 20 km, in order to be applicable to high altitude aviation operations. These heights represent a region below the TTL, within the TTL, at the tropopause, and within the stratosphere.

5.3 Simulation of Convection and Estimation of Turbulence Results

Convection simulated during the first six hours of the simulation period can be divided into five convective features by examining echo top heights (Fig. 40). Feature 1 is an individual cell with a maximum echo top height of 15 km. Feature 2 is a large complex of cells that have echo top heights greater than 14 km. During the first six

hours of the simulation, features 3-5 are visually represented by large regions of echo top heights less than 8 km. In regards to turbulence intensity, at 06 UTC Moderate-Severe (MS) turbulence is located in the same regions as the convective features, especially at 10 and 14 km (Fig. 41). The maximum percentage of the domain experiencing MS of turbulence is near 17% at 14 km, which is also the maximum percentage for all types of turbulence at any height. An additional feature of note is that the intensity of turbulence and the percentage of the domain experiencing turbulence generally decrease with height (Fig. 42).

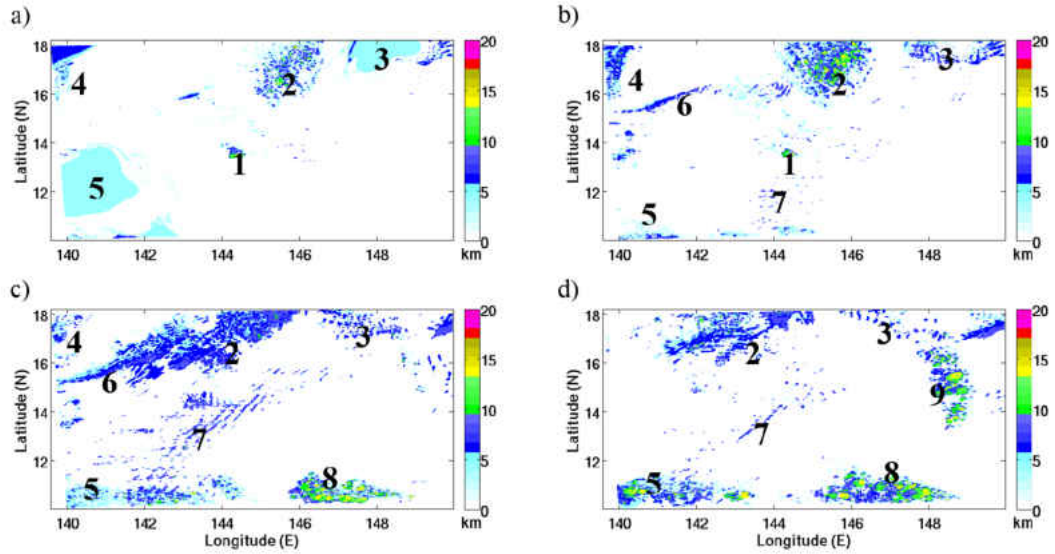


Figure 40: Echo top height composite of the maximum echo top height from the model simulation using 18 dBZ as a threshold from a) 00-06 UTC, b) 06-12 UTC, c) 12-18 UTC, and d) 18-23 UTC on 5 August 2005. Numbers represent identified convective features.

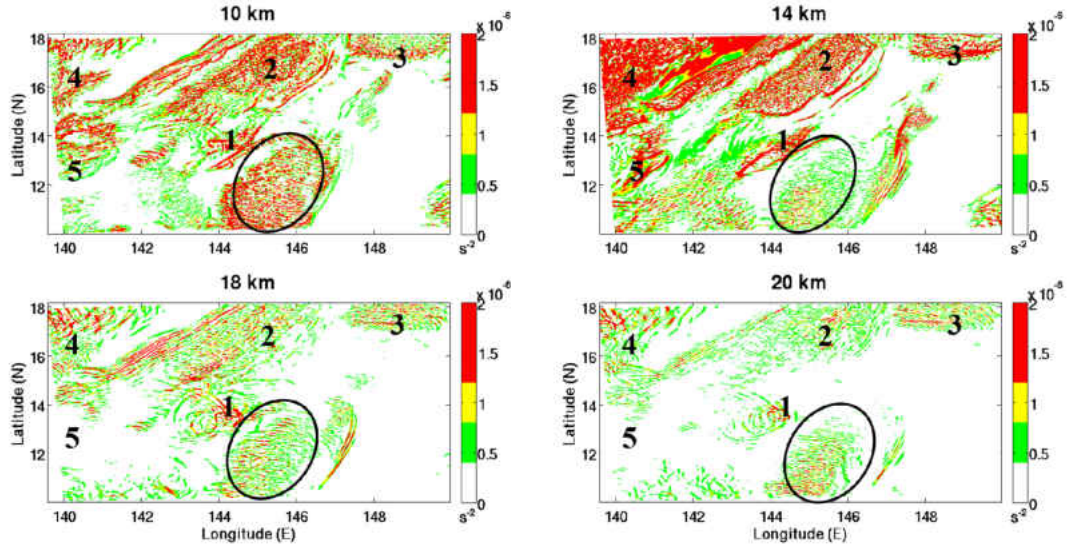


Figure 41: Estimated turbulence at a) 10 km, b) 14 km, c) 18 km, and d) 20 km at 06 UTC in 5 August 2005. Light-Moderate turbulence is represented by green, Moderate is represented by yellow, and Moderate-Severe is represented by red. Numbers represent convective features identified in the echo top analysis. Circled regions represent turbulence not associated with convective features.

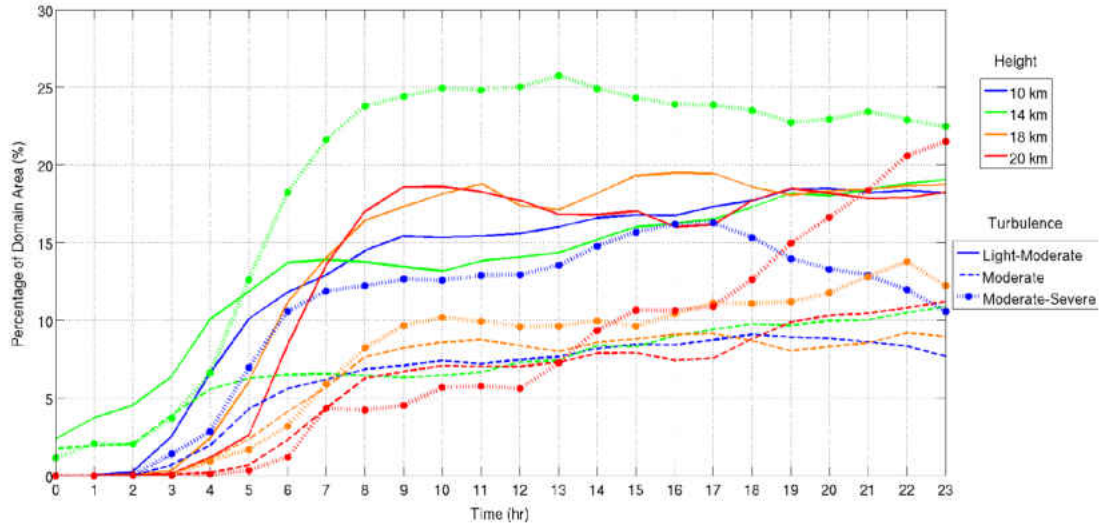


Figure 42: The percentage of the domain experiencing turbulence throughout the first 24 hours of the model simulation beginning at 00 UTC on 5 August 2005. Various colors represent the four height levels (10, 14, 18, 20 km), and solid lines represent Light-Moderate turbulence, dashed lines represent Moderate turbulence, and Moderate turbulence is represented by the dashed lines with circular markers.

As stated above, MS turbulence is located in the same regions as convective features, but MS turbulence is also found in regions where convective features have not been identified (see circled regions in Fig. 41). Further evaluation shows that these areas of turbulence are caused by the presence of vertical wind shear. Although clear air turbulence not associated with convection can pose a hazard to aviation operations, for the purpose of this study only convectively induced turbulence is discussed in detail.

During the next six hours (06-12 UTC) of the simulation, features 3-5 develop convective elements at the scale of the analysis domain resolution (Fig. 40b). Feature 3 is a large region of cells in close proximity to one another, with echo top heights less than 10 km. In addition, Features 4 and 5 have a more uniform distribution of echo top heights, generally less than 12 km. While Feature 1 intensity has decreased, the intensity of Feature 2 has increased. Furthermore, two additional convective features are present in the domain. Feature 6 is an elongated linear feature with echo top heights less than 10 km and Feature 7 is a complex of small isolated cells with echo top heights less than 10 km. Turbulence at 12 UTC is once again located near the convective features, especially near features 1, 2, 4, and 6 (Fig. 43). In addition, a vast region of MS turbulence is located in the northwest corner of the domain and extends well beyond the regions of convection at 10 and 14 km. This intense turbulence corresponds to an area of enhanced vertical wind shear and turbulence propagating away from convection. However, determining which turbulence features are convectively induced and which are caused by air motions not related to convection in this region is nearly impossible. In comparison to turbulence at 06 UTC, the percentage of the domain experiencing any intensity of turbulence has increased (Fig 42). As was the case at 06 UTC, the altitude at which MS turbulence is most extensive is 14 km, covering approximately 25% of the domain.

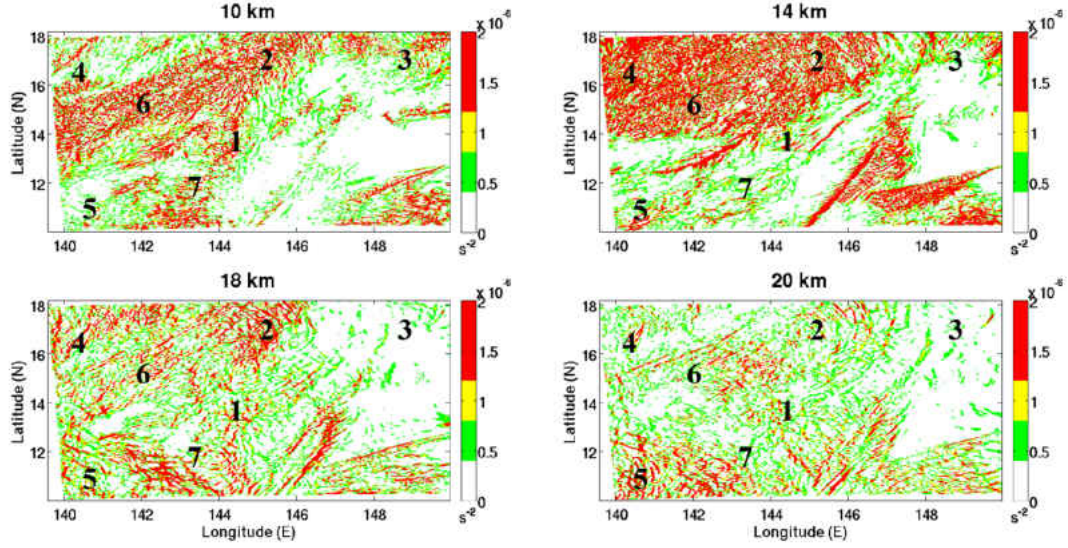


Figure 43: As in Fig. 41, except at 12 UTC.

In the following six hour period (12-18 UTC) the convection weakened in the northern portion of the domain (Fig. 40c). This weakening is especially apparent for Feature 2. All convective features have echo top heights less than 10 km, with the exception of Features 5 and 8 that have echo top heights near 16 km. Although the majority of convection is beginning to weaken during this time period, the turbulence intensity at 18 UTC in general did not decrease (Fig. 44). Furthermore, the intensity of turbulence near Features 5 and 8 increased considerably at all four heights. Likewise, the percentage of the domain experiencing MS turbulence at 20 km, in comparison to 18 km, is now greater (Fig. 42). However, the percentage of the domain experiencing MS turbulence at 14 km has begun to slightly decrease.

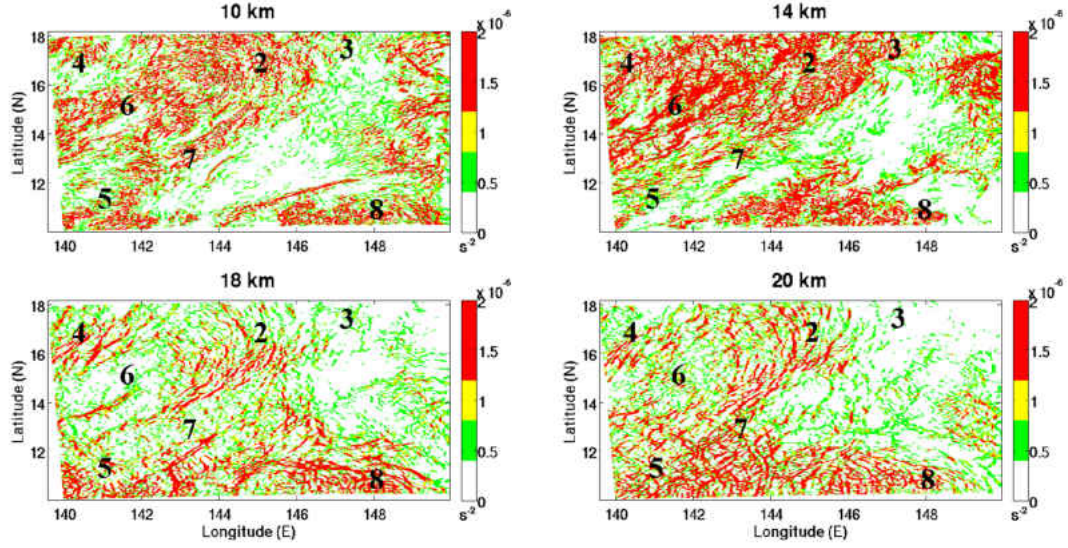


Figure 44: As in Fig. 41, except at 18 UTC.

During the remaining six hours of 5 August Features 2 and 3 continued to weaken and progress to the southwest (Fig. 40d). In addition, Features 5 and 8 continued to strengthen as echo top heights exceed 14 km. Finally, convection associated with Feature 9 has echo top heights near 14 km and progressed towards the west. In regards to turbulence intensity, at 00 UTC on 6 August a large region of MS turbulence is located near Features 2, 5, 7, 8, and 9, especially at 14 km and 20 km (Fig. 45). Furthermore, the level having the greatest domain coverage percentage of MS turbulence (23%) is 20 km (Fig. 46).

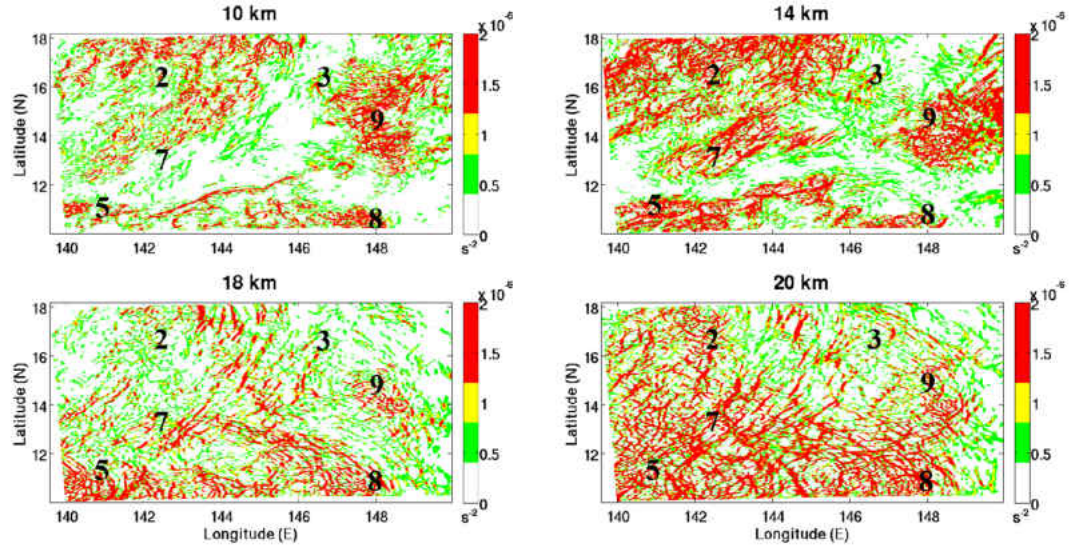


Figure 45: As in Fig. 41, except at 24 UTC.

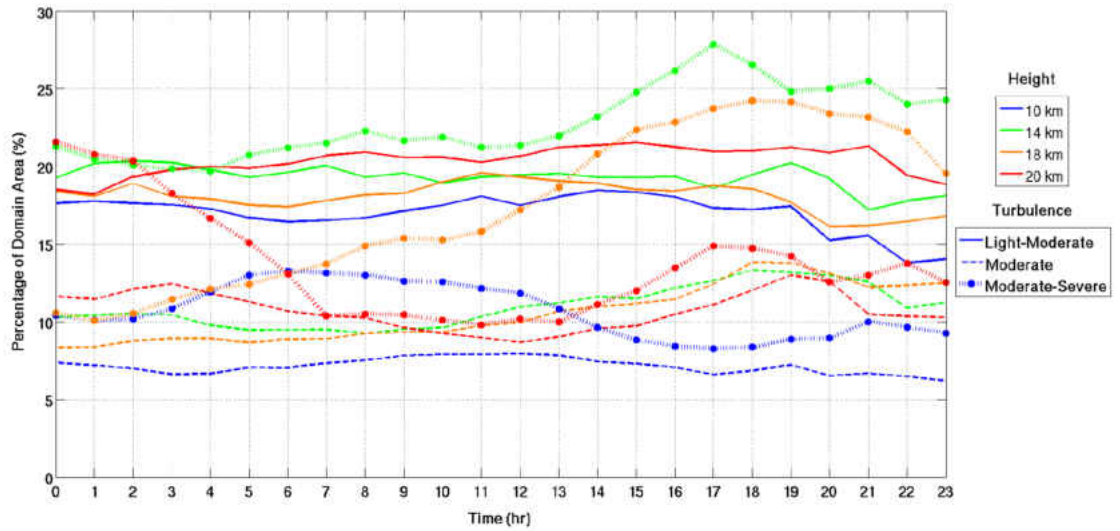


Figure 46: As in Fig. 42, except from 00-23 UTC on 6 August 2005.

The remaining 24 hours of the 48 hour simulation continued to indicate that turbulence is abundant in the domain region near convective features. The most concentrated area of MS turbulence is present near the southern boundary where convection continued to strengthen and propagate to the west. Furthermore, the

percentage of the domain experiencing Light-Moderate (LM) and Moderate (M) turbulence varies less than 5% during the last 24 hours. Lastly, the domain once again experiences the most severe turbulence at 14 km (Fig. 46).

5.4 Discussion

An examination of the strength of turbulence during the 48 hr simulation period indicates that MS is prevalent in every six hour time period up to altitudes of 20 km. Enhanced turbulence in and near the TTL has been documented in a number of past studies (i.e., Satheesan and Krishna Murthy 2002, Fujiwara et al. 2003, Alappattu and Kunhikrishnan 2010, Yamamoto et al. 2003). Alappattu and Kunhikrishnan (2010; hereafter, AK) examined 44 radiosonde ascents over the Bay of Bengal and Arabian Sea during convective free periods in 2006 from March through mid-May to gain an understanding of turbulence characteristics in the troposphere. From these data, eddy dissipation rates and stability parameters were calculated and analyzed. AK found that there is a region of enhanced turbulence between 10 and 16 km in height. They hypothesized that because there is a decrease in static stability from the troposphere to the TTL (10-15 km in height) and because breaking of Kelvin-Helmholtz waves further decreases stability, turbulence is enhanced. AK also found a maximum in wind shear near 18 km, which may explain the intense turbulence indicated by the Ellrod Index in the results presented above. Furthermore, AK examined environmental static stability by computing the square of the Brunt-Väisälä frequency (N^2). They found that between 10 and 15.5 km, N^2 fluctuated between positive and negative values and then became positive above 16 km, leading to the rapid increase in static stability near the tropopause and a decrease in turbulence. However, in this study N^2 values remained positive between 10 and 14 km and then rapidly increased above 14 km, followed by a fluctuation between increasing

and decreasing stability from 16 to 19 km (Fig. 47). Moreover, turbulence did not decrease significantly above 16 km, which could be a result of mechanical turbulence production that was large enough to overcome the damping effects of static stability (Holton 2004).

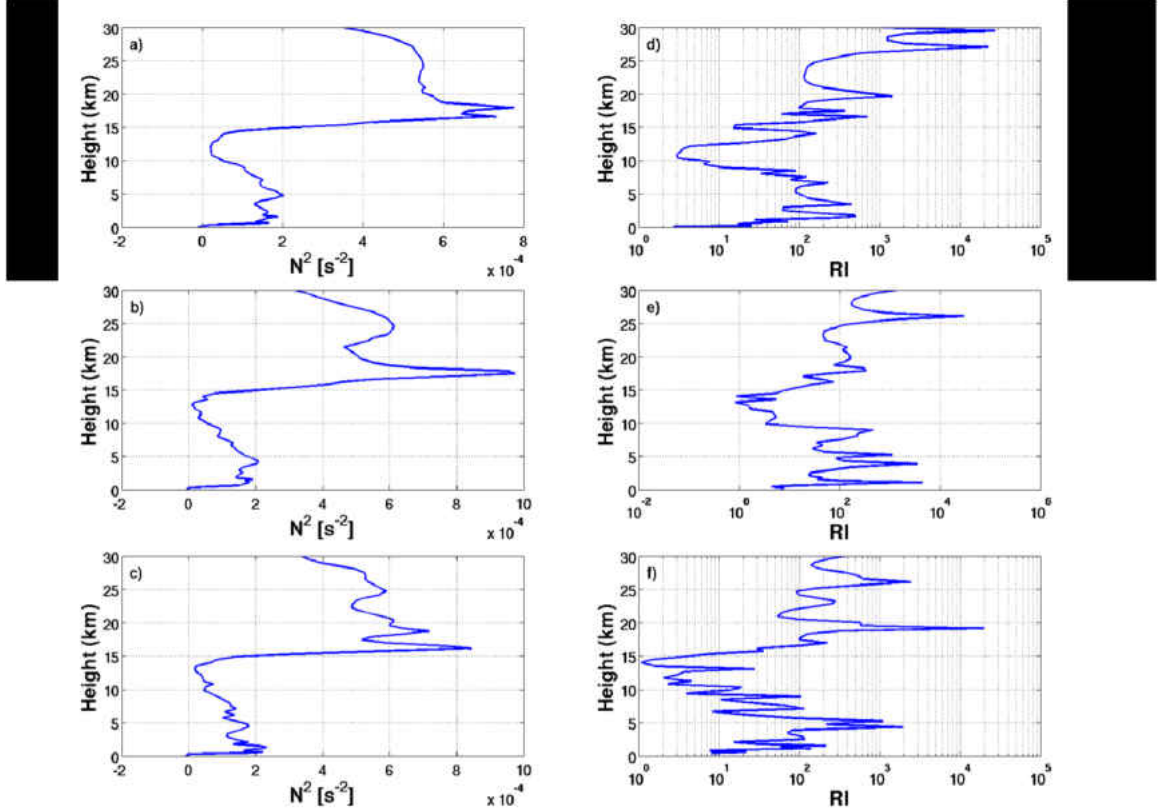


Figure 47: Square of Brunt-Väisälä frequency (N^2) and Richardson Number (RI) at a) 06 UTC, b) 12 UTC, and c) 18 UTC on 5 August 2005.

Satheesan and Krishna Murthy (2002) evaluated mesosphere-stratosphere-troposphere radar data collected from Gadanki, India and found that low values of Richardson number (RI) are associated with peaks in ε . Satheesan and Krishna Murthy (2002) concluded that low RI values indicated turbulence caused by dynamical instability due to the vertical gradient in the horizontal wind. Furthermore, Satheesan and Krishna Murthy (2002) hypothesized that the maintenance of tur-

bulence could be attributed to low RI values. In this study, RI values in the layer between 10 and 20 km were never less than 0.25 and were always greater than 0.75 (Fig. 47), indicating that turbulence may not be caused by dynamical instability. Other studies including that of Fujiwara et al. (2003) determined that enhanced turbulence observed in the tropical tropopause region over Kototabang (0.2°S , 100.2°E) was convectively generated when equatorial Kelvin waves located in the tropopause region break near the top of organized convection. In comparison to AK (2010), Fujiwara et al. (2003) found that the turbulent layer near the tropical tropopause was approximately 2 km in depth. As was previously discussed, the tropopause in this present study was identified to be at 16 km in height and turbulence is abundant both 2 km above and below the tropopause.

Due to the severe intensity of turbulence calculated over the entire simulation period, the formulation of the Ellrod Index was analyzed to provide perspective regarding the applicability of the results. The formulation of the original Ellrod Index (TI1) was based on previous studies that correlated meteorological parameters that were thought to influence clear air turbulence (CAT) to the frequency of moderate or severe turbulence encounters. The two Ellrod indices (TI1 and TI2; refer to Section 3.6) were evaluated with model resolutions greater than 50 km and were positively accepted by the meteorological community as effective indices for forecasting CAT caused by Kelvin-Helmholtz instabilities. The specific intensity thresholds (e.g. Moderate-Severe) were selected empirically by comparing index values with the location and intensity of observed CAT. These indices were designed for predicting turbulence within synoptic features in the U.S. and all verification excluded turbulence associated with convection or mountains. According to Behne (2008), Aviation Weather Center forecasters have reported a tendency for Ellrod Index values to overestimate the potential for turbulence, especially over the southern U.S, in association

with the subtropical jet. This tendency occurred for the North American Mesoscale Weather Research and Forecasting model (NAM-WRF), with a horizontal resolution of 12 km.

To test the impact of resolution on the turbulence analysis presented herein, a comparison of turbulence calculated with a coarser resolution was performed. An example of TI2 with 1.66 km and 15 km horizontal grid spacing for the innermost domain at 12 UTC on 6 August 2005 is provided in Fig. 48. At 14 km and 20 km nearly all of the MS turbulence in the northern and southern portions of the domain is absent when a coarser horizontal resolution is implemented. In addition, convectively-induced gravity waves can be seen propagating away from updraft regions at 20 km when a finer horizontal resolution is used. However, convectively-induced gravity wave features are absent at 20 km when a coarser model resolution is used. Furthermore, because the original empirical values of the Ellrod Index (TI1 and TI2) were calculated from coarse horizontal resolution, a comparison of VWS, DEF, and CVG terms (refer to Section 3.6) was also performed for the original 1.667 km horizontal resolution of this study and for 15 km horizontal resolution. This comparison led to the conclusion that the VWS term has the greatest influence on the estimation of turbulence because the magnitude of VWS is the largest ($\sim 10^{-2}$ - 10^{-3}), and with a coarser resolution, VWS is considerably less, therefore decreasing the intensity of the estimated turbulence and the percentage of the domain covered by intense turbulence.

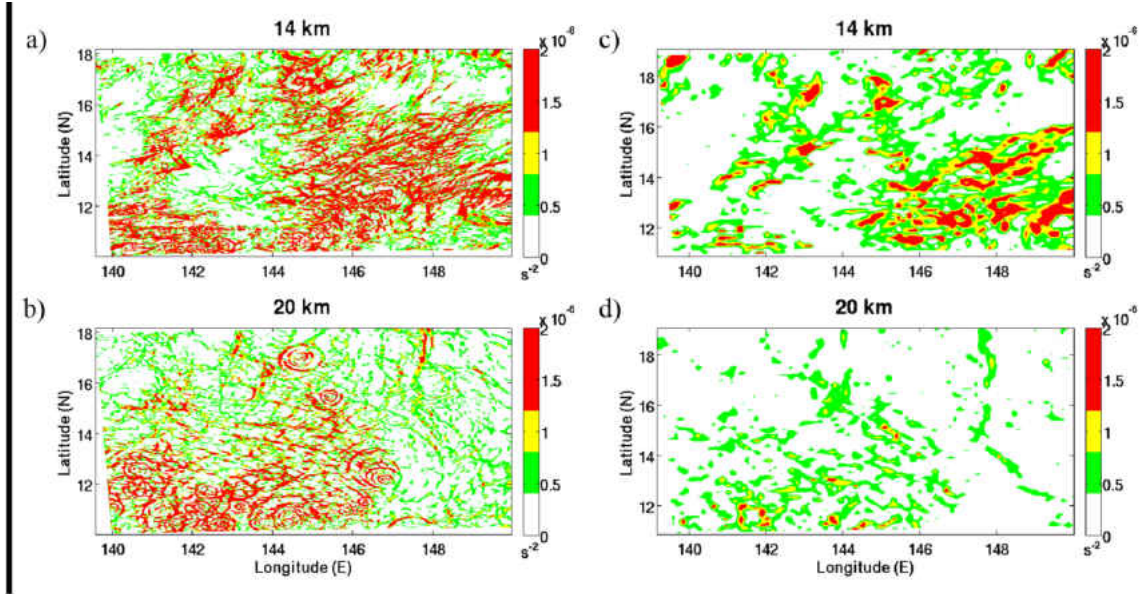


Figure 48: Comparison of Ellrod Index with varied horizontal resolution, a-b) 1.66 km horizontal grid spacing and c-d) 15 km horizontal grid spacing at 12 UTC 6 August 2005.

Clearly, the severity of turbulence estimated using coarser scale data does not agree with that estimated using finer scale data. This then brings to light the question of the accuracy of the severity and extent of turbulence when using finer resolution. Overeem (2002) concluded that because there were many assumptions made during the formulation of TI1 and TI2, the physical basis of the Ellrod Index is poor and may be the reason for high false-alarm rates. Radar measurements in the tropics indicate that turbulence within the TTL is common (i.e., Satheesan and Krishna Murthy 2002, Fujiwara et al. 2003, Alappattu and Kunhikrishnan 2010, Yamamoto et al. 2003), but the strength and extent of turbulence found in this study is questionable. Roach and Bysouth (2002) investigated how often severe CAT occurs over tropical oceans. For three case studies of synoptic patterns on days when severe CAT was reported, Roach and Bysouth (2002) used the Brown Index as a CAT index. The Brown Index is given by

$$\phi = \sqrt{0.3 \times \left(\frac{\partial v}{\partial x} - \frac{\partial u}{\partial y} + f \right)^2 + \left(\frac{\partial v}{\partial x} + \frac{\partial u}{\partial y} \right)^2 + \left(\frac{\partial u}{\partial x} - \frac{\partial v}{\partial y} \right)^2} \quad (5.1)$$

where f is the Coriolis parameter and the terms in brackets are absolute vorticity, shearing deformation, and stretching deformation (Brown 1973). Using Browns indicator, Roach and Bysouth (2002) found that severe CAT in tropical latitudes was associated with upper-level troughs generated by buckling of the Northern Hemisphere subtropical jet, and was not directly tied to convectively-induced CAT.

As others have tried to improve upon the Ellrod Index, additional turbulence estimations that have been created to aid forecasting of high-altitude CAT for aviation operations (e.g., the Brown Index, the Dutton Index; Dutton 1980, and the Ellrod-Knox Index; Lee 2013). One example of an adjustment is the Ellrod-Knox Index (Ellrod and Knox 2010). The original Ellrod Index (TI1) was adjusted to account for divergence tendency to identify CAT in situations of rapidly changing divergence associated with anticyclonic flow (hereafter, DTI). DTI is simply the sum of the TI and the divergence trend term (DVT), which is given by

$$DVT = C \left[\left(\frac{\Delta u}{\Delta x} + \frac{\Delta v}{\Delta y} \right)_{h2} - \left(\frac{\Delta u}{\Delta x} + \frac{\Delta v}{\Delta y} \right)_{h1} \right]. \quad (5.2)$$

C is a constant value set to 0.1 such that the magnitude of DVT is the product of VWS and DEF and subscripts $h2$ and $h1$ represent two forecast periods. Ellrod and Knox (2010) verified that the addition of DTI improved the accuracy of turbulence intensity in strong anticyclonic shear scenarios by comparing pilot reports of turbulence with Rapid Update Cycle-2 (RUC-2) model gridpoint values for a total of 1168 forecast-observation pairs. The horizontal grid spacing of the RUC-2 simulations implemented for the verification of DTI was 20 km (Benjamin et al. 2004).

While some uncertainty in simulated turbulence comes directly from the turbulence formulation chosen (i.e., the Ellrod Index), some uncertainty in turbulence can also be attributed to model uncertainty. An examination of the vertical velocity field at multiple heights and times indicated vertical velocities much greater than those typically observed (Fig. 49). For example, at 22 UTC on August 5 the maximum vertical velocity is greater than 30 m s^{-1} . Previous observational studies indicate that the median vertical velocity in tropical regions is less than 15 m s^{-1} (Table 1). A further evaluation of the means and standard deviations of only positive vertical velocities across the first 23 hours of the simulation was performed. This analysis indicated that the mean vertical velocity is less than 0.2 m s^{-1} at 10, 14, 18, and 20 km. Likewise, the standard deviation of vertical velocities was less than 0.4 m s^{-1} at 10, 14, 18, and 20 km. This indicates that the maximum vertical velocities are outliers within the data set (Fig. 50), and that these outliers are influencing the turbulence intensity estimates. In addition to overestimations of vertical velocity, boundary issues may be contributing to an over prediction of turbulence. Throughout the simulation strong convection is present at the southern boundary and only slightly varies in intensity. Numerically, continual convection located along or near a boundary is suspect because convection entering the inner domain is poorly resolved due to a transition in resolution and wave energy can be reflected from the boundary creating numerical instability. Thus, the continual presence of convection on the southern boundary likely resulted in inaccurate estimates of turbulence strength and extent from those features.

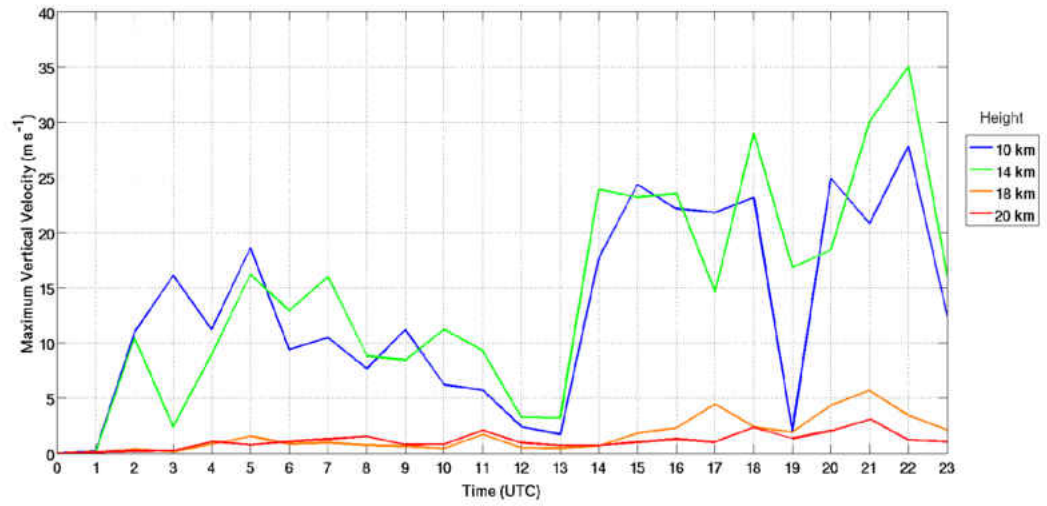


Figure 49: Maximum vertical velocity (m s^{-1}) in the domain during the first 24 hours of the simulation beginning on 5 August 2005.

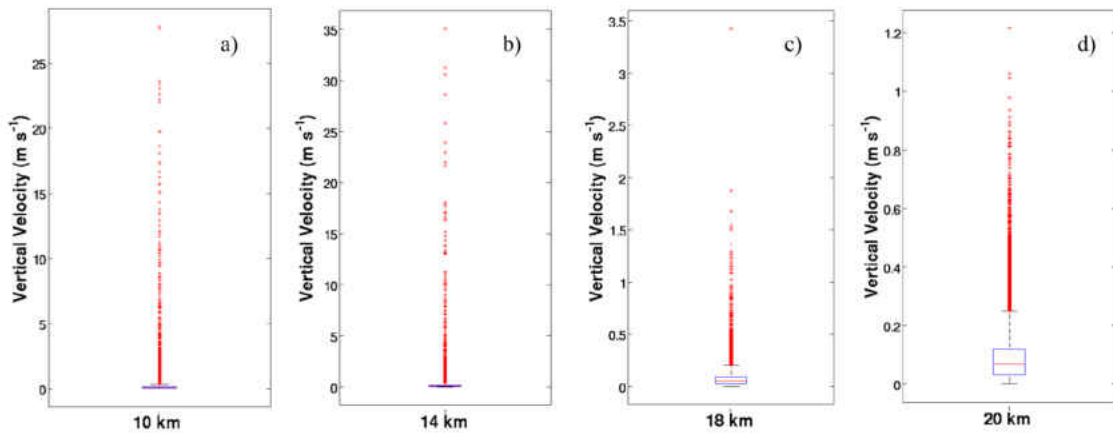


Figure 50: Vertical Velocities (m s^{-1}) at 22 UTC on 5 August 2005 at 10, 14, 18, 20 km.

The estimation of turbulence using the Ellrod Index on 5-6 August indicates that intense turbulence is abundant in the domain from 10 to 20 km in height. This turbulence is convectively induced and is also a result of large regions of strong vertical wind shear. However, determining the extent of turbulence associated only with convection is nearly impossible at this time. In addition, previous observational studies

in tropical regions have documented layers of turbulence within the TTL and near the tropopause, but the intensity was limited to Moderate and the maximum depth was limited to below 18 km. Furthermore, utilization of the Ellrod Index was found to be inappropriate for finer horizontal model resolutions and convectively-induced turbulence because the Ellrod Index was designed for model resolutions greater than 50 km, excluded convectively-induced turbulence in the verification, and the thresholds used to estimate turbulence intensity have no physical meaning. Lastly, in regards to the Federal Aviation Administration's (FAA) previous avoidance policies regarding vertical clearance over significant convective cloud tops, the recommended distance would not be sufficient to avoid turbulence. Maximum wind speeds at echo top heights at various times were less than 40 kts and according to the FAA avoidance policies, a minimum vertical separation less than 1 km of cloud tops would be recommended to avoid turbulence (Table 2). However, MS turbulence was found well above 1 km of echo top heights. The vertical clearance required for NASA's Global Hawk of 5,000 ft over significant convection would also be insufficient to avoid turbulence. Moreover, a horizontal clearance of 20 miles would also not be sufficient to avoid turbulence.

CHAPTER 6

CONCLUSIONS

Two thunderstorm type climatologies for the Guam area are created using ground and satellite-based radar data from 2005, 2010, and 2011. The ground-based radar climatology is restricted to the Guam radar coverage domain (230 km radius), while the satellite-based radar climatology is conducted in a large rectangular box encompassing 6-21 °N, 134-150 °E. The results of the climatologies indicate that aviation operations are most likely to be affected by thunderstorm activity during the summer months. During this time, isolated storms and MCSs are present in the small radar and large domain more often than during other seasons. Furthermore, during the summer months the echo top heights of all storm types is at a maximum and the Federal Aviation Administration (FAA) avoidance policies recommend that extreme caution be implemented when flying above cloud tops greater than 35,000 ft. In addition, during the summer the total area of all convection more commonly exceeds 12.5% and 60% of the domain area. This increase in areal coverage of convection impacts the regions in which flights are allowed to operate, because the FAA recommends avoiding areas where thunderstorm coverage is 60% or greater. Isolated storms are most frequently present in the domain year round, indicating that isolated storms have the potential to impact aviation operations most often. In addition to annual variability, interannual variability was also assessed by analyzing three years with different annual rainfall rates. In general, the annual rainfall rates did not impact the storm types or storm heights observed. However, the rainiest year (2011)

did have storm present in the domain more often in the winter months than the other years (2005, 2010). Lastly, a 48 hour model simulation of isolated storms and MCSs beginning on 5 August 2005 from 11-18 °N, 140-150 °E indicated large regions of Moderate-Severe turbulence at heights from 10 km to 20 km. The greatest percentage of the domain was covered by Moderate-Severe turbulence was at the height of 14 km.

The results of the ground-based radar and satellite-based radar climatologies were similar in both the percentage of time storm types were present and the percentage of time storm coverage areas exceeded domain specific thresholds. However, the climatologies were statistically different. These differences can be attributed to the spatial and temporal limitations of the data. More specifically, because the satellite-based radar has a larger latitudinal range than the ground-based radar the satellite-based climatology was sampling different populations of storms. In regards to the estimation of turbulence using the Ellrod Index, the extent of turbulence identified in this study is far beyond what is observed in midlatitude regions and in the vicinity of tropical cyclones (Lane et al. 2012; Cecil et al. 2014). Although strong turbulence has been observed within the tropical transition layer and near the tropical tropopause using active sensing instrumentation (Satheesan and Krishna Murthy 2002, Fujiwara et al. 2003, Alappattu and Kunhikrishnan 2010, Yamamoto et al. 2003, Sunilkumar 2012), the extent of turbulence in this simulation brings into question how appropriate the Ellrod Index is for the estimation of convectively-induced turbulence. The comparison of turbulence estimated using the original model resolution simulation and a coarser resolution simulation indicates that the empirical values of the Ellrod Index greatly depend upon model resolution. Therefore, the current turbulence thresholds are not appropriate for resolutions of less than 12 km. In addition, the Ellrod Index was verified using pilot reports that did not include

convectively-induced turbulence reports, which limits the use of this index. Thus, the Ellrod Index is not an appropriate method for estimating convectively-induced turbulence, and more research is needed to determine if the FAA avoidance policies are applicable in the tropics.

REFERENCES

- Ackerman, B., 1958: Turbulence around tropical cumuli. *J. Meteor.*, **15**, 69-74.
- Ackerman, T. P., K. Liou, F. P. J. Valero, and L. Pfister, 1988: Heating rates in tropical anvils. *J. Atmos. Sci.*, **45**, 1606-1623.
- Ahmad, N. N., and F. H. Proctor, 2011: Large eddy simulations of severe convection induced turbulence. *AIAA*, 2011-3201.
- Ahrens, C. D., 2008: Wind: global systems, *Meteorology Today*, M. Baird, M. Slaudt, and M. Stranz, Engage Learning, 260-261.
- Alappattu, D., and P. K. Kunhikrishnan, 2010: First observations of turbulence parameters in the troposphere over the Bay of Bengal and the Arabian Sea using radiosonde. *J. Geophys. Res.*, **115**:D6.
- Alexander, M. J., and J. R. Holton, 1997: A model study of zonal forcing in the equatorial stratosphere by convectively induced gravity waves. *J. Atmos. Sci.*, **54**, 408-419.
- American Meteorological Society, cited 2015: "El-Niño". Glossary of Meteorology. [Available online at http://glossary.ametsoc.org/wiki/El_niño].
- American Meteorological Society, cited 2014: Mesoscale Convective System. Glossary of Meteorology. [Available online at http://glossary.ametsoc.org/wiki/Mesoscale_convective_systems].

American Meteorological Society, cited 2014: Tropical Cyclone. Glossary of Meteorology. Available online at http://glossary.ametsoc.org/wiki/Tropical_cyclone].

American Meteorological Society, cited 2014: Turbulence. Glossary of Meteorology. [Available online at <http://glossary.ametsoc.org/wiki/Turbulence>].

American Meteorological Society, cited 2014: References. [Available online at <http://www.srh.noaa.gov/jetstream/tstorms/hail.htm>].

Anderson, N. F., C. A. Grainger, and J. L. Stith, 2005: Characteristics of strong updrafts in precipitation systems over the central tropical Pacific Ocean and in the Amazon. *J. Appl. Meteor.*, **44**, 731-738.

Arakawa, A., 2004: The cumulus parameterization problem: Past, present, and future. *J. Climate*, **17**, 2493-2525.

Atticks, M. G., and G. D., Robinson, 1983: Some features of the structure of the tropical tropopause. *Quart. J. Roy. Meteor. Soc.*, **109**, 295-308.

Australian Government Bureau of Meteorology, cited 2015: Analysis Chart Archive. [Available online at www.bom.gov.au/australia/charts/archive].

Aviation Weather Center, cited 2014: Ellrod Index Help. [Available online at <http://www.aviationweather.gov/exp/ellrod/info.php?mdl=NAM>].

Aviation Weather Center, cited 2015: Ellrod Index (NAM) Guidance. [Available online at <https://www.aviationweather.gov/exp/ellrod/nam/>].

Bedka, K., J. Brunner, R. Dworak, W. Feltz, J. Otkin, and T. Greenwald, 2010: Objective satellite-based detection of overshooting tops using infrared window channel brightness temperature gradients. *J. Appl. Meteor. Climatol.*, **49**, 181-202.

Behne, D., 2008: NAM-WRF verification of subtropical jet turbulence. *Nat. Wea. Ass. Electronic J. Oper. Meteor.*, **2008-EJ3**.

Bélair, S., J. Mailhot, C. Girard, and P. Vaillancourt, 2005: Boundary layer and shallow cumulus clouds in a medium-range forecast of a large-scale weather system. *Mon. Wea. Rev.*, **133**, 1938-1960.

Benjamin, S.G., D. Dévényi, S. S. Weygandt, K. J. Brundage, J. M. Brown, G. A. Grell, D. Kim, B. E. Schwartz, T. G. Smirnova, T. Lorraine Smith, and G. S. Manikin, 2004: An hourly assimilationforecast cycle: The RUC. *Mon. Wea. Rev.*, **132**, 495-518.

Berrisford, P., D. Dee, P. Poli, R. Brugge, K., Fielding, M. Fuentes, P. Kallberg, S. Kobayashi, S. Uppala, and A. Simmons, 2011: The Era-interim archive version 2.0. *ECMWF ERA Report Series*, Shinfield Park, Reading, **13**.

Biasutti, M., S. E. Yuter, C. D. Burleyson, and A. H. Sobel, 2012: Very high resolution rainfall patterns measured by TRMM precipitation radar: Seasonal and diurnal cycles. *Climate Dyn.*, **39**, 239-258.

Birner, T., 2010: Residual circulation and tropopause structure. *J. Atmos. Sci.*, **67**, 2582-2600.

Bluestein, H. B., and C. R. Parks, 1983: A synoptic and photographic climatology of low-precipitation severe thunderstorms in the Southern Plains. *Mon. Wea. Rev.*, **111**, 2034-2046.

Blyth, A. M., S. G. Lasher-Trapp, and W. A. Cooper, 2005: A study of thermals in cumulus clouds. *Quart. J. Roy. Meteor. Soc.*, **131**, 1171-1190.

Bowles, R. L., and B. Buck, 2009: A methodology for determining statistical performance compliance for airborne Doppler radar with forward-looking turbulence detection capability. NASA CR 2009-215769.

Brown, R., 1973: New indices to locate clear air turbulence. *Meteor. Mag.*, **102**, 347-361.

Bunkers, M. J., M. R. Hjelmfelt, and P. L. Smith, 2006: An observational examination of long-lived supercells. Part I: Characteristics, evolution, and demise. *Wea. Forecasting*, **21**, 673-688.

Burns, A., T. W. Harrold, J. Burnham, and C. S. Spavins, 1966: Turbulence in clear air near thunderstorms. National Severe Storms Laboratory, Technical Memorandum 30, 20 pp.

Byers, H. R., and R. R. Braham, 1949: The thunderstorm. Report of the thunderstorm project. US Govt Printing Office, 287 pp.

Carey, L. D., and S. A. Rutledge, 1998: Electrical and multiparameter radar observations of a severe hailstorm, *J. Geophys. Res.*, **103**, 13979-4000.

Cecil, D.J., and Coauthors, 2014: Weather avoidance guidelines for NASA global hawk high-altitude unmanned aircraft systems (UAS). Poster, *93rd Annual American Meteorological Society Meeting*, Atlanta, GA, Amer. Meteor. Soc..

Cecil, D. J., and C. B. Blankenship, 2012: Toward a global climatology of severe hailstorms as estimated by satellite passive microwave imagers. *J. Climate*, **25**, 687-703.

Cecil, D. J., E. J. Zipser, and S. W. Nesbitt, 2002: Reflectivity, ice scattering, and lightning characteristics of hurricane eyewalls and rainbands. Part I: Quantitative description. *Mon. Wea. Rev.*, **130**, 769-784.

Changnon, S. A., 1977: The scales of hail. *J. Appl. Meteor.*, **16**, 626-648.

Chen S. S., and R. A. Houze, 1997: Diurnal variation and life-cycle of deep convective systems over the tropical pacific warm pool. *Quart. J. Roy. Meteor. Soc.*, **123**, 357-388.

Chen, T. C., S. Y. Wang, and M. C. Yen, 2006: Interannual variation of the tropical cyclone activity over the western north Pacific. *J. Climate*, **19**, 5709-5720.

Christian, H. J., Blakeslee, R. J., Boccippio, D. J., Boeck, W. L., Buechler, D. E., Driscoll, K. T., Goodman, S. J., Hall, J. M., Koshak, W. J. and Mach, D. M., 2003: Global frequency and distribution of lightning as observed from space by the optical transient detector. *J. of Geophys. Res.*, **108**, ACL 4-1-ACL 4-15.

Clark, T. L., T. Haug, and J. P. Kuettner, 1986: Convectively forced internal gravity waves: Results from two-dimensional experiments. *Quart. J. Roy. Meteor. Soc.*, **112**, 899-926.

Climate Prediction Center, cited 2015: Cold and Warm Episodes by Season. [Available online at http://www.cpc.ncep.noaa.gov/products/analysis_monitoring/ensostuff/ensoyears.shtml].

Climate Prediction Center, cited 2015: El Nio/Southern Oscillation (ENSO) Diagnostic Discussion. [Available online at http://www.cpc.ncep.noaa.gov/products/analysis_monitoring/enso_disc_jan2005/].

Climate Prediction Center, cited 2015: El Nio/Southern Oscillation (ENSO) Diagnostic Discussion. [Available online at http://www.cpc.ncep.noaa.gov/products/analysis_monitoring/enso_disc_jan2010/].

Climate Prediction Center, cited 2015: El Nio/Southern Oscillation (ENSO) Diagnostic Discussion. [Available online at http://www.cpc.ncep.noaa.gov/products/analysis_monitoring/enso_disc_jan2011/].

Conway, J. W., and D. S. Zrnić, 1993: A study of embryo production and hail growth using Dual-Doppler and multiparameter radars. *Mon. Wea. Rev.*, **121**, 2511-2528.

Cooperative Institute for Meteorological Satellite Studies, cited 2015: Mid-Upper Layer Winds. [Available online at tropic.ssec.wisc.edu/archive/].

Cooperative Institute for Meteorological Satellite Studies, cited 2015: Mid-Lower Layer Winds. [Available online at tropic.ssec.wisc.edu/archive/].

Cooperative Institute for Meteorological Satellite Studies, cited 2015: Lower Level Convergence. [Available online at tropic.ssec.wisc.edu/archive/].

Cooperative Institute for Meteorological Satellite Studies, cited 2015: Upper Level Divergence. [Available online at tropic.ssec.wisc.edu/archive/].

Cooperative Institute for Meteorological Satellite Studies, cited 2015: Deep Layer Shear. [Available online at tropic.ssec.wisc.edu/archive/].

Corbosiero, K. L., and J. Molinari, 2002: The effects of vertical wind shear on the distribution of convection in tropical cyclones. *Mon. Wea. Rev.*, **130**, 2110-2123.

Cornman, L. B., G. Meymaris and M. Limber, 2004: An update on the FAA Aviation weather Research Programs in situ turbulence measurement and reporting system. *11th Conf. of Aviation, Range and Aerospace Meteorology*, Hyannis, MA.

Corti, T., B.P. Luo, T. Peter, H. Vomel, Q. Fu, 2005: Mean radiative energy valance and vertical mass fluxes in the equatorial upper troposphere and lower stratosphere. *Geo-phys. Res. Lett.*, **32**, L06802, doi:10.1029/2004GL021889.

Creighton, G., E. Kuchera, R. Adams-Selin, J. McCormick, S. Rentschler, and B. Wickard, 2014: AFWA Diagnostics in WRF. 1-17.

Developmental Testbed Center, 2012: Model Evaluation Tools Version 3.1 (METv3.1) Users Guide 3.1. Boulder, Colorado, USA.

Ellrod, G. P and D. I. Knapp, 1992: An objective clear-air turbulence forecasting technique: Verification and operational use. *Wea. Forecasting*, **7**, 150-165.

Ellrod G. P., and J. A. Knox, 2010: Improvements to an operational clear-air turbulence diagnostic index by addition of a divergence trend term. *Wea. Forecasting*, **25**, 789-798.

Emanuel, M., J. Sherry, S. Catapano, L. Cornman, and P. Robinson, 2013: In situ performance standard for eddy dissipation rate. Preprint and Recording, *16th*

Conf. of Aviation, Range, and Aerospace Meteorology, Austin, TX, Amer. Meteor. Soc., 11.3.

Federal Aviation Administration, 1977: Aviation weather services, Department of Transportation, 112-113.

Federal Aviation Administration, 2012: FAA aeronautical information manual. Chapter 7. [Available online at www.faa.gov/air_traffic/publications/atpubs/aim/].

Federal Aviation Administration, 2014: Aeronautical information manual: Official guide to basic flight information and ATC procedures. Chapter 7, Section 29.

Feng, Z., S. A. McFarlane, C. Schumacher, S. Ellis, J. Comstock, and N. Bharadwaj, 2014: Constructing a merged cloudprecipitation radar dataset for tropical convective clouds during the DYNAMO/AMIE experiment at Addu Atoll. *J. Atmos. Oceanic Technol.*, **31**, 1021-1042.

Folkens, I., and R. V. Martin, 2005: The vertical structure of tropical convection and its impact on the budgets of water vapor and ozone. *J. Atmos. Sci.*, **62**, 1560-1573.

Folkens, I., S. Fueglistaler, G. Lesins, and T. Mitovski, 2008: A low-level circulation in the tropics. *J. Atmos. Sci.*, **65**, 1019-1034.

Foote, G. B., 1984: A study of hail growth utilizing observed storm conditions. *J. Climate Appl. Meteor.*, **23**, 84-101.

Forster, P. M. F., R. S. Freckleton, and K. P. Shine, 1997: On aspects of the concept of radiative forcing. *Clim. Dynam.*, **13**, 547-560.

Fovell, R., D. Durran, and J. R. Holton, 1992: Numerical Simulations of Convectively Generated Stratospheric Gravity Waves. *J. Atmos. Sci.*, **49**, 1427-1442.

Fovell, R., R. Sharman, and S. Trier: 2007. A case study of convectively-induced clear air turbulence. *Conf. on Mesoscale Processes*, Proceedings, Waterville Valley, NH, 13.4.

- Frisby, E. M., and H. W. Sansom, 1967: Hail incidence in the tropics. *J. Appl. Meteor.*, **6**, 339-354.
- Fritts, D. C., and M. A. Geller, 1976: Viscous stabilization of gravity waves critical level flows. *J. Atmos. Sci.*, **33**, 2276-2284.
- Fueglistaler, S., A. E. Dessler, T. J. Dunkerton, I. Folkins, Q. Fu, and P. W. Mote, 2009: Tropical tropopause layer. *Rev. Geo.*, **47**, 1-31.
- Fujiwara, M., M. K. Yamamoto, H. Hashiguchi, T. Horinouchi, and S. Fukao, 2003: Turbulence at the tropopause due to breaking Kelvin waves observed by the Equatorial Atmosphere Radar. *J. Geophys. Res. Letts.*, **30**:D4.
- Futyan, J., and A. Del Genio, 2007: Deep convective system evolution over Africa and the tropical Atlantic. *J. Climate*, **20**, 5041-5060.
- Gallo, K., T. Smith, K. Jungbluth, and P. Schumacher, 2012: Hail swaths observed from satellite data and their relation to radar and surface-based observations: A case study from Iowa in 2009. *Wea. Forecasting*, **27**, 796802.
- Gettelman, A., and P.M de F. Forster, 2002: A climatology of the tropical tropopause layer. *J. Meteorol. Soc. Japan.*, **80**, 911-924.
- Glickman T. S., Ed., 2000: *Glossary of Meteorology*. 2d ed. Amer. Meteor. Soc., 855 pp.
- Goddard Earth Sciences Data and Information Services Center, cited 2014: Readme for TRMM Product 3B43(V7). [Available online at http://disc.sci.gsfc.nasa.gov/precipitation/documentation/TRMM_README/TRMM_3B43_readme.shtml].
- Golding, W. L., 2000: Turbulence and its impact on commercial aviation. *J. Aviation/Aerospace Edu. & Res.*, **11.2**.

Grant, L. D., and S. C. van den Heever, 2014: Microphysical and dynamical characteristics of low-precipitation and classic supercells. *J. Atmos. Sci.*, **71**, 2604-2624.

Hagos, S., Z. Feng, S. McFarlane, and L. R. Leung, 2013: Environment and the lifetime of tropical deep convection in a cloud-permitting regional model simulation. *J. Atmos. Sci.*, **70**, 2409-2425.doi: <http://dx.doi.org/10.1175/JAS-D-12-0260.1>

Hamilton, D. W., and F. H. Proctor, 2002: Convectively induced turbulence encounters during NASAs 2000 fall flight experiments. Preprints, *10th Conf. on Aviation, Range, and Aerospace Meteorology*, Portland, OR, Amer. Meteor. Soc., 371-374.

Haqq-Misra, J., S. Lee, and D. M. W. Frierson, 2011: Tropopause structure and the role of eddies. *J. Atmos. Sci.*, **68**, 2930-2944.

Heus, T., H. J. J. Jonker, H. E. A. Van den Akker, E. J. Griffith, M. Koutek, and F. H. Post, 2009: A statistical approach to the life cycle analysis of cumulus clouds selected in a virtual reality environment. *J. Geophys. Res.*, **114**, D06208.

Heymsfield, A. J., and D. J. Musil, 1982: Case study of a hailstorm in Colorado. Part II: Particle growth processes at mid-levels deduced from in-situ measurements. *J. Atmos. Sci.*, **39**, 2847-2866.

Heymsfield, G. M., L. Tian, A. J. Heymsfield, L. Li, and S. Guimond, 2010: Characteristics of deep tropical and subtropical convection from nadir-viewing high-altitude airborne doppler radar. *J. Atmos. Sci.*, **67**, 285-308.

Highwood, E. J., and B. J. Hoskins, 2006: The tropical tropopause. *Quart. J. Roy. Meteor. Soc.*, **124**, 1579-1604.

Holton, J. R., 2004: *An Introduction to Dynamic Meteorology*. Elsevier, New York.

Hong, G., G. Heygster, J. Notholt, and S. A. Buehler, 2008: Interannual to diurnal variations in tropical and subtropical deep convective clouds and convective overshooting from seven years of AMSU-B measurements. *J. Climate*, **21**, 4168-4189.

Houze R. A., and C. Cheng, 1977: Radar characteristics of tropical convection observed during GATE: Mean properties and trends over the summer season. *Mon. Wea. Rev.*, **105**, 964-980.

Houze, R.A., 1982: Cloud clusters and large-scale vertical motions in the tropics. *J. Meteor. Soc. Japan*, **60**, 396-410.

Houze, 2004: Mesoscale convective systems. *Rev. Geophys.*, **42**, 10.1029/2004RG000150, 43 pp.

Houze, R. A., 2010: Clouds in tropical cyclones. *Mon. Wea. Rev.*, **138**, 293-344.

Johnson, R. H, T. M. Ricknbach, S. A. Rutledge, P. E. Ciesielski, and W. H. Schubert, 1999: Trimodal characteristics of tropical convection. *J. Climate*, **12**, 2397-2418.

Kain, J. S., 2004: The KainFritsch convective parameterization: An update. *J. Appl. Meteor.*, **43**, 170-181.

Kaplan, M. L., Y- L. Lin, A. J. Riordan, K. T. Waight, K. M. Lux, and A W. Huffinan, 1999: Flight safety characterization studies, part I: turbulence categorization analyses. Interim Subcontrator Report to Research Lriangle Institute, NASA contract NAS 1-99074.

Kaplan, M. L., A. W. Huffman, K. M. Lux, J. J. Charney, A. J. Riordan, and Y. L. Lin, 2005: Characterizing severe turbulence environments associated with aviation accidents. *Meteor. Atmos. Phys.*, **88**, 129-152.

Keenan, T., and Coauthors, 2000: The maritime continent thunderstorm experiment (MCTEX): Overview and some results. *Bull. Amer. Meteor. Soc.*, **81**, 2433-2455.

Khairoutdinov, M., and D. Randall, 2006: High-resolution simulation of shallow-to-deep convection transition over land. *J. Atmos. Sci.*, **63**, 3421-3436.

Kim, J. H., and H. Y. Chun, 2012: A numerical simulation of convectively induced turbulence above deep convection. *J. Appl. Meteor. Climatol.*, **51**, 1180-1200.

Klimowski, B. A., M. R. Hjelmfelt, M. J. Bunkers, D. Sedlacek, and L. R. Johnson, 1998: Hailstorm damage observed from the GOES-8 Satellite: The 5-6 July 1996 ButteMeade storm. *Mon. Wea. Rev.*, **126**, 831-834.

Kodama, Y.-M., M. Katsumata, S. Mori, S. Satoh, Yuki H., and H. Ueda, 2009: Climatology of warm rain and associated latent heating derived from TRMM PR Observations. *J. Climate*, **22**, 4908-4929.

Kumar, V., A. Protat, C. Jakob, and P. May, 2013: On the atmospheric regulation of the growth of moderate to deep cumulonimbus in a tropical environment. *J. Atmos. Sci.*, **doi:10.1175/JAS-D-13-0231.1**, in press.

Lal, D M. S. D. Ghude, J. Singh, and S. Tiwari, 2014: Relationship between size of cloud ice and lightning in the tropics. *Adv. in Meteor.*, **2014**, 1-7.

Lane, T.P., M.J. Reeder, and T. L. Clark, 2001: Numerical modeling of gravity wave generation by deep tropical convection. *J. Atmos. Sci.*, **58**, 1249-1274.

Lane, T. P., R. D. Sharman, T. L. Clark, and H. M. Hsu, 2003: An Investigation of turbulence generation mechanisms above deep convection. *J. Atmos. Sci.*, **60**, 1297-1321.

Lane, T. P., R. D. Sharman, S. B. Trier, R. G. Fovell, and J. K. Williams, 2012: Recent advances in the understanding of near-cloud turbulence. *Bull. Amer. Meteor. Soc.*, **93**, 499-515.

Lang, T. J., S. A. Rutledge, 2002: Relationships between convective storm kinematics, precipitation, and lightning. *Mon. Wea. Rev.*, **130**, 2492-2506.

Lau, K.-M., H.-T. Wu, and S. Bony, 1997: The role of large-scale atmospheric circulation in the relationship between tropical convection and sea surface temperature. *J. Climate*, **10**, 381-392.

Lee, L., 2013: A climatological study of clear air turbulence over the North Atlantic. M.S. Thesis. Uppsala Universiteit.

LeMone, M. A., and E. J. Zipser, 1980: Cumulonimbus vertical velocity events in GATE. Part 1: Diameter, intensity, and mass flux. *J. Atmos. Sci.*, **37**, 2444-2457.

Lester, P. F., 1994: Turbulence: A New Perspective for Pilots. Jeppesen Sanderson, 212 pp.

Lilly, D. K., 1986: Turbulent transfer in thunderstorm outflows and thick cirrus sheets. Seminar given at MIT.

Lin, Y.-L., 1998: Mechanisms of cell regeneration, development, and propagation within a two-dimensional multicell storm. *J. Atmos. Sci.*, **55**, 1867-1886.

Lin, Y.-L., 2007: *Basic Waves Dynamics. Mesoscale Dynamics*, Cambridge University Press, 22-54.

Lucas, C., E. J. Zipser, and M. A. LeMone, 1994: Vertical velocity in oceanic convection off tropical Australia. *J. Atmos. Sci.*, **51**, 3183-3193.

Ludlam, F. H., 1976: Aspects of Cumulonimbus Study. *Bull. Amer. Meteor. Soc.*, **57**, 774-779.

Lyons, W. A., T. E. Nelson, R. A. Armstrong, V. P. Pasko, and M. A. Stanley, 2003: Upward electrical discharges from thunderstorm tops. *Bull. Amer. Meteor. Soc.*, **84**, 445-454.

MacGorman, D. R., and K. E. Nielsen, 1991: Cloud-to-ground lightning in a tornadic storm on 8 May 1996. *Mon. Wea. Rev.*, **119**, 1557-1574.

Mahinfalah, M., and R. A. Skordahl, 1998: The effects of hail damage on the fatigue strength of a graphite/epoxy composite laminate. *Composite structures*, **42.2**, 101-106.

Mancuso, R. L., and R. M. Endlich, 1966: Clear air turbulence frequency as a function of wind shear and deformation. *Mon. Wea. Rev.*, **94**, 581-585.

Markowski, P., and Y. Richardson, 2010: Organization of isolated convection, *Mesoscale Meteorology in Midlatitudes*, John Wiley and Sons, Wiley-Blackwell, 201-244.

Markowski, P., and Y. Richardson, 2010: Mesoscale convective systems, *Mesoscale Meteorology in Midlatitudes*, John Wiley and Sons, Wiley-Blackwell, 244-272.

Markowski, P., and Y. Richardson, 2010: Hazards associated with deep moist convection, *Mesoscale Meteorology in Midlatitudes*, John Wiley and Sons, Wiley-Blackwell, 273-313.

Masunaga, H., T. S. LEcuyer, and C. D. Kummerow, 2005: Variability in the characteristics of precipitation systems in the tropical Pacific. Part 1: Spatial Structure. *J. Climate*, **18**, 823-840.

Mecikalski J. R., T. A. Berendes, W. F. Feltz, K. M. Bedka, S. T. Bedka, J. J. Murray, A. J. Wimmers, P. Minnis, D. B. Johnson, J. Haggerty, B. Bernstein, M. Pavolonis, and E. Williams, 2007: Aviation Applications for Satellite-Based Obser-

vations of Cloud Properties, Convection Initiation, In-Flight Icing, Turbulence, and Volcanic Ash. *Bull. Amer. Meteor. Soc.*, **88**, 1589-1607.

Meischner, P., R. Baumann, H. Hller, and T. Jank, 2001: Eddy dissipation rates in thunderstorms estimated by Doppler radar in relation to aircraft in Situ measurements. *J. Atmos. Oceanic Technol.*, **18**, 1609-1627.

Miller, D., and J. M. Fritsch, 1991: Mesoscale convective complexes in the western pacific region. *Mon. Wea. Rev.*, **119**, 2978-2992.

Mohr, K. I., and E. J. Zipser, 1996: Mesoscale convective systems defined by their 85-GHz ice scattering signature: Size and intensity comparison over tropical oceans and continents. *Mon. Wea. Rev.*, **124**, 2417-2437.

Molinari, J., D. M. Romps, D. Vollaro, and L. Nguyen, 2012: CAPE in Tropical Cyclones. *J. Atmos. Sci.*, **69**, 2452-2463.

Mote, P. W., K. H. Rosenlof, M. E. McIntyre, E. S. Carr, J. C. Gille, J. R. Holton, J. S. Kinnersley, H. C. Pumphrey, J. M. Russell III, and J. W. Waters, 1996: An atmospheric tape recorder: The imprint of tropical tropopause temperatures on stratospheric water vapor. *J. Geophys. Res.*, **101**, 3989-4006.

National Climatic Data Center, cited 2014: Storm Events Database. [Available online at <http://www.ncdc.noaa.gov/stormevents/choosedates.jsp?statefips=98\%2CGUAM>].

National Climatic Data Center, cited 2014: NCDC Radar Resources: What is NEXRAD. [Available online at <http://www.ncdc.noaa.gov/oa/radar/radarresources.html#WHATIS>].

National Severe Storms Laboratory, cited 2015: Severe Weather 101: How is electrical charge distributed through a thunderstorm?. [Available online at <https://www.nssl.noaa.gov/education/svrwx101/lightning/>].

National Transportation Safety Board, cited 2015: Turbulence: Staying Safe. [Available online at https://www.faa.gov/passengers/fly_safe/turbulence/].

National Weather Service, cited 2014: MCS. Glossary of Meteorology. [Available online at <http://w1.weather.gov/glossary/index.php?word=MCS>].

National Weather Service, cited 2014: Mid-Latitude Areas. Glossary of Meteorology. [Available online at <http://w1.weather.gov/glossary/index.php?word=Mid-Latitude+Areas>].

National Weather Service, cited 2014: Tropics. Glossary of Meteorology. [Available online at <http://w1.weather.gov/glossary/index.php?word=Tropics>].

Nelson, S. P., 1983: The influence of storm flow on hail growth. *J. Atmos. Sci.*, **40**, 1965-1983.

Orlanski, I., and K. Bryan, 1969: Formation of the thermocline step structure by large-amplitude internal gravity waves. *J. Geophys. Res.*, **74** (28), 6975-6983.

Osuri K. K., U. C. Mohanty, A. Routray, M. A. Kulkarni, and M. Mohapatra, 2011: Customization of WRF-ARW model with physical parameterization schemes for the simulation of tropical cyclones over North Indian Ocean. *Nat. Haz.*, **63**, 1337-1359.

Overeem A. 2002. Verification of clear-air turbulence forecasts. *Technical Report TR 244*, Koninklijk Nederlands Meteorologisch Instituut: De Bilt; 76 pp.

Panofsky, H. A., and J.A Dutton, 1984: *Atmospheric Turbulence Models and Methods for Engineering Applications*. John Wiley & Sons, 397 pp.

Pantley, K. C., 1989: Turbulence near thunderstorm tops. M.S. thesis. Department of Meteorology, San Jose State University, 132 pp.

Pattanayak, S., and U. C. Mohanty, 2008: A comparative study on performance of MM5 and WRF models in simulations of tropical cyclones over Indian seas. *Current Sci.*, **95**, 923-936.

Peterson, M., and C.Liu, 2011: Global statistics of lightning in anvil and stratiform regions over the tropics and subtropics observed by the Tropical Rainfall Measuring Mission. *J. Geophys. Res.*, **116**, D23201.

Petersen, W. A., and S. A. Rutledge, 2001: Regional variability in tropical convection: Observations from TRMM. *J. Climate*, **14**, 3566-3586.

Politovich, M. K., R. K. Goodrich, C. S. Morse, A. Yates, R. Barron, and S. A. Cohn, 2011: The Juneau terrain-induced turbulence alert system. *Bull. Amer. Meteor. Soc.*, **92**, 299-313.

Potty, J., S. M. Oo, P. V. S. Raju, and U.C. Mohanty, 2012: Performance of nested WRF model in typhoon simulations over West Pacific and South China Sea. *Nat. Haz.*, **63**, 1-20.

Qian, J., 2008: Why precipitation is mostly concentrated over islands in the maritime continent. *J. Atmos. Sci.*, **65**, 1428-1441.

Raju, P. V. S, J. Potty, and U. C. Mohanty, 2011: Sensitivity of physical parameterizations on predication of tropical cyclone Nagis over the Bay of Bengal using WRF model. *Meteor. Atmos. Phys.*, **113**, 125-137.

Reid, G. C., and K. S. Gage, 1985: Interannual variations in the height of the tropical tropopause. *J. Geophys. Res.*, **90**, 5629-5635.

Reiter, E. R., and R. W. Hayman, 1962: On the nature of clear air turbulence. *Atmos. Sci. Tech.*, **28**, 1-52.

Reiter, E. R., and P. F. Lester, 1968: Richardsons number in the free atmosphere. *Archiv. Meteor. Geo. Bioklim. Sec. A.*, **17**, 1-7.

Roach, W. T., and C. E. Bysouth, 2002: How often does severe clear air turbulence occur over tropical oceans?. *Weather*, **57**:8-19.

Romps, D. M., and Z. Kuang, 2011: A transilient matrix for moist convection. *J. Atmos. Sci.*, **68**, 2009-2025.

Rozoff, C. M., W. H. Schubert, B. D. McNoldy, and J. P. Kossin, 2006: Rapid filamentation zones in intense tropical cyclones. *J. Atmos. Sci.*, **63**, 325-340.

Rutledge, S. A., E. R. Williams, and T. D. Keenan, 1992: The down under doppler and electricity experiment (DUNDEE): Overview and preliminary results. *Bull. Amer. Meteor. Soc.*, **73**, 3-16.

Rutledge, S. A., and D. R. MacGorman, 1988: Cloud-to-ground lightning activity in the 10-11 June 1985 mesoscale convective system observed during the Oklahoma-Kansas PRE-STORM project. *Mon. Wea. Rev.*, **116**, 1393-1408.

Satheesan, K., and B. V. Krishna Murphy, 2002: Turbulence parameters in the tropical troposphere and lower stratosphere. *J. Geophys. Res.*, **107**:D1.

Schultz, C. J., W. A. Petersen, and L. D. Carey, 2011: Lightning and severe weather: A comparison between total and cloud-to-ground lightning trends. *Wea. Forecasting*, **26**, 744-755.

Schumacher, C., and R. A. Houze, 2006: Stratiform precipitation production over sub-Saharan Africa and the tropical East Atlantic as observed by TRMM. *Quart. J. Roy. Met. Soc.*, **132**, 2235-2255.

Sekioka, M., 1970: Application of kelvin-helmholtz instability to clear air turbulence. *J. Appl. Meteor.*, **9**, 896-899.

Selkirk, H. B., 1993: The tropopause cold trap in the Australian monsoon during STEP/AMEX 1987. *J. Geophys. Res.*, **98**, 8591-8610.

Sharman, R., C. Tebaldi, G. Wiener, and J. Wolff, 2006: An integrated approach to mid- and upper-level turbulence forecasting. *Wea. Forecasting*, **21**, 268-287.

Sherwood, S. C., and A. E. Dessler, 2001: A model for transport across the tropical tropopause. *J. Atmos. Sci.*, **58**, 765-779.

Sherwood, S. C., and R. Wahrlich, 1999: Observed evolution of tropical deep convective events and their environment. *Mon. Wea. Rev.*, **127**, 1777-1795.

Sivakumar, V., H. Bencherif, N. Bégue, and A. M. Thompson, 2011: Tropopause characteristics and variability from 11 yr of SHADOZ observations in the southern tropics and subtropics. *J. Appl. Meteor. Climatol.*, **50**, 1403-1416.

Skok, G., J. Tribbia, and J. Rakovec, 2010: Object-Based analysis and verification of WRF model precipitation in the low- and midlatitude Pacific Ocean. *Mon. Wea. Rev.*, **138**, 4561-4575.

Son, S. W., and S. Lee, 2007: Intraseasonal variability of the zonal-mean tropical tropopause height. *J. Atmos. Sci.*, **64**, 2695-2706.

Steiner, M., R. A. Houze, and S. E. Yuter, 1995: Climatological characterization of three-dimensional storm structure from operational radar and rain gauge data. *J. Appl. Meteor.*, **34**, 1978-2007.

Stith, J. L., J. A. Haggerty, A. Heymsfield, and C. A. Grainger, 2004: Microphysical characteristics of tropical updrafts in clean conditions. *J. Appl. Meteor.*, **43**, 779-794.

Stolzenburg, M., W. D. Rust, B. F. Smull, and T. C. Marshall, 1998a: Electrical structure in thunderstorm convective regions. Part I: Mesoscale convective systems. *J. Geophys. Res.*, **103**, 14 059-14 078.

Short, D. A., and K. Nakamura, 2000: TRMM radar observations of shallow precipitation over the tropical oceans. *J. Climate*, **13**, 4107-4124.

Thuburn, J., and G. C. Craig, 2002: On the temperature structure of the tropical stratosphere. *J. Geophys. Res.*, **107**, 4017. Doi: 10.1029.2001JD000448.

Toracinta, E. R., D. J. Cecil, E. J. Zipser, and S. W. Nesbitt, 2002: Radar, passive microwave, and lightning characteristics of precipitating systems in the tropics. *Mon. Wea. Rev.*, **130**, 802-824.

Toracinta, E. R., and E. J. Zipser, 2001: Lightning and SSM/I-ice-scattering mesoscale convective systems in the global tropics. *J. Appl. Meteor.*, **40**, 983-1002.

Trier, S. B. Trier and R. D. Sharman, 2009: Convection-permitting simulations of the environment supporting widespread turbulence within the upper-level outflow of a mesoscale convective system. *Mon. Wea. Rev.*, **137**, 1972-1990.

TRMM Precipitation Radar Team, Japan Aerospace Exploration Agency, and National Aeronautics and Space Administration, 2011: Tropical Rainfall Measuring Mission (TRMM) Precipitation Radar Algorithm. *Instruction Manual for Version 7*, **L1**, 1-70.

University of Wyoming Department of Atmospheric Sciences, cited 2015: Maps/Soundings. [Available online at weather.uwyo.edu/upperair/sounding.html].

U.S.A.F, 1982: *Weather for Aircrews*. **Vol. 1**. AFN51-12VI, 13-713-13.

U.S. Department of Transportation Federal Aviation Administration, 1968: Subject: Thunderstorms. *Advisory Circular*, **00-24**, 1-6.

U.S. Department of Transportation Federal Aviation Administration, 2013: Subject: Thunderstorms. *Advisory Circular*, **00-24c**, 1-13.

Vinnichenko, N. K., N. Z. Pinus, S. M. Shmeter, and G. N. Shur, 1980: *Turbulence in the Free Atmosphere*. 2nd ed. Consultants Bureau, 310 pp.

Virts, K. S., and J. M. Wallace, 2014: Observations of temperature, wind, cirrus, and trace gases in the tropical tropopause transition layer during the MJO*. *J. Atmos. Sci.*, **71**, 1143-1157.

Vömel, H., and Coauthors, 2002: Balloon-borne observations of water vapor and ozone in the tropical upper troposphere and lower stratosphere. *J. Geophys. Res.*, **107**, D14, 4210, doi:10.1029/2001JD000707, 2002.

Vonnegut, B., 1994: The atmospheric electricity paradigm. *Bull. Amer. Meteor. Soc.*, **75**, 53-61.

Waite, M. L., and B. Khouider, 2010: The deepening of tropical convection by congestus preconditioning. *J. Atmos. Sci.*, **67**, 2601-2615.

- Walterscheid, R. L., and G. Schubert, 1990: Nonlinear evolution of an upward propagating gravity wave: Overturning, convection, transience and turbulence. *J. Atmos. Sci.*, **47**, 101-125.
- Waliser, D. E., and C. Gautier, 1993: A satellite-derived climatology of the ITCZ. *J. Climate*, **6**, 2162-2174.
- Wang, B., and J. C-L. Chan, 2002: How strong ENSO events affect tropical storm activity over the western North Pacific. *J. Climate*, **15**, 1643-1658.
- Williams, E. R, M. E. Weber, and C. D. Engholm, 1989a: Electrical characteristics of microburst producing storms in Denver. Preprints, *24th Conf. on Radar Meteorology*, Tallahassee, FL, Amer. Meteor. Soc., 89-92.
- Williams, J. K, 2004: NCAR turbulence detection algorithm. *NEXRAD Technical Advisory Committee Meeting 2004*, Indianapolis, IN.
- Wolff, J. K., and R. D. Sharman, 2008: Climatology of upper-level turbulence over the contiguous United States. *J. Appl. Meteor. Climatol.*, **47**, 2198-2214.
- Wu, C. M., B. Stevens, A. Arakawa, 2009: What controls the transition from shallow to deep convection?. *J. Atmos. Sci.*, **66**, 1793-1806.
- Wu, J., A. D. Del Genio, M.-S. Yao, and A. B. Wolf, 2009: WRF and GISS SCM simulations of convective updraft properties during TWP-ICE. *J. Geophys. Res.*, **114**, 1-18.
- Wu, Yutian, and O. Pauluis, 2014: Midlatitude tropopause and low-level moisture. *J. Atmos. Sci.*, **71**, 1187-1200.
- Xu, K., and D. A. Randall, 2001: Updraft and downdraft statistics of simulated tropical and midlatitude cumulus convection. *J. Atmos. Sci.*, **58**, 1630-1649.
- Xue, L. Z., M. A. Geller, and M. Zhang, 2004: Temperature fields in the tropical tropopause transition layer. *J. Climate*, **17**, 2901-2908.

Yamamoto, M. K., M. Fujiwara, T. Horinouchi, H. Hashiguchi, and S. Fukao, 2003: Kelvin-Helmholtz instability around the tropical tropopause observed with Equatorial Atmosphere Radar. *Geophys. Res. Lett.*, **30**(9), 1476.

Zhang, C., 1993: Large-scale variability of atmospheric deep convection in relation to sea surface temperature in the tropics. *J. Climate*, **6**, 1898-1913.

Zipser, E, 1994: Deep cumulonimbus cloud systems in the tropics with and without lightning. *Mon. Wea. Rev.*, **122**, 1837-1851.

Zipser, E. J., 2003: Some views on hot towers after 50 years of tropical field programs and two years of TRMM data. *Meteorological Monographs*, **29**, 49-49.

Zurita-Gotor, P., and G.K. Vallis, 2011: Dynamics of midlatitude tropopause height in an idealized model. *J. Atmos. Sci.*, **68**, 823-838.